Electrochemical Oxidation of Bio-derivable Alcohols Using Inorganic Materials and Mediators

by

Siqi Li

A dissertation submitted in partial fulfillment
of the requirements for the degree of
Doctor of Philosophy
(Chemistry)
in the University of Michigan
2024

Doctoral Committee:

        Professor Bart M. Bartlett, Chair
        Professor Andrej Lenert
        Professor Stephen Maldonado
        Professor Nathaniel K. Szymczak

Siqi Li

lsiqi@umich.edu

ORCID iD: 0009-0000-9729-1980

Dedication

This work is dedicated to my family.

"Family isn't always blood. It's the people in your life who want you in theirs. The ones who accept you for who you are. The ones who would do anything to see you smile, and who love you no matter what." —Maya Angelou

To the 2018 lab, or generally members before me (John, Adam, Aaron, Andy, Kori, Brad, Christian and Nate), thank you for showing me excessive patience and inclusion when I showed up as a foreigner alone with mediocre English. Thank you for all the training and valuable discussions that introduced me to the awesome science fields that the lab focused on. Thank you for introducing me to the impeccable lab culture that made me feel at home. I will proudly say our lab dynamic was state-of-the-art. I wish you all great with your careers and that I could follow your successful paths.

To the current lab, or generally members after me (Chris, Jake, Ryan, Valerie, Katie and all the other undergraduate researchers), thank you for making my part of graduate school as a mentor and a senior member immensely enjoyable. I could not have found a better group of students to pass my knowledge and the lab culture on to, and I appreciate the discussions and assistance with you on both my projects and yours. Goodbyes are always hard to say, yet it's bittersweet as I watched your growth to independent scientists. I believe the lab is in great hands and that you will achieve a lot in the future.

Table of Contents

List of Figures

List of Appendices

Abstract

Upcoming depletion of non-renewable fossil fuels provides an urgent prompt for reshaping the current structure of both direct energy sources and processing for industrial chemicals. Biorefinery hints an alternative pathway especially in processing industrial chemicals through oxidation of bio-derivable alcohols towards aldehydes and carboxylic acids that may serve as precursors to esters and polymers. With development in photovoltaic electrolyzers, renewable-energy compatible electrocatalysis serves as a promising tool to perform the selective oxidation reaction under the principles of green chemistry.

Aldehydes are considered relevant industrial chemicals that are usually evolved from fossil-fuel dependent procedures. Alcohol oxidation towards aldehyde products usually suffers from poor selectivity, remains challenging in the field and relies heavily on noble metal complexes or electrocatalysts. Here, this thesis outlines strategies to use inorganic mediators and noble-metal-free inorganic materials to achieve selective ethanol oxidation towards acetaldehyde. Solvent-free electrolysis, with ethanol as both the solvent and the substrate, is heavily implemented, where acetalization allows the generated acetaldehyde to be protected. This scheme is however understudied with ethanol being thought of as a difficult solvent for electrochemistry.

Under these circumstances, Chapter 2 investigates the use of chloride as redox mediator for solvent-free ethanol oxidation. On glassy carbon (GC), cyclic voltammetry (CV) shows chloride oxidation originates at lower potential compared to oxidation in chloride-free electrolyte. Constant potential chronoamperometry (CPC) shows 2-electron ethanol oxidation to 1,1-diethoxyethane (DEE) proceeds with >95% faradaic efficiency (FE) with chloride electrolyte. DEE arises from acetalization of acetaldehyde and protects acetaldehyde from overoxidation. UV–vis spectroscopy shows that ethyl hypochlorite (EtOCl) is the sole chloride oxidation product, which is known to decompose unimolecularly to form HCl and acetaldehyde. Finally, kinetic experiments show steady-state formation of EtOCl during electrolysis.

Chapter 3 seeks to understand the mechanism of the chloride oxidation reaction (COR) in ethanol. CV carried out at varying scan rate in inert dichloromethane solvent establishes a Volmer step, where solution chloride ion adsorbs as chlorine(0) on GC. At higher applied potential, a second electron transfer from ethanol solvent occurs, forming EtOCl. Rotating ring-disk electrode (RRDE) measurement and *in situ* spectroelectrochemical measurements corroborate the mechanism by showing no EtOCl is produced in lower potential (<0.8V), despite anodic current being observed. Thus, the 2-electron COR mechanism is confirmed to be Volmer step followed by a subsequent reaction between ethanol and adsorbed chlorine(0). Koutecky-Levich (K-L) analysis quantifies the kinetic rate constant of the COR to be 10^{-5} to 10^{-6} s^{-1}, which is 2 – 3 orders of magnitude faster than direct alcohol oxidation.

Chapter 4 develops a noble-metal-free electrocatalyst for neat ethanol oxidation. MnO$_x$ is deposited on FTO by electrochemical deposition. The material is amorphous by X-ray diffraction (XRD), and X-ray photoelectron spectroscopy (XPS) reveals a mixed-valent manganese (between Mn^{3+} and Mn^{4+}). Similar linear-sweep voltammetry (LSV) current responses are observed when tested with Cl$^-$-, NO$_3^-$-, and OTf$^-$- containing electrolytes, indicating direct ethanol oxidation occurs on MnO$_x$. After 16-hour CPC, >90% FE for DEE is observed by gas chromatrography in both Bu$_4$NOTf and HOTf electrolytes. Elemental analysis of the electrolyte solution shows <1% Mn dissolved after long-term electrolysis, highlighting its operational stability. With no potential applied, Mn dissolution occurs, and we propose the chemical oxidation of ethanol by Mn^{3+} is the rate limiting step, supported by Tafel analyses in electrolytes of varying acidity.

<p style="text-align:center">**Chapter 1**</p>

<p style="text-align:center">**Introduction**</p>

1.1. Renewable Resource Transition as the Solution to Fossil Fuel Depletion

1.1.1. Current State of Fossil Fuel Dependence

Non-renewable fossil fuels, despite their limited reserve, have seen their consumption by human activities elevating since the 1800s. Such resources were initially consumed as mainly direct energy sources as they are burnt for heating or generating electricity.[1] Accompanied with the development of chemical industries and the elevating requirement of synthetic materials, fossil fuels are also found to be critical as the fundamental source for processing, especially for industrial organic chemicals.[2] As of today, these two directions are still dominated by fossil fuels, and the productivity of many industries heavily relies on their efficient mining and conversion.

Formed from the slow decomposition of prehistoric biomasses, the once-abundant reserves of fossil fuels have made them convenient for human beings to harvest and utilize. However, due to the non-renewable nature of such substances, their complete depletion is fast approaching. A 2020 study projects that the current reserve of major fossil fuels, coal, oil and natural gas, will run out in 139, 54 and 49 years, respectively.[3] This is particularly due to the elevating consumption of such resources over the past century as can be seen from **Figure 1.1**.[4] One may also notice an equally daunting fact that despite the steady increase in total energy consumed, the contributions from renewable sources as well as nuclear are still far from ideal. Moreover, consumption of these carbon-based feedstocks brings significant public health and environmental impacts. Studies have shown that air pollution created from fossil fuel processing causes millions of casualties annually globally, in addition to as much as greater than 2 degrees Celsius of regional warming resulting from the greenhouse gas emitted.[5,6]

As such, efforts in developing renewable energies are being made by entities to target fossil fuel phase-out. Realistic projections indicated such phase-out can bring significant

<p style="text-align:center">1</p>
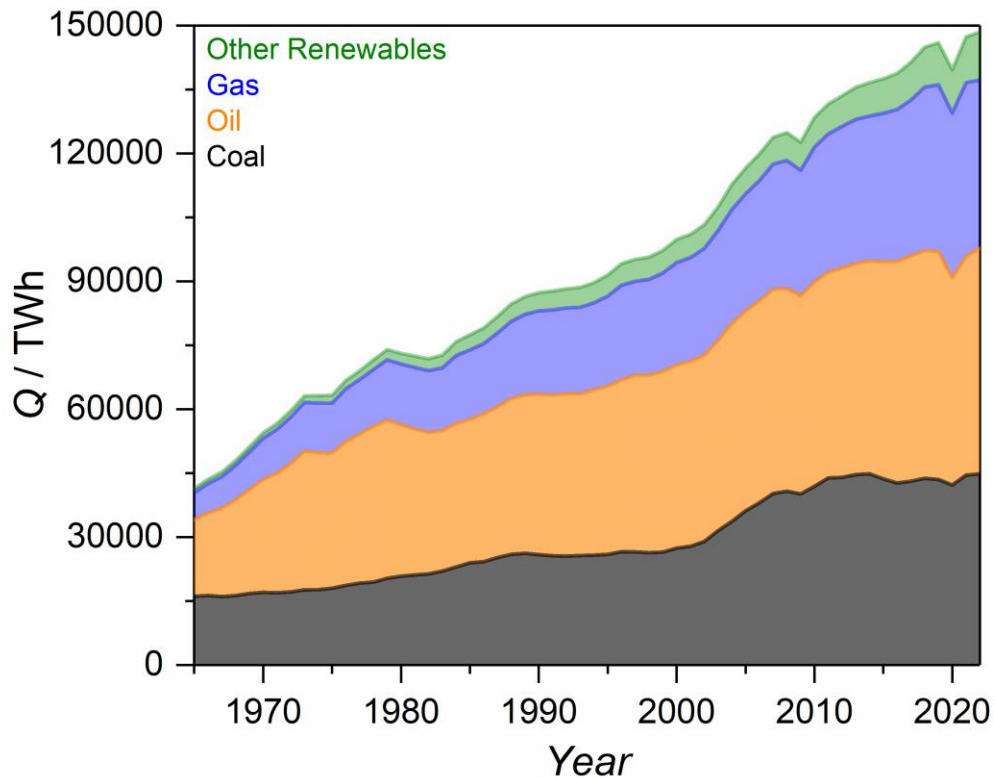
Figure 1.1. Trend of total energy consumption and breakdown of contributions from each component for the 1965-2022 region.

benefits towards controlling the adverse effect towards air quality and global warming.[7] Given the heavy current dependence on those traditional resources, the transition is expected to be a long way ahead, yet the deadline is fast approaching. Fortunately, many forms of renewable energy can be harvested and utilized once the corresponding technologies become mature. The corresponding data for "other renewables" in **Figure 1.1** consists of biofuels, solar, wind, hydropower, nuclear, and other minor sources.

1.1.2. Biomass Derived Alternative Resources for Processing

The catalytic conversion of fossil fuels remains the biggest source of many fundamental chemicals used in multiple industries. For example, hydrogen gas is sought after as the ideal "clean" fuel due to its high heat value and preferred combustion product (water).[8] However, greater than 75% of its industrial production arises from fossil fuel conversion, including steam-methane reformation with natural gas or from coal gasification.[9] Despite the fact that these methods inevitably produces CO_2 as a byproduct, the overarching reason

for their dominance is the low cost for H_2 generation compared to renewable approaches, including photochemical and photoelectrochemical catalysis that has the potential of utilizing the pseudo infinite solar energy. Similarly, crude oil cracking provides feedstock for a variety of critical chemicals including methane, ethylene, propylene, butadiene and aromatics that are then used as starting materials for synthesis of other organic chemicals.[10,11,12]

Gratefully, fossil fuel is not the only carbon-rich material available. Through photosynthesis, creatures can generate a theoretical value of ~100 billion tons of biomass annually.[13] While not all the biomass is harvestable, agricultural practices see a striking amount of biomass byproducts produced that can be further utilized. Lignocellulosic biomass is widely collected as a byproduct from sugarcane and corn agriculture and has been overlooked and wasted until recent years. Roughly 180 billion tons of such biomass is produced annually and, even though only a small portion of it has been utilized, industries have found the potential in converting it towards value-added products. **Figure 1.2** shows possible outcomes of lignocellulosic biomass valorization. Through a series of biological and chemical refining, a series of small molecules (petrochemicals) that would otherwise require the above-mentioned oil cracking can be obtained. For example, >112 Mton ethylene, >9.3 Mton butadiene and >71 Mton propylene per year is generated from petroleum refining. These chemicals are then crucial for the formation of other industrial chemicals. Fortunately, the processes illustrated in **Figure 1.2** can be implemented with little technical difficulties. From bio-derivable ethanol, ethylene can be obtained through a scalable thermal dehydration reaction; butadiene can be prepared with an aldol condensation reaction with >70% yield between ethanol and acetaldehyde, which can originate from dehydrogenation (oxidation) of ethanol. Finally, propylene can be produced in industry scale by dehydration of 1,2-propanediol.[14] Considering that greater than 180 billion tons of biomass is produced annually, fully covering the needs for such chemicals can be possible with the advances of technology and chemical engineering. Hence, products from biomass refining provide an approach to relieve the dependence on fossil fuels and their conversions by enabling alternative synthesis routes for chemicals.
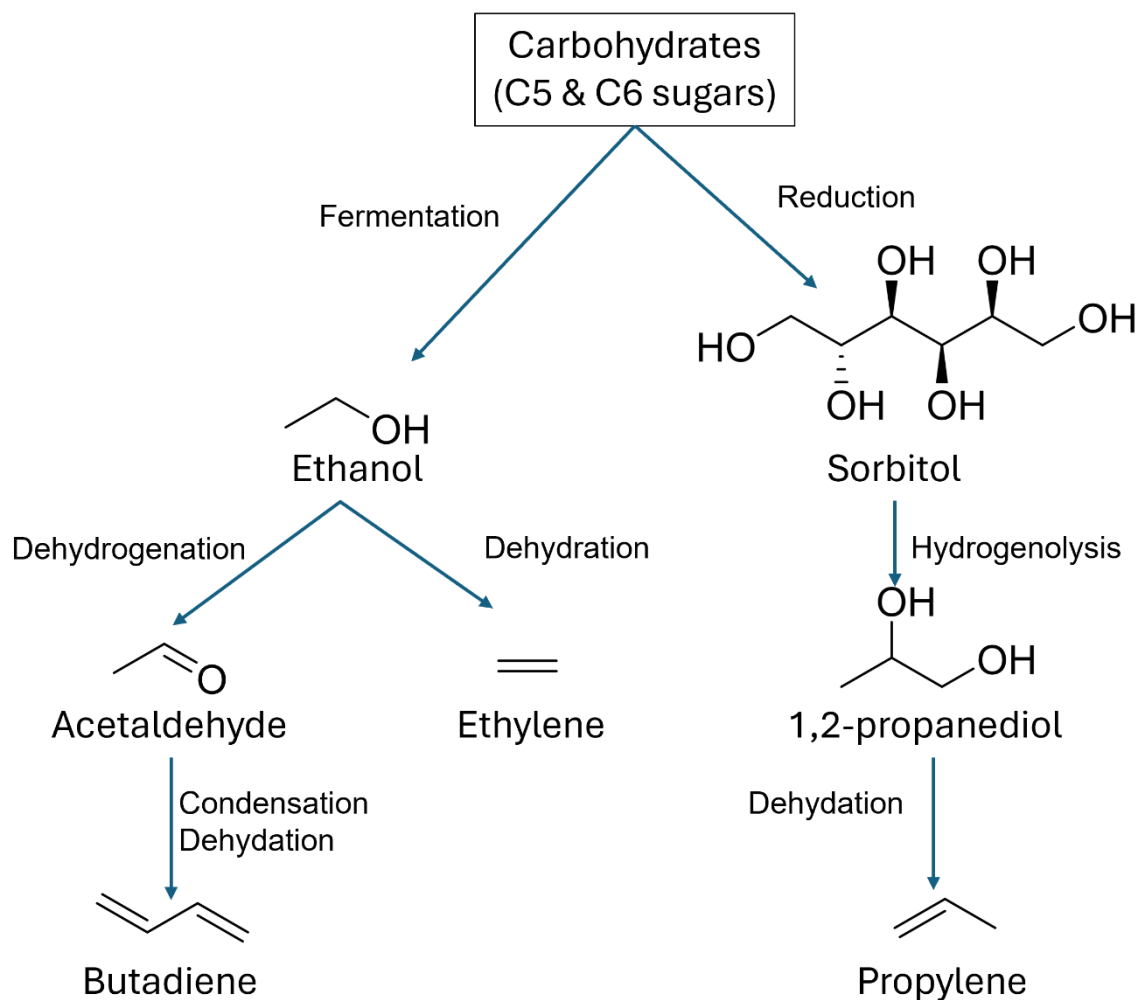
Figure 1.2. Possible production pathways of some petrochemicals from conversion of lignocellulosic biomass.

1.2. Renewable Energy Driven Catalysis of Bio-derivable Feedstocks

1.2.1. Venturing beyond Traditional Synthesis Methods

Both the fossil fuel reformation and biomass refining pathways in most cases only yield starting precursor for the chemicals needed for real-life applications. As such, performing catalytic conversion is critical to bringing absolute value to the resources.[15] With the development of photovoltaic technologies, direct and indirect conversion of renewable solar energy has been more effective. Electrocatalysis, photocatalysis and photoelectrocatalysis thus also received lots of attention and development recently, especially with the potential of direct generation of electricity from photon energy.[16]

Compared to traditional chemical conversion methods, these approaches have potential to be more budget and environmentally friendly. Partial or complete removal of stoichiometric reactant strongly increases the atomic economy, which is highly sought after under the guidance of green chemistry principles.[17] Moreover, these methods possess less demand for reaction conditions and can usually be carried out at ambient temperature and atmospheric pressure, allowing a further cut for cost and simplification of chemical processing devices.

1.2.2. (Photo)Electrochemical Water Splitting and Hydrogen Evolution Reaction

The most attractive and most developed reaction to carry out with these methods is currently water splitting. Due to the lack of stoichiometric oxidants/reductants, both sides of the redox reaction can be cast on the chemical of interest and can usually be engineered as needed. Hydrogen gas can be obtained from the cathodic (reduction) side of water splitting and may serve as an important secondary energy carrier, where ideally renewable energy is stored, besides the benefits mentioned earlier as clean fuel.[18] On the other side, oxygen gas is formed in the anodic (oxidation) reaction. A general scheme for electrochemical water splitting to give O_2 and H_2 and corresponding standard potentials for the half reactions can be found in **Figure 1.3**.[19]
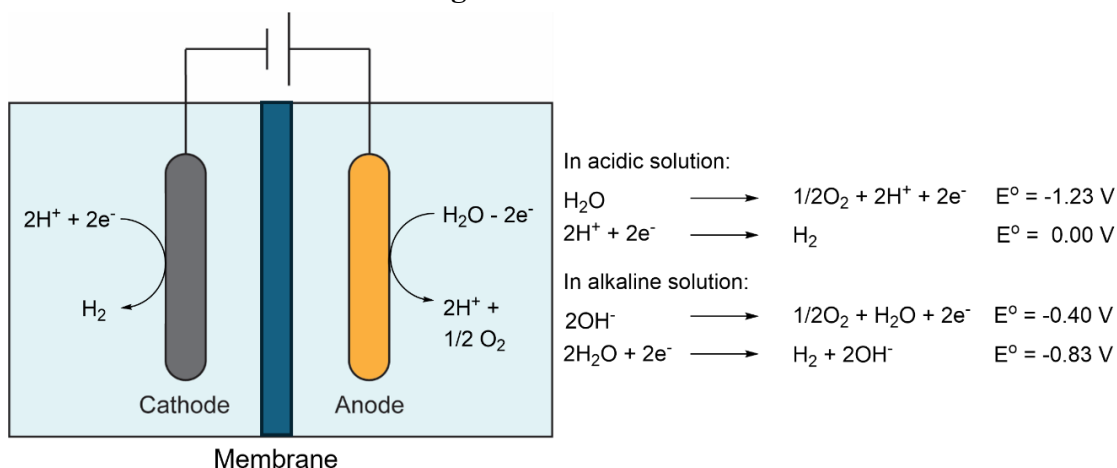
Figure 1.3. Scheme of electrochemical water splitting. Standard potentials for the corresponding electrode reactions are listed.

Considering the high cost for seawater purification, despite being an industrialized process, water splitting is far from ideal, and there are still angles for improvement.[20] In an engineering viewpoint, efforts must be made to ensure the complete separation of the

generated oxygen and hydrogen gases to avoid the explosion hazard.[21] Chemically, the oxygen evolution reaction (OER) shown in Figure 1.4 has a complicated mechanism, is thermodynamically energy demanding, and requires a large overpotential.[22] Finally, oxygen as the anode product generates very low financial value. Therefore, researchers have been seeking valuable substitutes for the OER reaction to couple with the desired hydrogen evolution reaction (HER).

1.2.3. Bio-derivable Alcohol Upgradation as Anodic Reaction

As discussed, bio-derivable alcohol (abbreviated as bioalcohols) is a readily available resource that can be utilized to relieve the dependence on petrochemicals. Ethanol is one of the most used and produced bioalcohol, and much of its current usage is as either fuel additives or as fuel itself for automobiles.[23] However, as a versatile chemical, ethanol can serve as the platform for the synthesis of many other industrial chemicals, including ethylene, acetaldehyde, acetic acid, ethyl acetate and as polymer precursors.[24] The majority of the chemicals mentioned above require an oxidative conversion of ethanol, which can be potentially carried out *via* renewable energy driven approaches mentioned in 1.2.1. Another example is 5-hydroxymethylfurfural(5-HMF), which can also be formed from the degradation of lignocellulosic biomass.[25] Upon selective oxidation, 5-HMF can be converted to a variety of valuable species that serves as precursors to bio-derivable polymers.[26] In addition, glycerol is also well sought after for its versatility in forming various chemicals upon oxidation or oxidative cleavage, despite originating from a different type of biomass.[27,28]

Still, the major purpose of performing these reactions is to produce valuable hydrogen gas with the cathodic reaction. This makes bioalcohol a more suitable target substrate especially amongst organic molecules, not only due to the extra solubility of small alcohols in water where water is the natural proton source, but also from the potential for non-aqueous electrocatalysis where the alcohol itself could serve as the proton source.

1.3. Principles and Strategies of Electrocatalysis

1.3.1. Electrochemistry and Electrochemical Organic Synthesis

Electrochemistry is one of the most powerful tools when it comes to performing redox reactions. In an ordinary electrochemical cell, one would expect the presence of electrodes, electrolyte and usually solvents. Depending on the setup required for the cells, all the components can be in different phases. A potentiostat is usually attached to the electrodes, where designated programs can be run to control the potential or current output into the cell. Generally, a 3-electrode setup including a working electrode (WE), a reference electrode (RE) and a counter electrode (CE) is preferred. The working electrode is where the most controlled reaction happens depending on the orders sent to the potentiostat. To ensure a precise quantification of the relative potential applied throughout the measurement, reference electrode is used as a non-polarizable electrode that serves as a steady reference point with known potential values. Finally, counter electrode ensures a complete circuit is formed between the cell and the potentiostat, and the opposite direction of electron transfer proceeds compared to the WE.[29]

Thus, electrochemical setup separates the desired alcohol oxidation reaction (AOR) away from the rather simple hydrogen evolution reaction so one can better provide the precise control needed in selective alcohol oxidation, where various mechanisms may proceed and lead to different products. An illustration of the AOR–HER cell can be found below in **Figure 1.4**.[30] Despite this, one still needs to keep in mind that the oxidation and reduction must proceed at the same rate. This provides more impetus to replace the slow 4-electron 4-proton OER with AOR, since the OER could be rate-limiting thus slowing the HER down.
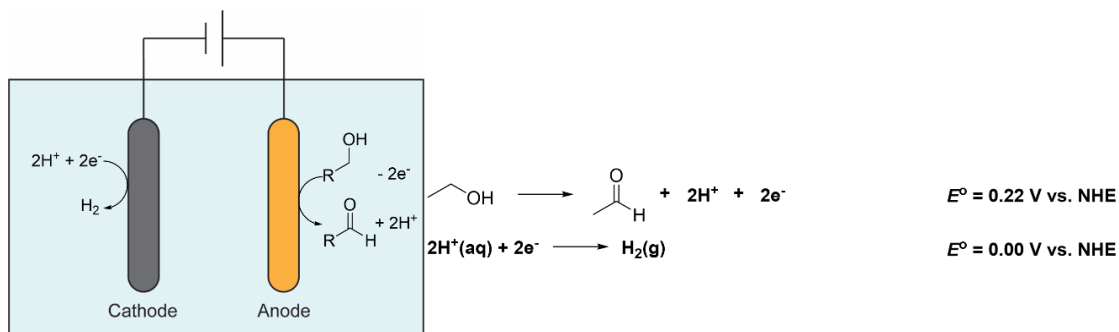
Figure 1.4. Scheme of AOR-HER electrochemical cell. Acetaldehyde/ethanol pair is selected as the model redox couple to demonstrate the design. Standard potentials of the electrode reactions are also attached.

In recent decades, electrocatalysis based organic synthesis has seen a renaissance where researchers are re-realizing its benefits and discovering amounts of novel reactions.[31]

Through applied potential on the electrodes, one-electron transfers that induce radical species critical to certain organic synthetic mechanisms may proceed in mild conditions. Moreover, through manipulating the chemical potentials of the solution redox couples as well as the potential applied on the WE, accurate control of reaction that happens can be achieved, thus unlocking undiscovered mechanism that would otherwise be impossible or avoiding undesirable parasite reactions easily.[32]

1.3.2. Direct Electrocatalysis

Selectivity is one of the major concerns in synthetic chemistry since it dictates both the yield and the extra cost introduced by purification and separation.[33] Electrochemically, selectivity can be controlled through different approaches depending on the type of electrolysis.

Direct electrocatalysis usually refers to the scenarios where the charge transfer proceeds directly between the working electrode surface and the targeted substrate. In this case, the substrate molecule will need to diffuse to the electrical double layer, possibly adsorb onto the heterogeneous electrode, and then the product must diffuse away from the surface so that new substrate molecule can diffuse into the double layer. Thus, the reaction is heavily dictated by the physical structure and chemical properties of the working electrode material. An ideal reaction then would require swift adsorption and low-energy electron transfer intermediate to form with the surface.[34] To satisfy these criteria, noble metal-based electrodes are usually considered the best candidate, especially for alcohol oxidation reactions.[35] Various research has been carried out with several noble metal electrodes, where unique strong absorption features are observed for C=O intermediates.[36] For direct electrocatalysis, selectivity is controlled through engineering of electrode material to favor different intermediates, and alternating electrochemical potential applied to the surface.

1.3.3. Indirect Electrolysis with Mediators

While direct electrolysis serves as a straightforward approach, the requirements mentioned above set many restraints on the material-substrate couple. Expensive, toxic noble metal outperforms most other materials due to their excellent properties in adsorption and stabilizing charge transfer intermediates.[37] To put more materials to use and make more mechanisms available, indirect approaches have been introduced. Redox mediators are

then utilized to bypass the hindrances of the direct pathway. **Figure 1.5** shows the general scheme for mediated indirect electrolysis.
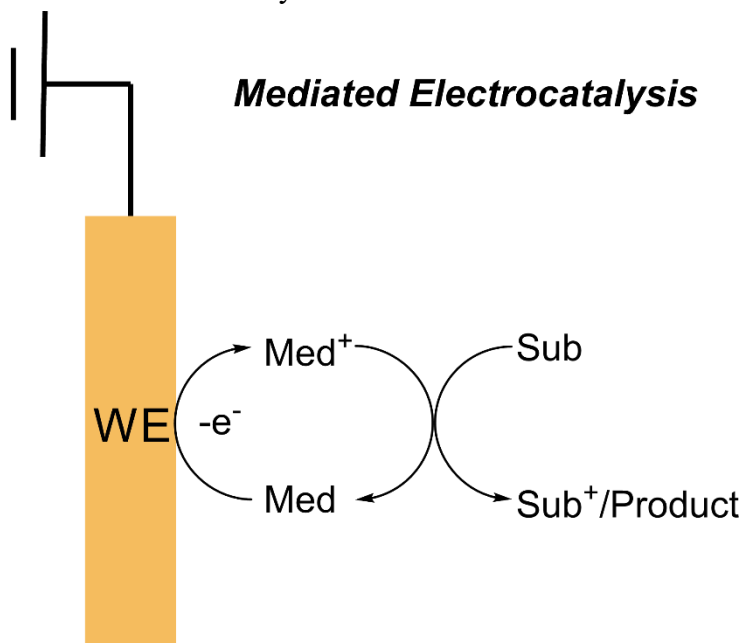
Figure 1.5. Scheme of mediated electrolysis for a 1-electron oxidation reaction. For simplicity, the counter electrode part is removed from the scheme.

Heterogeneous or homogeneous mediators will perform electron transfer (in this case, oxidation) instead. The substrate will subsequently get oxidized in a separate chemical step with the oxidized form of the mediator, with the mediator regenerated. Criteria for choosing redox mediators for alcohol oxidation are: 1) the mediator provides decent selectivity towards the desired product;[38] 2) the mediator is inexpensive and readily available; and 3) most importantly, the mediator possesses fast kinetics for its oxidation on the anode, as well as fast kinetics for oxidizing the alcohol.[39] With those in mind, various organic and inorganic mediators has been researched on, and are shown to enhance not only the selectivity but also the rate of alcohol oxidations towards desired products.[40,41]

Despite the benefits of mediators, there are noteworthy hinderances in their applications and should be considered when designing reactions. Many mediators are noble metal based organometallic compounds that suffer from poor stability in ambient conditions;[42,43] extra separation step adds to the cost for the recycle of organic mediators; active species generated from the oxidation/reduction of mediator molecules is too active that parasite reactions may proceed.[44]

1.3.4. Noble Metal Free Electrodes/Electrocatalysts

Noble metals are known to have very scarce preserve in earth crust. They pose a high cost in mining and purification, while producing strong adverse effects when released to the environment. Developing noble metal free materials thus shows much importance. **Figure 1.6** shows the abundancy of minable metal elements.[45]
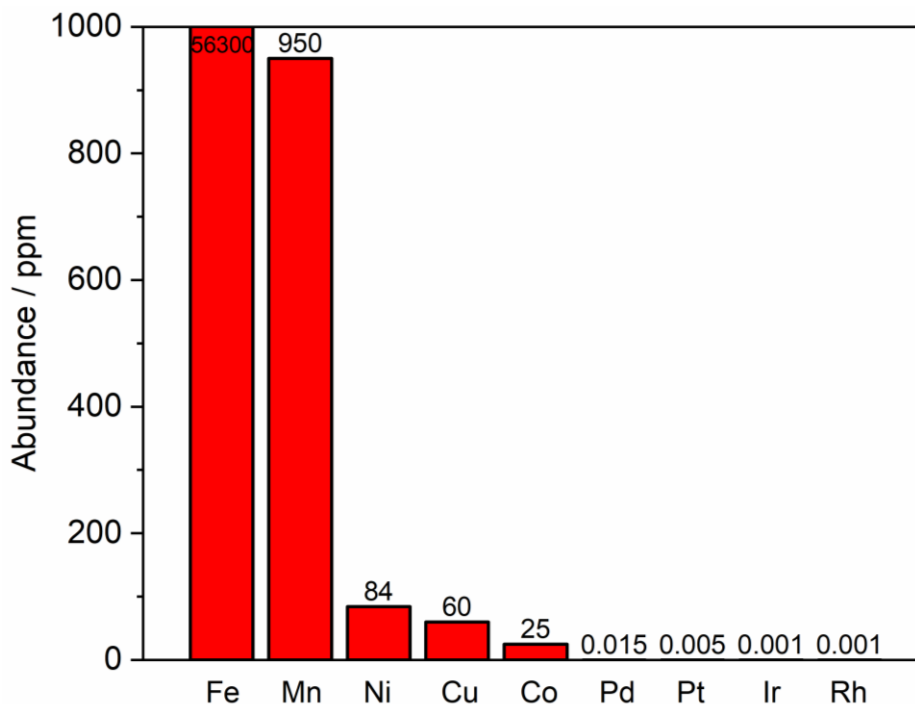
Figure 1.6. Abundance of different metals on the earth's surface.

Early transition metal oxides have been shown to perform alcohol oxidation, yet they always lack the characteristic adsorption feature exhibited by noble metals. Fortunately, with control over synthetic methods, the surface composition and morphology of these metal oxides can be engineered and can be addressed by surface characterization techniques. Advanced material synthesis methods then gave birth to tandem materials where noble metal components are loaded to a metal oxide backbone to maximize the surface area, utilize the benefits from the noble metal oxide and reduce the cost.[36] Nonetheless, researchers are still striving to create genuinely noble metal free electrocatalysts that provide similar outcomes as their noble metal based compartments.

Practically, transition metal oxides (TMOs) exhibit very different electrochemical properties in operation.[46] Compared to noble metal substance and noble metal oxides, TMOs usually suffer from poor chemical stability under unideal conditions. Under applied potential, electrochemical corrosion or passivation can also happen, adversely affecting the

activity of the material.[47] Moreover, based on element-based Pourbaix diagrams, TMOs are also prone to composition changes depending on the environment they are placed in.[48] Thus, much effort is still needed to bring TMOs to the high level of performance that noble metal based materials have been at.

1.4. Thesis Scope

This chapter highlights the overarching drive and the problem to tackle for the research carried out in this thesis. Realizing the potential of coupling electrochemical bio-derivable alcohol oxidation with hydrogen evolution reaction as an improvement substitute to water splitting, this thesis aims to provide cutting-edge insights and practices into performing such reactions with satisfactory rate and selectivity on noble metal free materials. Both direct and indirect approaches will be investigated alongside strategic improvements that bring totally different mechanisms. Electroanalytical approaches are implemented to fully understand the mechanism in neat ethanol, where chloride is used as an affordable and abundant mediator that is found to significantly accelerate the rate of electrochemical alcohol oxidation. Following deciphering the mechanism, noble metal free materials are fabricated and used as electrocatalysts for the alcohol oxidation reaction. The material exhibited a faster rate and excellent stability even under strong acidic conditions. Finally, strategies in adapting the solvent-free mechanism into the upgradation of more alcohols will be discussed, where the use of light-adsorbing semiconductors as photocatalyst is considered as a promising approach to circumvent the potential issues in electrochemistry or photoelectrochemistry.

Chapter 2 demonstrates the use of chloride anions from simple salts as redox mediators for electrochemical ethanol oxidation. Following recent work from the author and the research group, a solvent-free condition where ethanol serves both as solvent and substrate is explored. This condition showed completely different reaction pathways compared to the previous work, in which chloride was oxidized to hypochlorous acid (HOCl). Instead, UV-vis showed the formation of ethyl hypochlorite (EtOCl), avoiding the formation of an oxidized species with too strong oxidizing properties. Instead of functioning as an oxidant like traditional mediators, EtOCl produces acetaldehyde (MeCHO) with spontaneous decomposition in a separated chemical step. This alternation in oxidation product from

chloride oxidation reaction (COR) proves to be crucial in optimizing the selectivity of 2-electron oxidation product of ethanol. This work opens the gate towards a reaction system that provides excellent selectivity control, while utilizing a very accessible mediator that significantly accelerates the reaction.

Chapter 3 provides an in-depth mechanistic study for the electrochemical COR discovered in Chapter 2. In the latter, *ex situ* approaches are applied to prove the formation of EtOCl following COR, including cyclic voltammetry and UV-vis absorption analysis. To obtain more understanding on this newly discovered anode reaction, electrochemical analysis with faster timescale is utilized. Rotating ring-disk electrode analysis (RRDE), as well as other electrochemical methods, are carried out to determine the kinetic and mechanistic details of the reaction. Voltammetry experiments in an inert aprotic solvent revealed the presence of an one-electron Volmer step of Cl^- oxidation to $Cl(0)$ on the surface of the carbon. RRDE revealed the significant rate difference (2-3 orders of magnitude) between COR and direct ethanol oxidation in the absence of chloride. Eventually, collection experiments with RRDE, alongside spectroelectrochemical analysis indirectly confirm the presence of a first step where EtOCl isn't generated despite the presence of anodic current.

Chapter 4 discovers an appropriate noble metal free electrocatalyst specifically for the solvent-free ethanol oxidation scheme. On a FTO substrate, MnO_x was deposited by electrochemical deposition followed by annealing. Compared to bare FTO electrode, MnO_x showed lower overpotential besides faster rate, as is revealed by Tafel analysis. Additionally, very similar current response as well as overpotential was observed for chloride-based and chloride-free electrode, indicating the electrocatalyst can accelerate the kinetics of direct ethanol oxidation reaction by such a great extent that the rate advantage of mediators no longer exists. Moreover, the anodic current is found to be stable even in high concentration of triflic acid during electrolysis, and that the acidic condition further elevates the reaction rate. ICP-MS revealed neglectable dissolution of manganese after 24-hour electrolysis, further confirming the excellent stability. To understand the mechanism, thorough material characterizations are carried out for the film before, during and after electrolysis. It is hypothesized that a regeneration mechanism proceeds in maintaining the integrity of the MnO_x film. This work adds to more progress to the solvent-free alcohol

oxidation scheme by proving that noble metal free electrocatalysts can significantly accelerate the once-sluggish process while maintaining excellent selectivity.

Despite the promising results with alcohol oxidation in neat ethanol scheme, its drawbacks and limitations must be acknowledged. Chapter 5 delivers a comprehensive view on the potential approaches to bypass or circumvent those issues, either by performing photocatalysis or by introducing inert solvent to extend the scheme to different sorts of alcohols. This chapter also discusses the current state-of-the-art strategies applied in photocatalytic alcohol oxidation, from the standpoint of both alternating mechanisms and engineering of the semiconductor nanomaterials. Eventually, preliminary results are included to demonstrate the effectiveness of those strategies under solvent-free scenarios. The author believes that this thesis will be able to inspire further investigation in materials and mechanisms for the newly established solvent-free alcohol oxidation scheme, a novel subfield in renewable energy driven bio-derivable organic substrate upgradation and assist in relieving the elevating dependence on fossil fuels.

1.5. References

[1] Pirani, S. Burning up: A global history of fossil fuel consumption. Pluto Press, 2018.

[2] Levi, P. G.; Cullen, J. M. Mapping global flows of chemicals: from fossil fuel feedstocks to chemical products. *Environ. Sci. Technol.* **2018**, *52*, 4, 1725–1734. DOI: https://doi.org/10.1021/acs.est.7b04573

[3] Ritchie, H.; Rosado, P.; Roser, M. Fossil fuels. Our world in data, 2024.

[4] 2022 bp Statistical Review of World Energy Report. https://www.bp.com/en/global/corporate/energy-economics/webcast-and-on-demand.html#stats-review-archive (accessed February 05, 2024)

[5] Lelieveld, J.; Klingmüller. K.; Pozzer, A. Effects of fossil fuel and total anthropogenic emission removal on public health and climate. *Proc. Natl. Acad. Sci. U. S. A.* **2019**, *116*(15), 7192-7197. DOI: https://doi.org/10.1073/pnas.1819989116

[6] Holechek, J. L.; Geli, H. M.; Sawalhah, M. N.; Valdez, R. A global assessment: can renewable energy replace fossil fuels by 2050? *Sustainability* **2022**, *14*(8), 4792. DOI: https://doi.org/10.3390/su14084792

[7] Shindell, D.; Smith, C. J. Climate and air-quality benefits of a realistic phase-out of fossil fuels. *Nature* **2019**, *573*(7774), 408-411. DOI: https://doi.org/10.1038/s41586-019-1554-z

[8] Jain, I. P. Hydrogen the fuel for 21st century. *Int. J. Hydrogen Energy* **2009**, *34*(17), 7368-7378. DOI: https://doi.org/10.1016/j.ijhydene.2009.05.093

[9] Dincer, I.; Acar, C. Review and evaluation of hydrogen production methods for better sustainability. *Int. J. Hydrogen Energy* **2015**, *40*(34), 11094-1111. DOI: https://doi.org/10.1016/j.ijhydene.2014.12.035

[10] Corma, A.; Corresa, E.; Mathieu, Y.; Sauvanaud, L.; Al-Bogami, S.; Bourane, A. Crude oil to chemicals: light olefins from crude oil. *Catal. Sci. Technol.* **2017**, *7*(1), 12-46. DOI: https://doi.org/10.1039/C6CY01886F

[11] Oil Refineries. https://interestingengineering.com/innovation/oil-refineries-process-turning-crude-oil-into-jet-fuel (accessed February 05, 2024)

[12] Antonini, C.; Treyer, K.; Streb, A.; van der Spek, M.; Bauer, C.; Mazzotti, M. Hydrogen production from natural gas and biomethane with carbon capture and storage–A techno-environmental analysis. *Sustainable Energy Fuels* **2020**, *4*(6), 2967-2986. DOI: https://doi.org/10.1039/D0SE00222D

[13] Forsberg, C. W.; Dale, B. E.; Jone, D. S.; Hossain, T.; Morais, A. R. C.; Wendt, L. M. Replacing liquid fossil fuels and hydrocarbon chemical feedstocks with liquid biofuels from large-scale nuclear biorefineries. *Appl. Energy* **2021**, *298*, 117225. DOI: https://doi.org/10.1016/j.apenergy.2021.117225

[14] Cherubini, F.; Strømman, A. H. Chemicals from lignocellulosic biomass: opportunities, perspectives, and potential of biorefinery systems. *Biofuels, Bioprod. Biorefin.* **2011**, *5*(5), 548-561. DOI: https://doi.org/10.1002/bbb.297

[15] Van de Vyver, S.; Geboers, J.; Jacobs, P. A.; Sels, B. F. Recent advances in the catalytic conversion of cellulose. *ChemCatChem* **2011**, *3*(1), 82-94. DOI: https://doi.org/10.1002/cctc.201000302

[16] Ardo, S.; et al. Pathways to electrochemical solar-hydrogen technologies. *Energy Environ. Sci.* **2018**, *11*, 2768-2783. DOI: https://doi.org/10.1039/C7EE03639F

[17] Anastas, P.; Eghbali, N. Green chemistry: principles and practice. *Chem. Soc. Rev.* **2010**, *39*(1), 301-312. DOI: https://doi.org/10.1039/B918763B

[18] Tian, Y.; Mao, Z.; Wang, L.; Liang, J. Green Chemistry: Advanced Electrocatalysts and System Design for Ammonia Oxidation. *Small Struct.* **2023**, 2200266. DOI: https://doi.org/10.1002/sstr.202200266

[19] You, B.; Sun, Y. Innovative strategies for electrocatalytic water splitting. *Acc. Chem. Res.* **2018**, *51*(7), 1571-1580. DOI: https://doi.org/10.1021/acs.accounts.8b00002

[20] Liang, J.; Li, Z.; He, X.; Luo, Y.; Zheng, D.; Wang, Y.; Li, T.; Ying, B.; Sun, S.; Cai, Z.; Liu, Q.; Tang, B.; Sun, X. Electrocatalytic seawater splitting: Nice designs, advanced strategies, challenges and perspectives. *Mater. Today* **2023**, *69*, 193-235. DOI: https://doi.org/10.1016/j.mattod.2023.08.024

[21] Dresp, S.; Dionigi, F.; Klingenhof, M.; Strasser, P. Direct electrolytic splitting of seawater: opportunities and challenges. *ACS Energy Lett.* **2019** *4*(4), 933-942. DOI: https://doi.org/10.1021/acsenergylett.9b00220

[22] Liu, P. F.; Yin, H.; Fu, H. Q.; Zu, M. Y.; Yang, H. G.; Zhao, H. Activation strategies of water-splitting electrocatalysts. *J. Mater. Chem. A* **2020**, *8*(20), 10096-10129. DOI: https://doi.org/10.1039/D0TA01680B

[23] Biofuels explained. https://www.eia.gov/energyexplained/biofuels/ethanol-use.php (accessed February 06, 2024)

[24] Khaire, K. C.; Moholkar, V. S.; Goyal, A. Bioconversion of sugarcane tops to bioethanol and other value added products: an overview. *Mater. Sci. Energy Technol.* **2021**, *4*, 54-68. DOI: https://doi.org/10.1016/j.mset.2020.12.004

[25] Li, C.; Zhao, X.; Wang, A.; Huber, G. W.; Zhang, T. Catalytic transformation of lignin for the production of chemicals and fuels. *Chem. Rev.* **2015**, *115*(21), 11559-11624. DOI: https://doi.org/10.1021/acs.chemrev.5b00155

[26] Hu, L.; Xu, J.; Zhou, S.; He, A.; Tang, X.; Lin, L.; Xu, J.; Zhao, Y. Catalytic advances in the production and application of biomass-derived 2, 5-Dihydroxymethylfuran. *ACS Catal.* **2018**, *8*(4), 2959-2980. DOI: https://doi.org/10.1021/acscatal.7b03530

[27] Corma, A.; Huber, G. W.; Sauvanaud, L.; O'Connor, P. Biomass to chemicals: catalytic conversion of glycerol/water mixtures into acrolein, reaction network. *J. Catal.* **2008**, *257*(1), 163-171. DOI: https://doi.org/10.1016/j.jcat.2008.04.016

[28] Fan, L.; Liu, B.; Liu, X.; Senthilkumar, N.; Wang, G.; Wen, Z. Recent progress in electrocatalytic glycerol oxidation. *Energy Technol.* **2021**, *9*(2), 2000804. DOI: https://doi.org/10.1002/ente.202000804

[29] Bard, A. J.; Faulkner, L. R.; White, H. S. Electrochemical methods: fundamentals and applications. John Wiley & Sons. 2022

[30] Karp, G. Cell and molecular biology: concepts and experiments. John Wiley & Sons. 2009

[31] McClymont, K. S.; Wang, F. Y.; Minakar, A.; Baran, P. S. Total synthesis of (−)-maximiscin. *J. Am. Chem. Soc.* **2020**, *142*(19), 8608-8613. DOI: https://doi.org/10.1021/jacs.0c03202

[32] Novaes, L. F.; Liu, J.; Shen, Y.; Lu, L.; Meinhardt, J. M.; Lin, S. Electrocatalysis as an enabling technology for organic synthesis. *Chem. Soc. Rev.* **2021**, *50*(14), 7941-8002. DOI: https://doi.org/10.1039/D1CS00223F

[33] Zheng, R.; Liu, Z.; Wang, Y.; Xie, Z. Industrial catalysis: strategies to enhance selectivity. *Chin. J. Catal.* **2020**, *41*(7), 1032-1038. DOI: https://doi.org/10.1016/S1872-2067(20)63578-1

[34] Kim, K.; Lee, C. Recent progress in electrochemical hydrogen sulfide splitting: Strategies for enabling Sulfur-tolerant anodic reactions. *Chem. Eng. J.* **2023**, *469*, 143861. DOI: https://doi.org/10.1016/j.cej.2023.143861

[35] Lamy, C. Electrocatalytic oxidation of organic compounds on noble metals in aqueous solution. *Electrochim. Acta*, **1984**, *29*(11), 1581-1588. DOI: https://doi.org/10.1016/0013-4686(84)85012-4

[36] Cai, J.; Huang, Y.; Huang, B.; Zheng, S.; Guo, Y. Enhanced activity of Pt nanoparticle catalysts supported on manganese oxide-carbon nanotubes for ethanol oxidation. *Int. J. Hydrogen Energy* **2014**, *39*(2), 798-807. DOI: https://doi.org/10.1016/j.ijhydene.2013.10.108

[37] Oh, N. K.; Seo, J.; Lee, S.; Kim, H. J.; Kim, U.; Lee, J.; Han, Y.; Park, H. Highly efficient and robust noble metal free bifunctional water electrolysis catalyst achieved via complementary charge transfer. *Nat. Commun.* **2021**, *12*(1), 4606. DOI: https://doi.org/10.1038/s41467-021-24829-8

[38] Bosco, A. J.; Lawrence, S.; Christopher, C.; Radhakrishnan, S.; Joseph Rosario, A. A.; Raja, S.; Vasudevan, D. Redox-mediated oxidation of alcohols using Cl^-/OCl^- redox couple in biphasic media. *J. Phys. Org. Chem.* **2015**, *28*(9), 591-595. DOI: https://doi.org/10.1002/poc.3454

[39] Ganem, B. Biological spin labels as organic reagents. Oxidation of alcohols to carbonyl compounds using nitroxyls. *J. Org. Chem.* **1975**, *40*(13), 1998-2000. DOI: https://doi.org/10.1021/jo00901a030

[40] Breuhaus-Alvarez, A. G.; Li, S.; Hardin, N. Z.; Bartlett, B. M. Oxidizing Ethanol and 2-Propanol by Hypochlorous Acid Generated from Chloride Ions on H_xWO_3 Photoelectrodes. *J. Phys. Chem. C* **2021**, *125*(48), 26307-26312. DOI: https://doi.org/10.1021/acs.jpcc.1c06286

[41] Rafiee, M.; Konz, Z. M.; Graaf, M. D.; Koolman, H. F.; Stahl, S. S. Electrochemical oxidation of alcohols and aldehydes to carboxylic acids catalyzed by 4-acetamido-TEMPO: An alternative to "Anelli" and "Pinnick" oxidations. *ACS Catal.* **2018**, *8*(7), 6738-6744. DOI: https://doi.org/10.1021/acscatal.8b01640

[42] Liu, Y.; Zhao, S. F.; Guo, S. X.; Bond, A. M.; Zhang, J.; Zhu, G.; Hill, C. L.; Geletii, Y. V. Electrooxidation of ethanol and methanol using the molecular catalyst $[\{Ru_4O_4(OH)_2(H_2O)_4\}(\gamma\text{-}SiW_{10}O_{36})_2]^{10-}$. *J. Am. Chem. Soc.* **2016**, *138*(8), 2617-2628. DOI: https://doi.org/10.1021/jacs.5b11408

[43] Serra, D.; Correia, M. C.; McElwee-White, L. Iron and ruthenium heterobimetallic carbonyl complexes as electrocatalysts for alcohol oxidation: Electrochemical and mechanistic studies. *Organometallics* **2011**, *30*(21), 5568-5577. DOI: https://doi.org/10.1021/om101070z

[44] DiMeglio, J. L.; Terry, B. D.; Breuhaus-Alvarez, A. G.; Whalen, M. J.; Bartlett, B. M. Base-Assisted Nitrate Mediation as the Mechanism of Electrochemical Benzyl Alcohol Oxidation. *J. Phys. Chem. C* **2021** *125*(15), 8148-8154. DOI: https://doi.org/10.1021/acs.jpcc.0c10476

[45] Rana, S.; Biswas, J. P.; Paul, S.; Paik, A.; Maiti, D. Organic synthesis with the most abundant transition metal-iron: from rust to multitasking catalysts. *Chem. Soc. Rev.* **2021**, *50*(1), 243-472. DOI: https://doi.org/10.1039/D0CS00688B

[46] Manandhar, K.; Pletcher, D. The preparation of high surface area nickel oxide electrodes for synthesis. *J. Appl. Electrochem.* **1979**, *9*, 707-713. DOI: https://doi.org/10.1007/BF00614964

[47] Cartagena, S.; Calderón, J. A. Corrosion of non-noble metal-based catalysts during oxygen evolution reaction under on/off operation. *Corros. Sci.* **2022**, *205*, 110437. DOI: https://doi.org/10.1016/j.corsci.2022.110437

[48] Hochfilzer, D.; Chorkendorff, I.; Kibsgaard, J. Catalyst Stability Considerations for Electrochemical Energy Conversion with Non-Noble Metals: Do We Measure on What We Synthesized? *ACS Energy Lett.* **2023**, *8*(3), 1607-1612. DOI: https://doi.org/10.1021/acsenergylett.3c00021

Chapter 2

Selective Electrochemical Chloride Mediated Neat Ethanol Oxidation to 1,1-Diethoxyethane

Portions of this chapter have been published:

Reprinted with permission from Li, S.; Bartlett, B. M. *J. Am. Chem. Soc.* **2021**, *143*, 15907-15911. Copyright 2021 American Chemical Society.

2.1. Introduction

Selective conversion of biomass-derivable compounds has potential to serve as an alternative for fossil-fuel based chemical manufacturing.[1] Among all the compounds obtainable from biomass, bioethanol stands out, and the oxidative conversion of bioethanol has been widely investigated.[2,3] In particular, the formation of acetaldehyde as a platform chemical from bioethanol has attracted significant attention due to acetaldehyde's versality in preparing long-chain organic compounds.[4] Industrially, acetaldehyde is produced at 10^6 tons/year through the Wacker process starting from petroleum-based ethylene.[5,6] While converting ethanol to acetaldehyde remains a highly sought industry target, preventing overoxidation to acetic acid remains a challenge,[7] and selective ethanol oxidation typically requires either high-temperature gas phase conditions, which are energy- and equipment intensive, or requires noble metal catalysts.[8,9,10] Consequently, electrocatalysis stands as a promising alternative, where inert reagents can be activated *via* control of reaction conditions, serving as *in situ* oxidants under ambient conditions as mediators.[11,12]

Despite the excellent performance from noble metal catalysts, scarce reserve hampers the sustainability of their implement. To reduce the need for costly noble metal catalysts while maintaining selectivity, mechanistic differences must be designed to inhibit overoxidation, particularly under electrochemical (bulk electrolysis) conditions. 1,1-diethoxyethane (DEE) is a highly desirable oxygenated fuel additive (derived from ethanol and acetaldehyde) for corrosion prevention in combustion engines. This molecule offers an

additional benefit of serving as a storage platform for acetaldehyde due to its resistance to further oxidation and its low volatility, and possibility of releasing acetaldehyde when hydrolyzed.[13,14] When acetaldehyde and ethanol are mixed in low-water conditions with strong acid, DEE will form swiftly due to the acid-catalyzed nucleophilic attack of ethanol to the aldehyde, illustrated in **Figure 2.1**.[15] This established preparation requires the stoichiometric mixture of ethanol and acetaldehyde with the presence of homogeneous[16] or heterogeneous[17] acid catalysts.

overall balanced equation
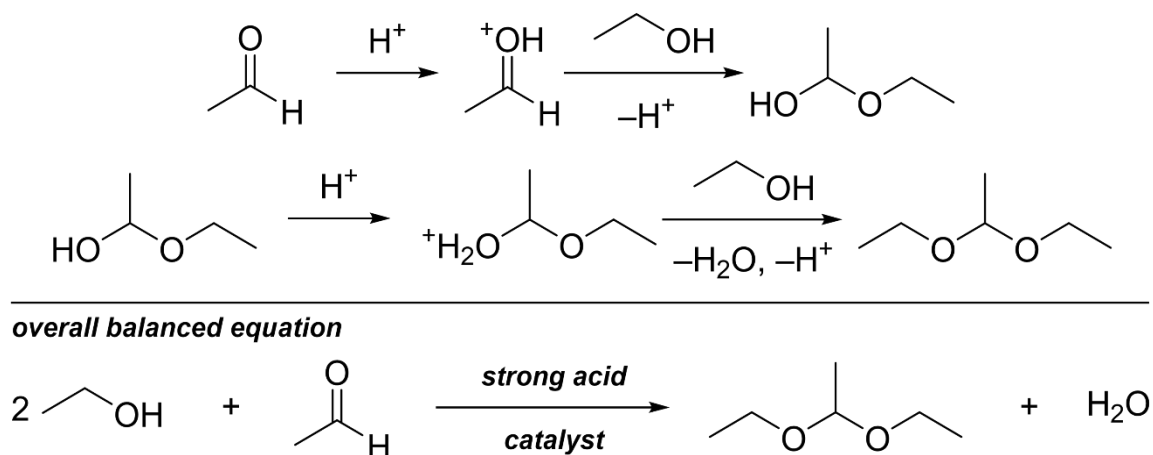
Figure 2.1. Scheme for acid catalyzed DEE synthesis by ethanol and acetaldehyde.

With DEE being a utility chemical and this specific synthesis pathway, this chapter seeks to explore its electrochemical generation through ethanol oxidation in neat ethanol conditions. In this case, acetaldehyde will be generated by the electrode reaction, resulting in the removal of it as a stoichiometric reactant, thus lowering the production cost and environmental impact. Moreover, we hypothesize that by operating in solvent-free conditions, rapid conversion of acetaldehyde to DEE shown in Figure 2.1 will proceed, thus indirectly preventing the formation of overoxidation products. Such scheme, combined with the ethanol oxidation towards acetaldehyde, gives the overall hypothesized electrochemical reaction:

$$(2.1)$$
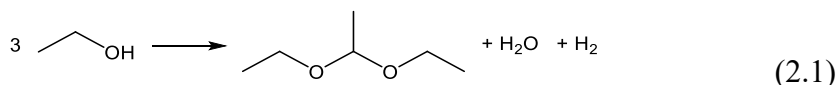
Where DEE can be converted to acetaldehyde and 2 equivalence of ethanol through hydrolysing.[18,19] These considerations provide the impetus of using DEE as a protective platform for acetaldehyde, whose selective conversion from ethanol has been challenging.[20,21] To accelerate the oxidation of the rather inert α C-H bond, researchers

have utilized redox mediators[22,23,24] and heterogeneous[25] catalysts. Historic attempts on performing equation (1) have mainly been through the methods of photocatalysis[26,27,28] and thermochemistry[29,30], since the 1990s. With the development of electrocatalysis, where reactions can be carried out in mild conditions with accurate potential control, equation (1) is also investigated electrochemically with both indirect and direct pathways. However, in these studies, not only is noble metal involved, but undesirable overoxidation to acetic acid and/or ethyl acetate proceeds, hampering the selectivity of the reaction.[31,32,33]

In such circumstances, we hypothesize that chloride anion can be an attractive abundant redox mediator, since its highly oxidizing oxoanions and substance are commonly used to oxidize organic compounds during wastewater treatment and other practices.[34,35,36] Consequently, we decided to explore indirect electrochemical solvent-free ethanol oxidation with chloride anion as mediator, targeting the synthesis of DEE.

2.2. Experiments

2.2.1. Chemicals and Materials

All chemicals were used as received unless specifically mentioned. Tetrabutylammonium chloride (Bu4NCl, ≥97.0%, Sigma-aldrich, recrystallized). Tetrabutylammonium trifluoromethanesulfonate (Bu4NOTf, >98.0%, TCI), sodium chloride (certified ACS, Fisher), sodium sulfate (99%, Alfa Aesar), silver nitrate (99.9+%, Alfa Aesar), ammonium iodide (>99%, Sigma), L-ascorbic acid (certified ACS, VWR), ferrocene (98%, Sigma-aldrich), calcium hypochlorite (Alfa Aesar), deuterated chloroform (Cambridge Isotope Laboratories), ethanol (200 proof, Fisher), acetic acid (glacier, Fisher) and hydrochlorous acid (concentrated, Fisher) are used throughout the chapter's research. Ferrocene is purified by sublimation, where the commercial ferrocene is placed in a beaker above the surface of a hotplate, and a watch glass is placed above the beaker. Upon sublimation, ferrocene will re-crystalize on the watch glass, and is collected.

2.2.2. Electrochemical Reaction Conditions

All electrochemical measurements were carried out on a CHI1000C electrochemical workstation (CH Instruments) if not specifically stated. A glassy carbon disk electrode (3mm diameter, CH Instruments) was used as working electrode throughout the study.

After each electrochemical measurement, the working electrode was polished by 0.3-micron alumina and then rinsed with 200 proof ethanol, then dried with N_2. A silver wire electrode soaked in a vessel containing the same solution as the bulk solution but separated by a glass frit was used as reference electrode. All electrochemical reactions were conducted in a glass 2-compartment cell with a glass frit as a separator. During CPC experiments, the cell was covered by parafilm to reduce the evaporation of ethanol and other volatile organic compounds. To calibrate the reference electrode to ferrocene redox couple, a 100 mM ferrocene stock ethanol solution was prepared and added to the working solution, yielding a 10 mM total concentration of ferrocene in the working solution. The ferrocene calibration scan rate was 50 mV / s. All electrolytes for quantification are prepared in volumetric flasks to certify the concentration. Tafel analysis was carried out on a CHI760C electrochemical workstation using the same electrodes (working: glassy carbon disk, counter: glassy carbon disk, reference: silver wire) and electrolyte (200 mM of salt dissolved in EtOH). The scan rate for the Tafel study was 0.5 mV / s with vigorous stirring.

2.2.3. Product Identification and Quantification

The DEE product was characterized by GC-MS analysis (Shimadzu QP-2010) and quantitative ^{1}H-NMR spectroscopy (Varian Vnmrs 700 MHz). The GC-MS sample was prepared by diluting the post-electrolysis aliquot in 200 proof ethanol. The quantitative ^{1}H-NMR sample was prepared by diluting the post-electrolysis aliquot in deuterated chloroform. NMR signals from the Bu_4NCl electrolyte are applied as the internal standard for quantification.

FT-IR measurement was carried out on a Thermo-Nicolet IS-50 spectrometer with its ATR accessory. During measurement, the background is set to ambient air, and the aliquot was dropped on the ruby directly without dilution. For the control experiment against the CPC sample, the same electrochemical cell was assembled and left stirring for the same time, but with no charge passed.

The UV-vis absorption measurement was carried out on an Agilent Cary 5000 UV-Vis-NIR spectrophotometer with a zero-baseline calibration, of which zero corresponds to air and baseline corresponds to the unaltered mother solution of EtOH with 200 mM Bu_4NCl dissolved. Before the measurement, the aliquot underwent dilution by the mother solution

to avoid exceeding the signal upper limit. A quartz cuvette is used to ensure the absorption feature of the species of interest is not interrupted by the cuvette.

Chloride recovery was carried out by adding excess silver nitrate ($AgNO_3$) aqueous solution to precipitate AgCl ($K_{sp} = 1.8 \times 10^{-10}$ at 25 ºC). The precipitate was subsequently washed with water, EtOH, and water before being dried in a vacuum oven at 60 °C. Then, the leftover powder was collected and weighed to calculate the chloride ion concentration in the mother liquor.

EtOCl titration with NH_4I is carried out with a slight change to a reported method[37]. First, 5 mL of electrolyte was added to an aqueous solution with excess KI, which was acidified by acetic acid. Stoichiometrically, the EtOCl will oxidize iodide in solution to iodine rapidly. Subsequently, the iodine was titrated by L-ascorbic acid, which can be quantified. The corresponding chemical reactions are listed below.

$$EtOCl + 2I^- + H^+ \rightarrow EtOH + Cl^- + I_2$$
$$I_2 + C_6H_8O_6 \rightarrow C_6H_6O_6 + 2I^- + 2H^+$$
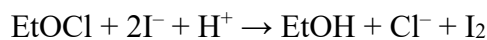
Attempts were made to observe the acetaldehyde intermediate by low-temperature ^{1}H-NMR spectroscopy. Briefly, after 1h CPC experiment, an aliquot was immediately diluted in $CDCl_3$ and then instantly cooled down by liquid N_2. The sample was inserted to the NMR instrument which was pre-cooled down to –80 °C. However, even at low temperature, the spectrum obtained showed no presence of acetaldehyde, while the formation of DEE was observed.

2.3. Results and Discussion

2.3.1. Voltammetry and Constant Potential Coulometry Results

Electrochemical oxidation of chloride anion in neat ethanol solvent has not been reported. Thus, to start, we assessed this process and explored the viability of chloride as a mediator for ethanol oxidation. Cyclic voltammetry (CV) measurements were carried out with Bu_4NCl electrolyte, and the result was compared to Bu_4NOTf, an inert electrolyte. **Figure 2.2** shows the CV traces at two different scan rates in both electrolytes.
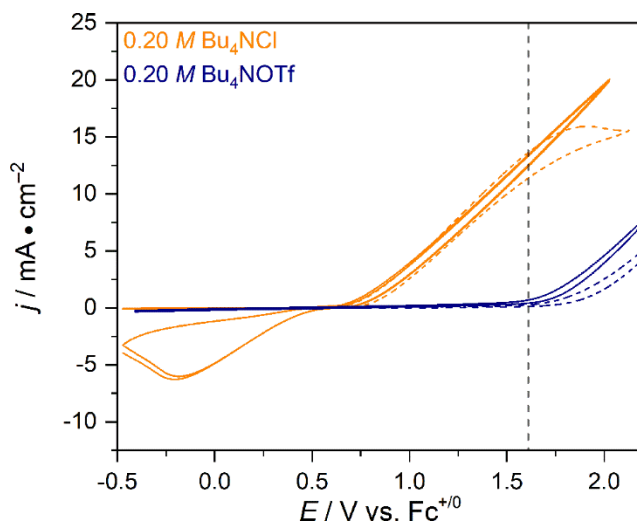
Figure 2.2. CV traces of electrolytes in ethanol. Solid and dashed lines indicate a scan rate of 10 and 100 mV / s, respectively. The gray vertical dashed line represents the onset for background current in inert electrolyte. The initial scan direction is positive.

With Bu4NCl electrolyte, a significantly less positive onset potential is observed (0.63 V vs. 1.61 V), representing an oxidation event that requires less energy input to initiate. It is noteworthy that a cathodic (reduction) peak is observed at the faster 100 mV / s scan rate, indicating the formation of a transient oxidizing species formed during the anodic (oxidation) scan. Additionally, an anodic peak is observed for the slower scan rate, representing a diffusion-controlled process in chloride oxidation. In this case, the cathodic peak is completely absent, marking the presence of an irreversible chemical step that consumes the generated oxidizing species. Note that none of these features appeared in triflate-containing electrolyte, confirming that they only emerge due to chloride oxidation.

Similar observations are seen for chloride oxidation in aqueous system on glassy carbon electrode. As can be seen in **Figure A.1**, in which a feature is also observed on the reductive scan with the presence of chloride. This suggests that chloride's behavior in ethanol mirrors that in water where ethanol oxidation has shown to be mediated by chloride oxidation. Next, the mediative ability of chloride is decided by conducting constant potential chronoamperometry (CPC) analysis at 1.61 V vs. $Fc^{+/0}$, which is the most positive potential before the onset of background current observed in **Figure 2.2**. The CPC results for both chloride-containing and chloride-free scenarios are shown in **Figure 2.3**.
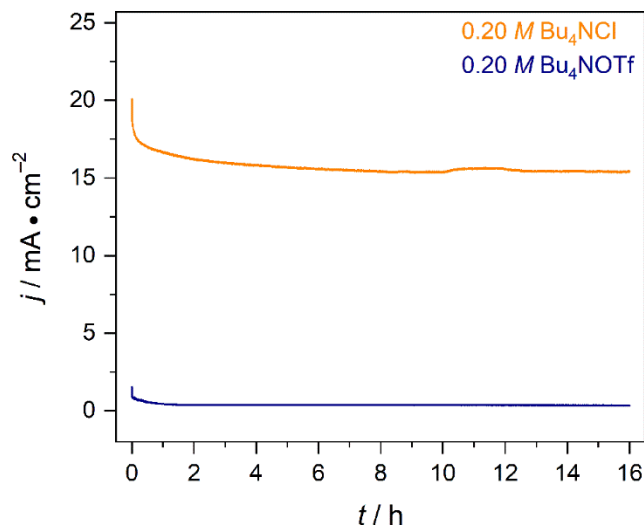
Figure 2.3. CPC curves of ethanol solution with different electrolytes poised at 1.61 V vs Fc$^{+/0}$.

At this potential, Bu$_4$NCl electrolyte shows a high, stable current density (> 15 mA / cm^2), while the Bu$_4$NOTf electrolyte yields negligible current. According to the proposed mechanism in reaction (1), DEE is the anticipated product, and is quantified through ^{1}H-NMR spectroscopy (**Figure A.2**) alongside the qualitative confirmation by GC-MS (**Figure A.3**). Both techniques confirm the generation of DEE, and that DEE is the sole organic product. Moreover, FT-IR spectrum in **Figure A.4** shows no signal for C=O stretch, indicating no acetic acid or ethyl acetate is formed, which could be from the 4-electron overoxidation. The faradaic efficiency (FE) is quantified to be 95.8 ± 1.9 % and is determined by the following equation:

$$FE \ (\%) = \frac{n \cdot N_{DEE} \ (mol) \cdot F}{Q} \cdot 100 \ \% \qquad (2.2)$$

where n is the number of electrons transferred (n = 2, due to the redox reaction only proceeds towards the formation of acetaldehyde, and the conversion from acetaldehyde to 1,1-DEE is chemical, not electrochemical), F is Faraday's constant and Q is the amount of charge passed (determined from the integration of the CPC curve). In the triplate case, no detectable product is observed, as expected from to the negligible amount of charge passed. This result suggests that in this indirect oxidation mechanism, chloride plays a critical part.

2.3.2. Detection of the Intermediate and Kinetic Study

To understand the chloride-mediated mechanism in ethanol, more efforts are made to track the possible intermediates. Based on the aqueous chloride-water Pourbaix diagram,

hypochlorous acid (HOCl) dominates the neutral pH region.[38] In ethanol solution with no external Bronsted acid or base source, we hypothesize that the anode reaction forms analogous product to HOCl, which is ethyl hypochlorite (EtOCl) according to reaction (3):

$$Cl^- + EtOH \rightarrow EtOCl + H^+ + 2e^- \qquad (2.3)$$
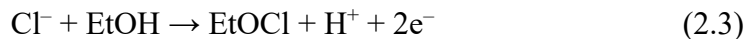
Most alkyl hypochlorites are volatile water-insoluable liquids that decompose violently upon irradiation or heat, yielding their corresponding carbonyl compounds (aldehydes or ketones) and hydrochlorous acid, according to reaction (4):[37]

$$EtOCl \rightarrow MeCHO + H^+ + Cl^- \qquad (2.4)$$
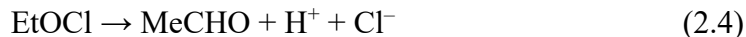
Thus, not much attention and applications have been put to these chemicals. Realizing most chloride-oxidation products are able to be detected by UV-vis spectroscopy, we attempted to track and identify EtOCl. **Figure 2.4** shows a series of UV-vis absorption measurements carried out for our chloride-containing electrolysis solution, which is measured immediately after a 1-hour electrolysis.
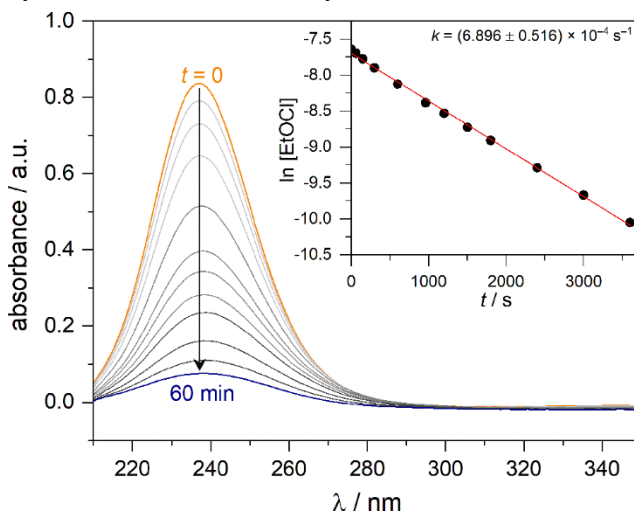
Figure 2.4. UV-vis spectra of chloride solution recorded after a 1 h CPC experiment. t = 0 (orange) is measured immediately after opening the circuit. The inset shows first-order kinetics for EtOCl decomposition, where the concentration of EtOCl is determined by titration method demonstrated in 2.2.3. The linear fit (red) gives the rate constant, which is an average of 3 trials (replicates presented in **Figure A.7**).

The aliquot was allowed to stay untouched in the UV-vis chamber, while absorption measurements are measured over time until 60 minutes from the first measurement taken in the beginning. Across the spectra, only one absorption feature is observed at $\lambda \sim 237$ nm, identical to what is observed for gas-phase ethyl hypochlorite[39]. The full spectrum is shown in **Figure A.5** to show the sole presence of this species. This observed decomposition pattern agrees with reported properties of alkyl hypochlorites, further confirming EtOCl is

being produced from the anodic reaction. To assess the rate of such decomposition, initial concentrations of EtOCl are measured *via* reaction with iodide and L-ascorbic acid titration, in a separate experiment. Through replicates, we confirmed EtOCl decomposes with first-order kinetics, as is shown by the linear relationship between ln[EtOCl] and time. This decomposition forms acetaldehyde, which immediately reacts with ethanol in the faction shown in **Figure 2.1**. The kinetic rate constant of the deposition step is quantified and shown in the figure above.

Following the confirmation of the redox intermediate, we move on to verify that chloride is indeed functioning as a mediator, rather than consumed stoichiometrically. A 27-hour CPC experiment is carried out to pass a significant amount of charge (**Figure A.6**). In this experiment, if chloride is consumed stoichiometrically for the 2-electron oxidation, or converted to other species, ~50 % of initial concentration would be lost based on the amount of charge passed. By adding excess aqueous $AgNO_3$ solution to precipitate the chloride, 98.1 % of the initial chloride is recovered in the form of AgCl, confirming that it is not consumed through electrolysis. While we also attempted to track the formation of acetaldehyde, the result was not successful. As is mentioned, DEE is observed as the only organic product post electrolysis. Flash-freezing of the sample aliquot followed by low-temperature ^{1}H-NMR was not able to track the formation of acetaldehyde, either. We believe that due to the rather slow rate of EtOCl decomposition as well as the overwhelming excess of ethanol around, acetaldehyde reacts too quickly to be detected *ex situ*, thus also avoiding overoxidation, agreeing with the near unity faradaic efficiency for DEE.

Further, we tracked the formation of DEE in parallel with the change of EtOCl by measuring the concentration of both species by ^{1}H-NMR and UV-vis spectroscopy, respectively during CPC. **Figure 2.5** shows the concentrations of both species over the course of a 4-hour CPC experiment.
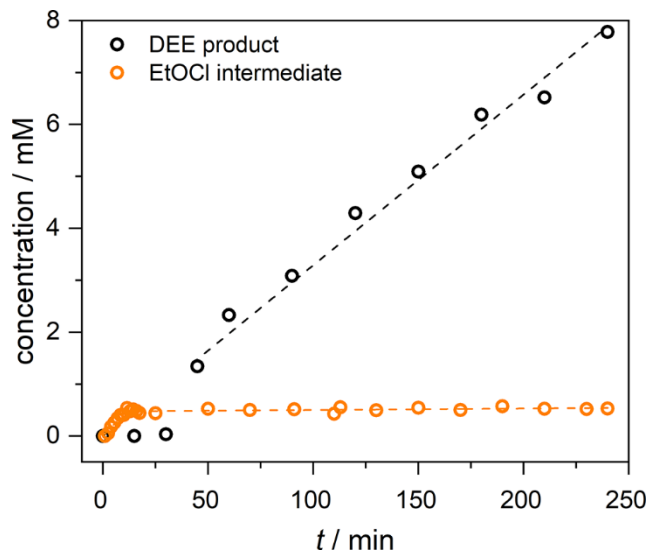
Figure 2.5. Plot of [EtOCl] intermediate and [DEE] product during the first 4 hours of the CPC experiment.

A rapid buildup of EtOCl concentration can be observed in the first ~20 minutes as it is being electrochemically generated. Since its degradation adheres to first order kinetics, the degradation gets accelerated as concentration builds up. Thus, it reaches steady-state regime as it reaches its critical concentration. Once this equilibrium is established, the near-linear growth of DEE can be observed.

Finally, we performed Tafel analysis to provide additional insight to the chloride oxidation step. With a slow-scan rate stirred LSV measurement, the Tafel slope of chloride oxidation is observed to be 163 mV / dec (**Figure A.8**), lower than that observed on a Pd/Ti electrocatalyst for aqueous ethanol oxidation.[40] This indicates a faster kinetic compared to the aqueous case, even with noble metal based catalyst. Although, this Tafel slope is larger than what is observed in aqueous chloride oxidation reactions, especially on metal oxide electrodes.[41] Considering the electrode used throughout the project is only glassy carbon, there is clear impetus in developing other electrocatalyst for the solvent-free scheme.

2.4. Conclusions

On commercial glassy carbon electrode, we found selective neat ethanol oxidation to DEE proceeds through an ethyl hypochlorite intermediate that is observable by UV-Vis spectroscopy. The reaction yields DEE as the sole product with near unity faradaic efficiency, under a high and stable current density at lower potential input. We propose that acetaldehyde derived from the ethyl hypochlorite intermediate is quickly converted to DEE,

protecting it from further oxidation or volatilization (DEE has a very high boiling point compared to ethanol). Recovery experiments show that chloride is not consumed during the reaction, confirming its participation as a redox mediator. Chloride oxidation occurs at a potential 1 V less positive than background direct ethanol oxidation measured with Bu$_4$NOTf. The alkyl hypochlorite decomposition mechanism exploited here under ambient conditions represents a promising approach to deliver targeted aldehyde (or ketone) products from not only ethanol but other alcohols, without using toxic or expensive oxidants and metal catalysts. Additionally, understanding the potential of applying this mechanism to other bio-derivable alcohols is our current target.

2.5. References

[1] McGlade, C.; Ekins, P. The geographical distribution of fossil fuels unused when limiting global warming to 2 C. *Nature* **2015**, *517*(7533), 187-190. DOI: https://doi.org/10.1038/nature14016

[2] Sun, J.; Wang, Y. Recent advances in catalytic conversion of ethanol to chemicals. *ACS Catal*. **2014**, *4*(4), 1078-1090. DOI: https://doi.org/10.1021/cs4011343

[3] Grim, R. G.; To, A. T.; Farberow, C. A.; Hensley, J. E.; Ruddy, D. A.; Schaidle, J. A. Growing the bioeconomy through catalysis: a review of recent advancements in the production of fuels and chemicals from syngas-derived oxygenates. *ACS Catal.* **2019**, *9*(5), 4145-4172. DOI: https://doi.org/10.1021/acscatal.8b03945

[4] Sato, A. G.; Volanti, D. P.; Meira, D. M.; Damyanova, S.; Longo, E.; Bueno, J. M. C. Effect of the ZrO_2 phase on the structure and behavior of supported Cu catalysts for ethanol conversion. *J. Catal.* **2013**, *307*, 1-17. DOI: https://doi.org/10.1016/j.jcat.2013.06.022

[5] Liu, P.; Hensen, E. J. Highly efficient and robust $Au/MgCuCr_2O_4$ catalyst for gas-phase oxidation of ethanol to acetaldehyde. *J. Am. Chem. Soc.* **2013**, *135*(38), 14032-14035. DOI: https://doi.org/10.1021/ja406820f

[6] Keith, J. A.; Henry, P. M. The mechanism of the Wacker reaction: a tale of two hydroxypalladations. *Angew. Chem., Int. Ed.* **2009**, *48*(48), 9038-9049. DOI: https://doi.org/10.1002/anie.200902194

[7] Jira, R. Acetaldehyde from ethylene—A retrospective on the discovery of the Wacker process. *Angew. Chem., Int. Ed.* **2009**, *48*(48), 9034-9037. DOI: https://doi.org/10.1002/anie.200903992

[8] Wang, C.; Garbarino, G.; Allard, L. F.; Wilson, F.; Busca, G.; Flytzani-Stephanopoulos, M. Low-temperature dehydrogenation of ethanol on atomically dispersed gold supported on $ZnZrO_x$. *ACS Catal*. **2016**, *6*(1), 210-218. DOI: https://doi.org/10.1021/acscatal.5b01593

[9] Guan, Y.; Hensen, E. J. Selective oxidation of ethanol to acetaldehyde by Au-Ir catalysts. *J. Catal.* **2013**, *305*, 135-145. DOI: https://doi.org/10.1016/j.jcat.2013.04.023

[10] Paleti, G.; Peddinti, N.; Gajula, N.; Kadharabenchi, V.; Rao, K. S. R.; Burri, D. R. Direct ethanol condensation to diethyl acetal in the vapour phase at atmospheric pressure over CuNP/SBA-15 catalysts. *New J. Chem.* **2019**, *43*, 10003-10011. DOI: https://doi.org/10.1039/C9NJ02287B

[11] Novaes, L. F.; Liu, J.; Shen, Y.; Lu, L.; Meinhardt, J. M.; Lin, S. Electrocatalysis as an enabling technology for organic synthesis. *Chem. Soc. Rev.* **2021**, *50*, 7941-8002. DOI: https://doi.org/10.1039/D1CS00223F

[12] DiMeglio, J. L.; Terry, B. D.; Breuhaus-Alvarez, A. G.; Whalen, M. J.; Bartlett, B. M. Base-Assisted Nitrate Mediation as the Mechanism of Electrochemical Benzyl Alcohol Oxidation. *J. Phys. Chem. C*, **2021** *125*(15), 8148-8154. DOI: https://doi.org/10.1021/acs.jpcc.0c10476

[13] Kresge, A. J.; Weeks, D. P. Hydrolysis of acetaldehyde diethyl acetal and ethyl vinyl ether: secondary kinetic isotope effects in water and aqueous dioxane and the stability of the ethoxyethyl cation. *J. Am. Chem. Soc.* **1984**, 106(23), 7140-7143. DOI: https://doi.org/10.1021/ja00335a046

[14] Zhang, Q.; Tiefenbacher, K. Hexameric resorcinarene capsule is a brønsted acid: investigation and application to synthesis and catalysis. *J. Am. Chem. Soc.* **2013.** 135(43), 16213-16219. DOI: https://doi.org/10.1021/ja4080375

[15] Zhang, H.; Zhang, W.; Zhao, M.; Yang, P.; Zhu, Z. A site-holding effect of TiO_2 surface hydroxyl in the photocatalytic direct synthesis of 1,1-diethoxyethane from ethanol. *Chem. Commun.* **2017**, *53*(9), 1518-1521. DOI: https://doi.org/10.1039/C6CC09050H

[16] Boennhoff, K.; Obenaus. F. Non-petroleum diesel fuels - based on lower alkyl acetal and/or cyclododecatriene. DE 29 11 411, 1980.

[17] Thavornprasert, K. A.; de la Goublaye de Ménorval, B.; Capron, M.; Gornay, J.; Jalowiecki-Duhamel, L.; Sécordel, X.; Cristol, S.; Dubois, J-L.; Dumeignil, F. Selective oxidation of ethanol towards a highly valuable product over industrial and model catalysts. *Biofuels* **2012**, *3*(1), 25-34. DOI: https://doi.org/10.4155/bfs.11.144

[18]Kresge, A. J.; Weeks, D. P. Hydrolysis of acetaldehyde diethyl acetal and ethyl vinyl ether: secondary kinetic isotope effects in water and aqueous dioxane and the stability of the ethoxyethyl cation. *J. Am. Chem. Soc.* **1984**, *106*(23), 7140-7143. DOI: https://doi.org/10.1021/ja00335a046

[19] Zhang, Q.; Tiefenbacher, K. Hexameric resorcinarene capsule is a brønsted acid: investigation and application to synthesis and catalysis. *J. Am. Chem. Soc.* **2013.** *135*(43), 16213-16219. DOI: https://doi.org/10.1021/ja4080375

[20] Sulaiman, J. E.; Zhu, S.; Xing, Z.; Chang, Q.; Shao, M. Pt-Ni octahedra as electrocatalysts for the ethanol electro-oxidation reaction. *ACS Catal*. **2017**, *7*(8), 5134-5141. DOI: https://doi.org/10.1021/acscatal.7b01435

[21] Hanukovich, S.; Dang, A.; Christopher, P. Influence of metal oxide support acid sites on Cu-catalyzed nonoxidative dehydrogenation of ethanol to acetaldehyde. *ACS Catal*. **2019**, *9*(4), 3537-3550. DOI: https://doi.org/10.1021/acscatal.8b05075

[22] Nutting, J. E.; Rafiee, M.; Stahl, S. S. Tetramethylpiperidine N-oxyl (TEMPO), phthalimide N-oxyl (PINO), and related N-oxyl species: electrochemical properties and their use in electrocatalytic reactions. *Chem. Rev.* **2018**, *118*(9), 4834-4885. DOI: https://doi.org/10.1021/acs.chemrev.7b00763

[23] Hoover, J. M.; Steves, J. E.; Stahl, S. S. Copper (I)/TEMPO-catalyzed aerobic oxidation of primary alcohols to aldehydes with ambient air. *Nat. Protoc.* **2012**, *7*(6), 1161-1166. DOI: https://doi.org/10.1038/nprot.2012.057

[24] Taitt, B. J.; Bender, M. T.; Choi, K. S. Impacts of the Regeneration Pathways of the Oxoammonium Cation on Electrochemical Nitroxyl Radical-Mediated Alcohol

Oxidation. *ACS Catal*. **2019**, *10*(1), 265-275. DOI: https://doi.org/10.1021/acscatal.9b03241

[25] Gong, J.; Mullins, C. B. Selective oxidation of ethanol to acetaldehyde on gold. *J. Am. Chem. Soc.* **2008**, *130*(49), 16458-16459. DOI: https://doi.org/10.1021/ja805303s

[26] Tanaka, T.; Takenaka, S.; Funabiki, T.; Yoshida, S. Selective formation of acetal by photooxidation of ethanol over silica-supported niobium oxide catalysts. *Chem. Lett.* **1994**, *23*(4), 809-812. DOI: https://doi.org/10.1246/cl.1994.809

[27] Chao, Y.; Zhang, W.; Wu, X.; Gong, N.; Bi, Z.; Li, Y.; Zheng, J.; Zhu, Z.; Tan, Y. Visible-light direct conversion of ethanol to 1, 1-diethoxyethane and hydrogen over a non-precious metal photocatalyst. *Chem.-Eur. J* **2019**, *25*(1), 189-194. DOI: https://doi.org/10.1002/chem.201804664

[28] Melchionna, M.; Beltram, A.; Montini, T.; Monai, M.; Nasi, L.; Fornasiero, P.; Prato, M. Highly efficient hydrogen production through ethanol photoreforming by a carbon nanocone/Pd@TiO$_2$ hybrid catalyst. *Chem. Commun.* **2016,** *52*(4), 764-767. DOI: https://doi.org/10.1039/C5CC08015K

[29] Liu, H.; Iglesia, E. Selective oxidation of methanol and ethanol on supported ruthenium oxide clusters at low temperatures. *J. Phys. Chem. B* **2005**, *109*(6), 2155-2163. DOI: https://doi.org/10.1021/jp0401980

[30] Ding, J.; Huang, L.; Ji, G.; Zeng, Y.; Chen, Z.; Eddings, E. G.; Fan, M.; Zhong, Q.; Kung, H. H. Modification of Catalytic Properties of Hollandite Manganese Oxide by Ag Intercalation for Oxidative Acetalization of Ethanol to Diethoxyethane. *ACS Catal.* **2021**, *11*, 5347-5357. DOI: https://doi.org/10.1021/acscatal.1c00505

[31] Gao, P.; Chang, S. C.; Zhou, Z.; Weaver, M. J. Electrooxidation pathways of simple alcohols at platinum in pure nonaqueous and concentrated aqueous environments as studied by real-time FTIR spectroscopy. *J. Electroanal. Chem. Interfacial Electrochem.* **1989**, *272*(1-2), 161-178. DOI: https://doi.org/10.1016/0022-0728(89)87077-9

[32] Liu, Y.; Zhao, S. F.; Guo, S. X.; Bond, A. M.; Zhang, J.; Zhu, G.; Hill, C. L.; Geletii, Y. V. Electrooxidation of ethanol and methanol using the molecular catalyst $[\{Ru_4O_4(OH)_2(H2O)_4\}(\gamma\text{-}SiW_{10}O_{36})_2]^{10-}$. *J. Am. Chem. Soc.* **2016**, *138*(8), 2617-2628. DOI: https://doi.org/10.1021/jacs.5b11408

[33] Serra, D.; Correia, M. C.; McElwee-White, L. Iron and ruthenium heterobimetallic carbonyl complexes as electrocatalysts for alcohol oxidation: Electrochemical and mechanistic studies. *Organometallics* **2011**, *30*(21), 5568-5577. DOI: https://doi.org/10.1021/om101070z

[34] Chung, M.; Jin, K.; Zeng, J. S.; Manthiram, K. Mechanism of Chlorine-Mediated Electrochemical Ethylene Oxidation in Saline Water. *ACS Catal.* **2020**, *10*(23), 14015-14023. DOI: https://doi.org/10.1021/acscatal.0c02810

[35] Behin, J.; Akbari, A.; Mahmoudi, M.; Khajeh, M. Sodium hypochlorite as an alternative to hydrogen peroxide in Fenton process for industrial scale. *Water Res.* **2017**, *121*, 120-128. DOI: https://doi.org/10.1016/j.watres.2017.05.015

[36] Nwaukwa, S. O.; Keehn, P. M. The oxidation of alcohols and ethers using calcium hypochlorite [Ca(OCl)$_2$]. *Tetrahedron Lett.* **1982**, *23*(1), 35-38. DOI: https://doi.org/10.1016/S0040-4039(00)97525-7

[37] Chattaway, F. D.; Backeberg, O. G. CCCLVI.-Alkyl hypochlorites. *J. Chem. Soc., Trans.* **1923**, *123*, 2999-3003. DOI: https://doi.org/10.1039/CT9232302999

[38] Dionigi, F.; Reier, T.; Pawolek, Z.; Gliech, M.; Strasser, P. Design criteria, operating conditions, and nickel-iron hydroxide catalyst materials for selective seawater electrolysis. *ChemSusChem* **2016**, *9*(9), 962-972. DOI: https://doi.org/10.1002/cssc.201501581

[39] Jungkamp, T. P.; Kirchner, U.; Schmidt, M.; Schindler, R. N. UV absorption cross-section data for the hypochlorites ROCl (R = H, CH$_3$, C$_2$H$_5$, i-C$_3$H$_7$, tert-C$_4$H$_9$). *J. Photochem. Photobiol., A* **1995**, *91*(1), 1-6. DOI: https://doi.org/10.1016/1010-6030(95)04074-P

[40] Liu, J.; Ye, J.; Xu, C.; Tong, Y. Kinetics of ethanol electrooxidation at Pd electrodeposited on Ti. *Electrochem. Commun.* **2007**, *9*(9), 2334-2339. DOI: https://doi.org/10.1016/j.elecom.2007.06.036

[41] Consonni, V.; Trasatti, S.; Pollak, F.; O'Grady, W. E. Mechanism of chlorine evolution on oxide anodes study of pH effects. *J. Electroanal. Chem. Interfacial Electrochem.* **1987**, *228*(1-2), 393-406. DOI: https://doi.org/10.1016/0022-0728(87)80119-5

Chapter 3

Rotating Ring-Disk Electrodes Show that Electrochemical Chloride Oxidation in Ethanol Occurs in Multiple One-Electron Steps

Portions of this chapter have been submitted to *Chem. Sci.*

Reprinted from Li, S.; Morrissey, K. H.; Van Daele, R. D.; Bartlett, B. M. *Submitted.*

3.1. Introduction

Electrochemical synthesis, functionalization, and transformations of organic molecules have seen a renaissance in recent years, spurred by an emphasis on green chemistry and insights from energy-relevant catalytic reactions. With various catalysts and redox mediators, mechanisms that would otherwise be impossible to activate can be achieved. In these cases, oxidation and reduction reactions occur by electron transfer reactions on electrodes rather than through stoichiometric chemical reagents.[1] With developments in photovoltaic and photoelectrochemical approaches, electrochemical synthesis also allows renewable energy inputs from solar irradiation.[2] Although, one challenge in organic electrocatalysis is the solubility of both the substrate and the supporting electrolyte necessary to carry out the reaction in an organic solvent. Accordingly, acetonitrile is usually used as the solvent for such applications, not only because of the considerable solubility and conductivity for many electrolytes, but also due to its rather-large redox stability window.[3,4] However, it remains an undesirable solvent both from an environmental, health and safety perspective as well as cost, especially at larger scale processing.[5] On the other hand, short-chain alcohols that can be produced from biomass feedstocks shows promising features, with industrialized biorefineries around the world generating annual production of greater than 10^{10} gallons of bioethanol.[6] Compared to acetonitrile, these small alcohols possess lower viscosity, decent solubility for organic substrates, lower toxicity and better cost efficiency, and may serve as a promising solvent for the synthesis and functionalization for organic compounds.[7,8] Additionally, alcohols may serve as proton source for potential

hydrogen evolution reaction (HER) as well as for hydrogenation reactions.[9,10] This provides potential for coupling the highly desirable HER reaction with the actual anodic reaction of interest.

In the case of bioalcohols, such reaction of interest can yield a range of industry-relevant chemicals, including aldehydes, carboxylic acids, esters and polymer precursors, whether when the alcohols are dissolved substrates or are serving as the solvent.[11] This property allows the bio derivable alcohols to provide an alternative towards petrochemicals, which heavily rely on crude oil cracking and natural gas reforming.[12] Electrocatalytic bioalcohol oxidation also stands as a critical part of the next generation fuel cells, direct alcohol fuel cell (DAFCs), should appropriate electrocatalyst is found.[13] Apart from developing electrocatalysts, mediators are another critical approach for both accelerating the rate and improving the selectivity for electrocatalysis by alternating the mechanism. During anodic reactions, a general scheme involves the following steps: solution-phase mediator diffuses to the anode, electron transfer takes place, then oxidized form of mediator diffuses away. Ideally, these steps should be rapid, and the oxidized form would carry out homogeneous chemical step forming desired product. Thus, sluggish mass transport and adsorption/desorption of the substrate molecules can be circumvented; additionally, direct electron transfer between the anode and the substrate can be avoided, which usually otherwise results in compromised selectivity and electrode passivation.[14,15]

N-oxyl radicals, such as TEMPO, are the most sought-after electrochemical mediators due to their reversible kinetics and selectivity control.[16,17] Yet, as a rather-unstable organic compound, it doesn't suit well for larger scale practices due to concerns in cost and environmental impact. To promote usage of low-cost, non-toxic mediators, our group has explored nitrate ($NO_3^-/NO_3^{\bullet}$) and chloride ($Cl^-/HClO$) as accessible inorganic mediators for alcohol oxidation reactions.[18,19] In acetonitrile solvent, however, it is found that nitrate radical leads to H-atom abstraction from the solvent itself, and that this reaction consumes nitrate irreversibly.[20] In water, chloride can be oxidized to HClO then homogeneously oxidize ethanol and 2-propanol, but with compromised selectivity for the 2-electron oxidation product due to overoxidation. Recently, we discovered that chloride mediated ethanol oxidation can be carried out under solvent free conditions, selectively forming 1,1-diethoxyethane (DEE) as the 2-electron product. Key to this mechanism is the formation

of EtOCl intermediate from chloride oxidation, which is known to be a strong oxidant and functionalization reagent yet degrades spontaneously.[21] Although in this work, EtOCl is not utilized as an oxidant, its oxidizing nature provides the impetus of studying its reactivity through RRDE approaches.

Chloride oxidation generates strong oxidants or chlorinating agents. Under aqueous conditions, Cl_2, HClO, ClO^- can be produced depending on the pH, and related electrochemical mechanisms are well established.[22,23] Another recent work on chloride-mediated ethanol conversion in water indicates that chlorine radicals are produced and subsequently attack the α or β H of ethanol, yielding acetic acid or ethylene oxide as product, respectively.[24] However, as mentioned earlier, in neat ethanol, EtOCl is observed as the sole product from chloride oxidation reaction (COR), hinting a completely different mechanism. Here, a hydrodynamic kinetics study on electrochemical COR in ethanol is carried out and a reaction mechanism for this newly discovered anodic reaction is proposed.

3.2. Experiments

3.2.1. Chemicals and Materials

Tetrabutylammonium chloride (Bu4NCl, ≥97.0%, Sigma-aldrich, recrystalized), Tetrabutylammonium trifluoromethanesulfonate (Bu4NOTf, >98.0%, Fisher), Tetrabutylammonium hexafluorophosphate (Bu4NPF6, ≥98.0%, TCI, recrystalized), ethanol (200 proof, Fisher), dichloromethane (Stabilized/Certified ACS, Fisher), were purchased and used as described. Ferrocene (98%, Sigma) is purified by sublimation at 120 ºC on a hot plate.

3.2.2. Electrochemical Measurements

All electrochemical measurements were carried out on a CHI760E electrochemical workstation (CH Instruments) if not specifically stated. All electrochemical data is plotted under IUPAC convention. Rotating ring-disk electrode measurements (RRDE) are carried out by RRDE-3A (ALS Japan) connected to the CHI760E. For all the RRDE measurements, a 3-electrode setup is used, where Ag wire is used as a pseudo reference electrode, Pt wire (Surepure Chemetals, 0.05 cm diameter, with 2 cm submerged, resulting with ~0.314 cm^2 surface area) is mounted to a piece of copper wire sealed in a glass tube and is used as the

counter electrode. The working electrodes for RRDE analysis are also purchased from ALS Japan (013336, DRE-PGK Pt ring/GC disk replaceable electrode kit). The Pt ring and GC disk are polished separately, first with 0.3-micron alumina, then with 0.05-micron alumina on nylon polishing pads (Buehler). The GC disk is planar with a diameter of 4 mm. The disk is then surrounded with a ring of insulating Teflon (OD: 5mm; ID: 4mm) on the same vertical level, along with the Pt ring (OD: 7mm; ID: 5mm).

The RRDE assembly, including its protective shell, has an overall diameter of 12 mm. The Ag wire reference electrodes were purchased from CH Instruments as well (CHI112P), but the glass frit attached is replaced with a more compact glass frit with plastic seals (Gamry, 955-00003). The solution in which the Ag wire is soaked is kept identical to the electrolyte in the cell. PTFE stir bars, when used, are purchased from Fisher with a length of 12.7 mm and a diameter of 3.2 mm. The single-compartment electrochemical cell specifically for RRDE measurements is also purchased from ALS Japan. All RRDE measurements are conducted on the CHI760E, where the disk electrode is always the working electrode with green wiring, and the ring electrode is always secondary electrode with yellow wiring. If not specified, the working electrode always performs oxidation and the secondary electrode always performs reduction.

To calibrate the pseudo reference electrode to ferrocene redox couple, the exact solution of interested is replicated but with an additional 10 mM ferrocene dissolved. Then with the same set of working/reference/counter electrodes as the RRDE measurement, a CV with a scan rate of 50 mV / s is carried out between $0 - 1$ V to obtain the redox potentials of $Fc^{+/0}$ redox couple by calculating the average of both the oxidation and reduction peak potential. Note that during $Fc^{+/0}$ calibrations, the Pt ring is not connected to workstation and thus no current is recorded. All RRDE electrolyte solutions are prepared in volumetric glassware and each measurement, 50 mL of electrolyte is poured into the reaction cell. Solution deoxygenation is not required due to a lack of difference observed w/ or w/o N_2 sparging. All voltammetry measurements are performed at room temperature with IR compensation applied in the CHI760E.

3.2.3. UV-Vis Measurement and Spectroelectrochemical Analysis

The UV-Vis spectroelectrochemical measurement is carried out with a CHI1000C electrochemical workstation (CH instrument), Agilent Cary 5000 UV-Vis-NIR spectrophotometer and a custom-built spectroelectrochemical cell. For wavelength scan measurements, the measurement is carried out with a zero-baseline calibration in absorption mode, where zero is collected from atmosphere and baseline is collected from the identical electrolyte solution. The wavelength scan step size is 0.5 nm, and the range is 500 nm – 200 nm. A 3-electrode system similar to that described in the RRDE set-up is used, where the working electrode is a planar glassy carbon disk purchased from CH Instrument (CHI104P) with a diameter of 3.0 mm. For kinetic measurements, the measured wavelength is held at 237 nm while a linear sweep voltammetry measurement is run on the potentiostat. Following each measurement, the electrolyte post-electrolysis is replaced with fresh electrolyte. Detailed information and a photograph of the spectroelectrochemical setup is presented in **Figure B.1**.

3.2.4. Gas Chromatography Quantification

Selective 2-electron oxidation of ethanol will result in the detection of 1,1-diethoxyethane (DEE) as product by gas chromatography. However, if 4-electron (over)oxidation occured, one would expect to observe acetic acid and/or ethyl acetate. Constant potential coulometry (CPC) is applied to access the oxidation products. The CHI760E potentiostat and a 3-electrode setup is used in all CPC experiments, where a glassy carbon disk electrode (CHI104P, surface area: 0.07 cm^2) is used as the working electrode, and same reference/counter electrodes in the previous sessions are used. The electrochemical cell is a custom-made 2-compartment glass cell with a glass frit as the separator. The potential applied was held at 1.91 V and 2.41 V vs Fc$^{+/0}$, where the former represents the highest potential of interest in this work; the latter represents the case where overoxidation occurs. CPC electrolysis was carried out with constant stirring (600 rpm) until a significant quantity of charge is passed for accurate detection of products.

The GC sample is prepared by performing a 10-fold dilution of the post-CPC solution with EtOH. In the sample, 2 mM toluene is added as an internal standard. The GC measurement is then carried out with a ThermoFisher Trace 1310 gas chromatograph

equipped with a capillary column and flame ionization detector (FID). During analysis, the column oven was warmed from 40 to 200 °C at a 10 °C min^{-1} ramp rate.

3.3. Results

3.3.1. Detection of Chlorine(0) Adsorption on Glassy Carbon

The reactions of interest are COR reaction based on the previous chapter:

$$Cl^- + CH_3CH_2OH \rightarrow CH_3CH_2OCl + H^+ + 2e^- \qquad (3.1)$$

$$CH_3CH_2OCl \rightarrow CH_3CHO + H^+ + Cl^- \qquad (3.2)$$

Reaction 3.1 requires applied potential at the glassy carbon electrode and oxidizes chloride anion by 2 electrons. Reaction 3.2 instead, is a purely chemical step where EtOCl decomposes spontaneously to form acetaldehyde and regenerate chloride anion. As the applied potential increases, however, the direct electrochemical ethyl alcohol oxidation reaction (AOR) can also proceed:

$$CH_3CH_2OH \rightarrow CH_3CHO + 2H^+ + 2e^- \qquad (3.3)$$
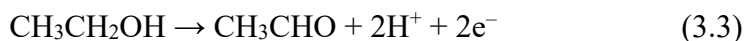
Understanding that COR appears to proceed faster with lower overpotential, we propose that reaction 3.1 proceeds through 2 discrete 1-electron steps: first, a Volmer step where chloride adsorbs; then an outer-sphere reaction happens between adsorbed chlorine and the ethanol solvent. This proposed reaction mechanism is illustrated in **Figure 3.1**:
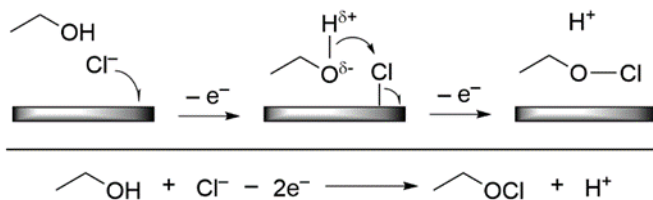
Figure 3.1: Proposed step-by-step mechanism of chloride oxidation reaction in neat ethanol on glassy carbon electrode.

To certify the hypothesis, we carried out CV in a 10 mM [Cl⁻] solution in dichloromethane (DCM), considered as an inert, aprotic and polar solvent compared to ethanol. **Figure 3.2** shows the CV curves on glassy carbon electrode with varied scan rates.
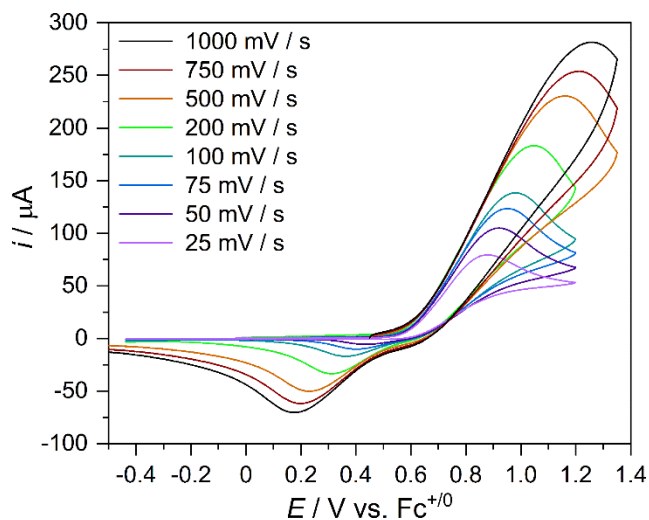
Figure 3.2: CV traces at varying scan rate for 10 mM Bu$_4$NCl and 90 mM Bu$_4$NPF$_6$ dissolved in DCM.

An irreversible redox couple is observed at ~0.6 V. Through analyzing the scan rate – peak current dependence, insights on reaction mechanism can be obtained. **Figure 3.3** shows such dependence on both the anodic and cathodic peak in **Figure 3.2**.
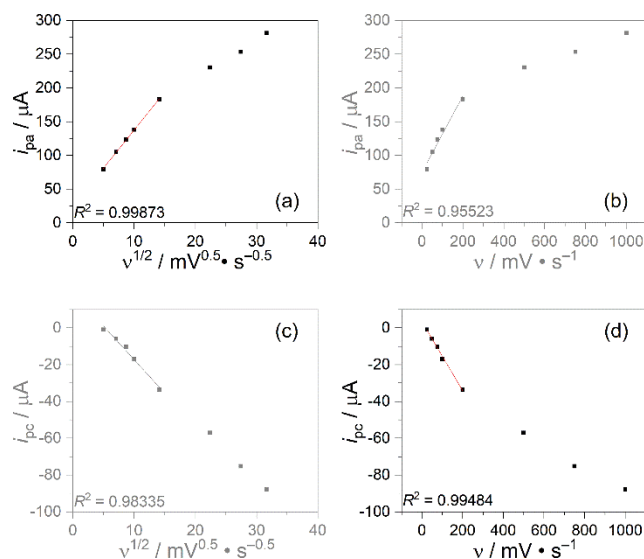
Figure 3.3: Relationship of peak currents from the CV traces in Figure 3.2 and either the square root of scan rate or first order of scan rate.

From panels (a), (d) and the respective R^2 value, the peak current of the anodic wave (i_{pa}) shows a linear relationship with the square root of scan rate, reflecting a diffusion-limited reaction. This likely represents the reaction with solution-phase chloride. However, the peak current of the cathodic wave (i_{pc}) shows a linear relationship with the first order of scan rate, representing a surface adsorption-limited reaction, which can arise from the reduction of the surface adsorbed Cl(0) species. Such pattern is also observed for 100 mM

Bu₄NCl trials where the cathodic peak current also revealed linearity to first order of scan rate (**Figure B.2**). Note that at rather fast scan rate, deviation from linearity is expected due to the absorption/desorption equilibrium being fast and that the reaction is no longer surface confined. Additionally, at fast scan rates, the solution internal resistance (iR) can produce a higher distortion to the shape of the CV curves, resulting in inaccuracy. Thus, only the relationship between i_p and slower scan rates are considered. [25,26] These observations are similar to those observed in water, where a Volmer step results in absorbed chloride.[27,28] Upon scanning to more positive potential, a second redox couple centered at ~1.5 V is observed, as is shown in **Figure 3.4**. For this redox feature, a linear $i_{pa} - v$ relationship is also observed for its anodic peak, indicating again, an adsorbed species. This further supports the hypothesized Volmer step on GC, where the subsequent oxidation of the adsorbed Cl(0) species proceeded at this higher potential. It is noteworthy that in the control CV experiment with only Bu₄NPF₆ in DCM, no redox wave is observed (**Figure B.3**), highlighting that all the redox features arise form chloride-related chemistry.
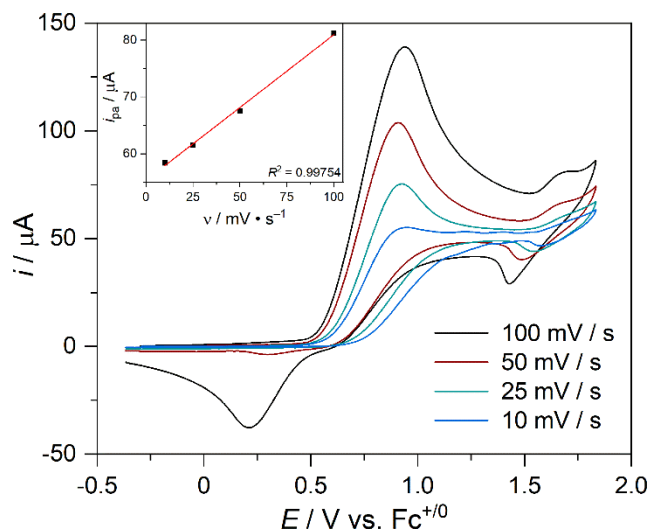
Figure 3.4: CV scans to higher potential at varying scan rate for 10 mM Bu₄NCl and 90 mM Bu₄NPF₆ dissolved in DCM.

3.3.2. Rotating Ring-Disk Electrode (RRDE) Analysis of COR in Ethanol

With the previous section supporting chloride absorption as a plausible step on GC electrode, we move on to assessing the COR in ethanol with a hydrodynamic study, accomplished by RRDE. To start, we assessed our RRDE set-up by measuring the collection efficiency (N) by using the standard $[Fe(CN)_6]^{3-/4-}$ redox couple. **Figure B.4**

shows the corresponding LSV curves under different rotation rate, and N was measured with the following equation:[29]

$$N = \left| \left(\frac{i_{ring}}{i_{disk}} \right) \left(\frac{n_{ring}}{n_{disk}} \right) \right| \times 100\% \qquad (3.4)$$

Where n corresponds to the number of electrons transferred at the disk and at the ring (both equal to 1 for $[Fe(CN)_6]^{3-/4-}$) and i corresponds to the mass-transport limiting current. N is thus determined to be 39.9 % by averaging out the values obtained from the experiments. This agrees with the theoretical value of 42.4 % based on the dimensions of the RRDE setup, provided by the vendor of the instrument. **Figure 3.5** shows the LSV with the same electrode setup, but in our ethanol oxidation scheme with either 100 mM [Cl⁻] or no chloride available. Note that in this case, Bu₄NOTf is considered stable and non-oxidizable, as a supporting electrolyte. In this case, positive, scanning bias is applied on the glassy carbon disk, while a constant negative bias is applied on the Pt ring ($E_{ring} = -0.4$ V) to reduce oxidative species generated on the disk.
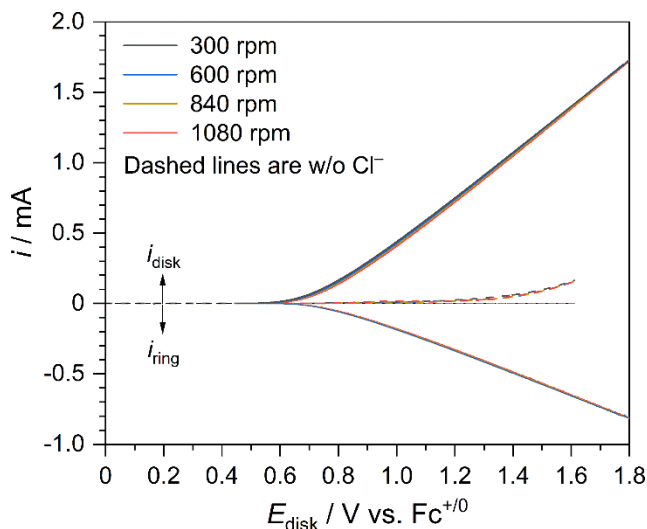
Figure 3.5. RRDE LSV (i - E_{disk}) with a GC-disk and Pt-ring in 100 mM electrolyte in EtOH solvent. The solid lines are Bu₄NCl electrolyte, and the dashed lines are the Bu₄NOTf control experiment. The scan rate is 20 mV/s.

Neglectable disk current is observed for the Bu₄NOTf case before > 1.2 V applied, with virtually no ring current even at those high potentials. However, for chloride electrolyte, significant anodic and cathodic current can both be observed starting from 0.6 V. This certifies generation of an oxidizing species upon COR in ethanol. However, no visible difference is observed among rotation rates, nor is there a limiting current. These results

41

hint that 100 mM Bu₄NCl provides sufficiently high concentration that the current will always be rate limited, rather than mass transport limited. To further study the competition between AOR and COR at higher potential, we carried out the RRDE LSVs with a much lower concentration of Bu₄NCl. **Figure 3.6** shows the LSVs with 5 mM Bu₄NCl and 100 mM Bu₄NOTf (added for conductivity purposes), where the scale of y-axis is very different. In this case, we do observe current increase as rotation rate increases, yet still no limiting current is observed. It is concluded that the direct AOR will proceed before COR could reach its limiting current. With the trend of disk current and rotation rate, Koutecky-Levich analysis can be carried out to understand the kinetic details of the reaction.
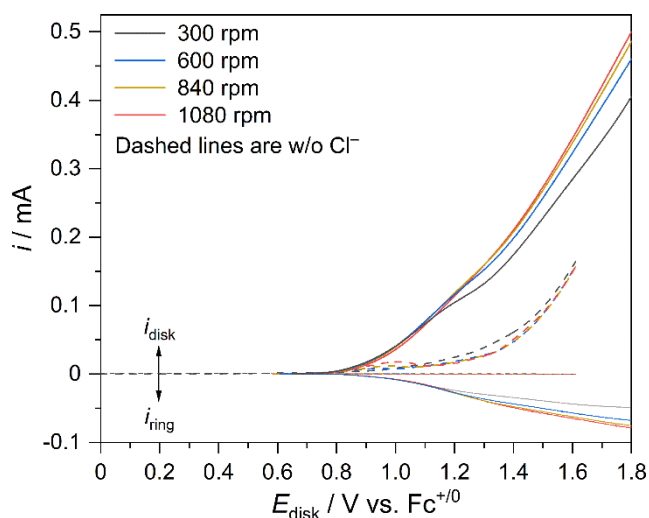
Figure 3.6. RRDE LSV (i - E_{disk}) with a GC-disk and Pt-ring in 100 mM Bu₄NOTf electrolyte in EtOH solvent. The solid lines are with 5 mM Bu₄NCl electrolyte added. The scan rate is 20 mV/s.

3.3.3. Koutecky-Levich (K-L) Analysis of COR in Ethanol

To fully assess the relationship between anodic current and rotation rate (that dictates mass transport at low Cl⁻ concentration), we carried out RRDE LSVs with a wider range of rotation rate between 60 and 3000 rpm, shown in **Figure 3.7**.
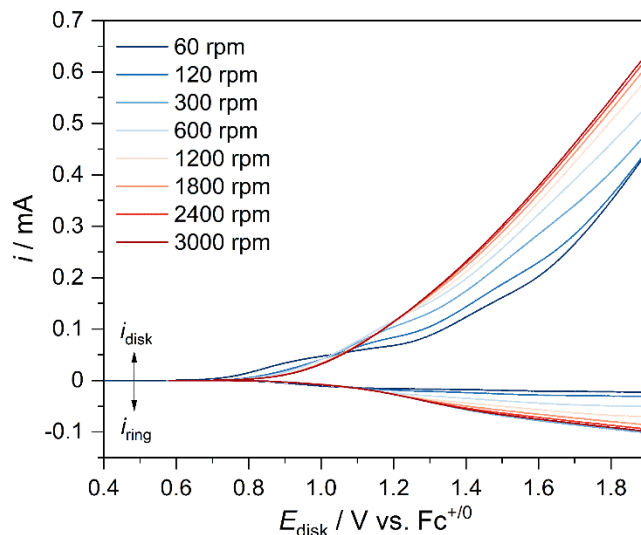
Figure 3.7. RRDE LSV (i - E_{disk}) with a GC-disk and Pt-ring in 5 mM Bu₄NCl and 100 mM Bu₄NOTf electrolyte in EtOH solvent. The scan rate is 20 mV/s and E_{ring} is poised at –0.4 V vs. Fc$^{+/0}$.

From this experiment, noticeable differences can be observed between 1.1 V and 1.6 V. First, multiple waves appear in the disk current at lower rotation rate yet disappear as rotation rate reaches 1200 rpm. A crossover point can be seen at 1.1 V as well, when the kinetic current rises faster with increasing potential. It is noteworthy that this is also the potential where ring current arises. The above observations are consistent with the scenario where a chloride absorption at lower potential (with minimal ring current observed) with subsequent ethanol-involved reaction proceeds at higher potential. The increase of current with rotation rate also indicates that COR is kinetically faster than AOR, and will dominate the current, should a sufficient mass transport be provided. Finally, the disk current measured for 2400 and 3000 rpm is very similar, indicating that the range of rotation rate selected is appropriate.

Based on the above experiment, to better understand the kinetic details of the reaction, we carried out K-L analysis in the 5 mM Bu₄NCl solution. Such analysis is based on the following equation:

$$\frac{1}{i} = \frac{1}{i_k} + \left(\frac{1}{0.62nFAD^{\frac{2}{3}}v^{-\frac{1}{6}}C} \right) \omega^{-\frac{1}{2}} \qquad (3.5)$$

Where i is the measured current, i_k is the kinetic current (assuming mass-transport is not limiting), n is the number of electrons transferred, F is Faraday's constant (96,485 C/mol), A is the electrode surface area (0.126 cm²), D is to the diffusion coefficient of the analyte

(1.52 × 10^{-6} cm^2/s for chloride in EtOH; 1.01 × 10^5 cm^2/s for EtOH itself),[30] v is the kinematic viscosity of EtOH (1.391 × 10^{-2} cm^2/s),[31] C is the bulk concentration of the analyte in mol/cm^3 and ω is the rotation rate of the electrode (rad/s). D_{Cl^-} is not available in the literature, and is measured instead *via* a Cottrell experiment shown in **Figure B.5**. Guided by equation 3.5, **Figure 3.8** shows the linear plots of i^{-1} vs. $\omega^{-1/2}$ among varied potentials. In this graph, i_k is determined from the intercept and n is assumed to be 2 for the net reaction. The analysis is based on the underlying assumptions: EtOCl, the oxidized species, has a similar diffusion coefficient as chloride anion; decomposition of EtOCl is negligible due to its low concentration compared to the bulk chloride concentration. For all the potential analyzed, good linearity is observed for the high-frequency region where ideal RDE response is determined by mass-transport. We believe that the derivation of linearity at low frequency region is due to the lack of dependence on mass-transport, where direct AOR acts as an interference due to the insufficient chloride available. Slight curvature near the high frequency region is known to be due to regeneration of the disk-reactant.[32,33] In our case, the slow spontaneous decomposition of EtOCl can cause a similar recycling effect.
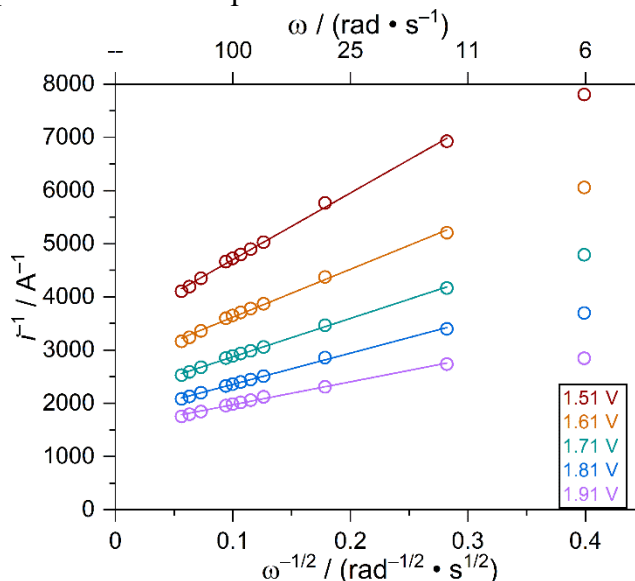
Figure 3.8. K-L plot of 5 mM Bu$_4$NCl in neat ethanol across various potentials and rotation rates. The LSV scan rate is 20 mV/s.

From the kinetic current determined by **Figure 3.8**, we can then determine the kinetic rate constant for the forward (oxidation) reaction, k_f, based on the following equation:

$$i_k = k_f n F A C^m \qquad (3.6)$$

Where *m* is the apparent reaction order, measured from a separate experiment shown in **Figure B.6** and numeric results are listed in the Appendix. Similarly, reaction 3.6 is applied to the 100 mM Bu$_4$NOTf case, where AOR proceeds (since ethanol is the solvent, *m* is considered as zero and the current is considered kinetic current due to sufficient reactant without mass-transport limit, especially with conviction). This is also confirmed by the observed result that the current for AOR does not change with ω. To confirm that the AOR reaction is strictly limited to the 2-electron reaction 3.3, we carried out gas chromatography to certify the oxidation product by applying a constant potential coulometry (CPC) experiment at 1.91 V, highest potential of this analysis, and 2.41 V which is a rather high potential with higher risk of overoxidation. **Figure B.7** shows the GC chromatogram for both conditions, where for 1.91 V only DEE is detected as a product, confirming that only 2-electron reaction proceeds at this potential. With those considerations, **Figure 3.9** shows the trend of $\log_{10}(k_f)$ vs E for electrolytes with 0-20 mM [Cl$^-$] in ethanol. Note that the ionic strengths among the datapoints are kept the same by maintaining a total of 100 mM salt concentration between Bu$_4$NCl and the inert Bu$_4$NOTf.
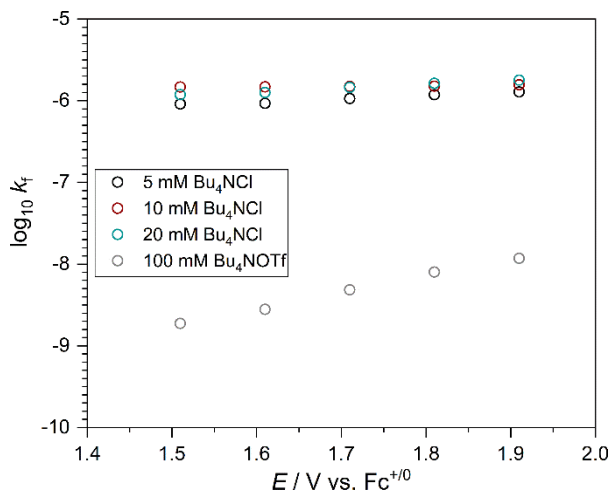
Figure 3.9. Trend of kinetic rate constant for the forward reaction (cm/s) with potential applied. Numerical data is included in the Appendix.

Numerically, rate constant for COR (~10^{-6} cm/s with good agreement between concentrations) is measured to be 2-3 magnitudes larger than that for AOR (10^{-9} to 10^{-8} cm/s). This result also agrees with the observation that COR is kinetically faster than AOR and dominates the current when sufficient mass-transport is provided.

3.3.4. Reaction Pathway Analysis by LSV

Additionally, conviction-free LSV experiments are carried out among different concentrations of chloride. With the same constant ionic strength compensated by Bu$_4$NOTf, **Figure 3.10** shows the measured LSV curves for 0 - 100 mM chloride.
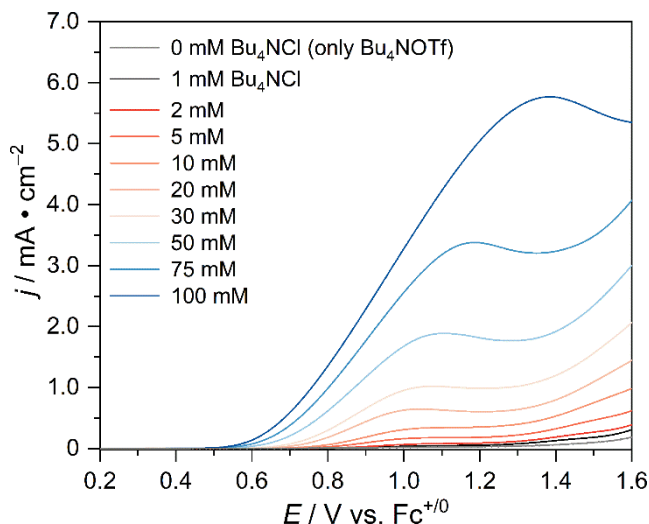
Figure 3.10. LSV curves on a GC disk in varying chloride concentration. The scan rate is 5 mV / s. The control experiment with no chloride is also included (gray) for comparison.

From this quiescent experiment, a concentration dependent $j – E$ profile is observed. With the presence of chloride, 2 oxidation events can be observed with either a plateau ($\leq$10 mM Cl$^-$) or an inflection point ($\geq$ 20 mM Cl$^-$) between them. Similar to the $j – E$ response in DCM, we attribute the first event to the absorption of Cl$^-$ and the second step to the electron transfer with the Cl^0 and the ethanol solvent involved, *en route* to forming EtOCl. In the same fashion, one would expect the first step to be diffusion-limited even in ethanol, and this is verified by **Figure B.8** where the expected linear relationship between peak current and square root of scan rate is seen. Since this step determines the available Cl^0 at the surface, it also affects the second step. At low surface coverage, diffusion-limited flux of reactant leads to the curvature in the LSV trace as potential increases. At higher surface coverage, the second step also show increased current. For the 50 mM Bu$_4$NCl case with clear distinguishable redox features, varied scan rate CVs were carried out (**Figure B.9**) to further understand the kinetic profile. At 5 or 10 mV/s scan rate, no cathodic return wave is observable due to the transient lifetime of EtOCl; while the return wave is observable for faster scan rates, greater than 1 V split between the anodic and

cathodic is seen, indicating an irreversible reaction. In such case, the peak current can be estimated by:[29]

$$i_p = (2.99 \times 10^5) n^{3/2} \alpha^{1/2} A D_{Cl}^{1/2} C_{Cl}^* v^{1/2} \qquad (3.7)$$

Where i_p is the observed peak current in A, v is the scan rate in V/s, α is estimated to be 0.5, with other parameters inherited from the previous calculations. **Figure 3.11** shows the scatter plot of i_p recorded among various scan rate values, alongside predicted i_p from the above equation for both $n = 1$ and $n = 2$ cases. It can then be seen that the measured results have a better alignment with $n = 1$ case with both similar current value and trend, agreeing to the proposed mechanism.
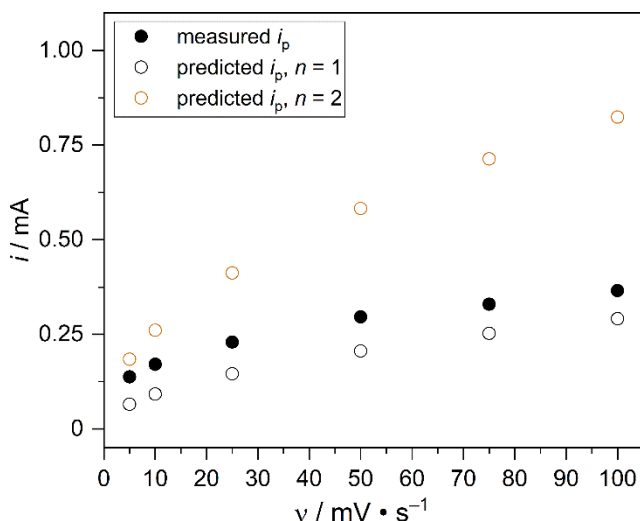
Figure 3.11. Measured vs. predicted peak current vs. scan rate plot for 50 mM Bu₄NCl in 50 mM Bu₄NOTf supporting electrolyte.

3.4. Discussion

The product of 2-electron COR in water is usually Cl_2, HClO and ClO^-, depending on the pH of the solution. These 2-electron reactions are usually found to be kinetically faster on various materials compared to the oxygen evolution reaction (OER), which is a 4-electron reaction.[34] However, in ethanol, the competing reactions are the direct AOR reaction, which is also 2-electron, same as the amount of electron transferred in the formation of EtOCl. Thus, the significant faster rate observed can be attributed to our proposed 2 1-electron steps with similar overpotential, where the kinetics are favourable due to the attraction of charged & partially charged species in the proposed mechanism. Unlike in DCM where the solvent is considered innocent, ethanol participates in the second

step, lowering the overpotential by avoiding another chloride anion to diffuse and absorb onto the surface. Additionally, the lack of chlorinated product further indicates that active chlorine is never present in solution throughout the COR process. All electrochemical analyses are carried out without the addition of either Brønsted acid or base, thus only negligible amount of ethoxide anion ($1.122 * 10^{-8}$ M) is expected considering the autoionization constant of ethanol.[35] As a result, in all tests, anions from the added salt are considered as the dominating anionic species.

The work in Chapter 2 understood that EtOCl has a characteristic UV-vis absorption profile. **Figure 3.12** shows the UV-vis spectroelectrochemical absorption measurement carried out throughout the potential assessed in this chapter.
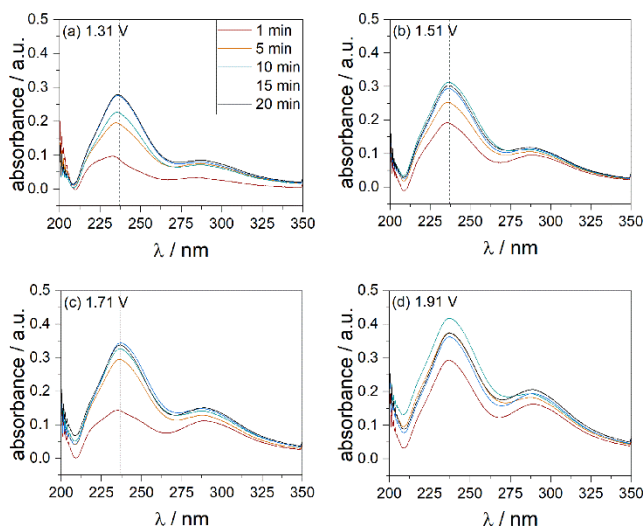
Figure 3.12. Spectroelectrochemical measurement of 100 mM Bu₄NCl solution poised at different constant potential in a custom cell. Vertical lines in each figure correspond to wavelength = 237 nm. UV-vis absorption measurement of the electrolyte is carried out every minute while the CPC proceeds for 20 mins. Only selected timepoints of measurement are shown for clarity.

These measurements are carried out to test the plausibility of the previous measurement. For all trials listed in **Figure 3.12**, a custom spectroelectrochemical cell is used, and the background of the UV-vis absorption measurements is the identical electrolyte solution with no charge passed. Over 20 minutes of CPC, the only spectrochemical difference observed among electrolytes under varied potentials is the intensity of the absorbance. This confirms the formation of a single COR product throughout the potential range studied. It is also observed that the concentration of such species undergoes a steady build-up region before oscillating around a steady state level, agreeing with what is observed in Chapter 2.

Notably, the higher potential applied, the faster such steady state is reached. To confirm that the absorption features arise only from COR, a control reaction with only Bu₄NOTf as the electrolyte is carried out and no visible feature is observed, as can be seen in **Figure B.10**. With such information in mind, we then carried out another spectroelectrochemical measurement, where instead of CPC, an LSV experiment is performed with rather slow scan rate (1 mV/s). Additionally, rather than performing wavelength-scan experiment, the UV-vis spectrophotometer is charged to continuously measure the absorption value at 237 nm, the absorption maxima of EtOCl, during the LSV. **Figure 3.13** shows the LSV-absorption measurement result.
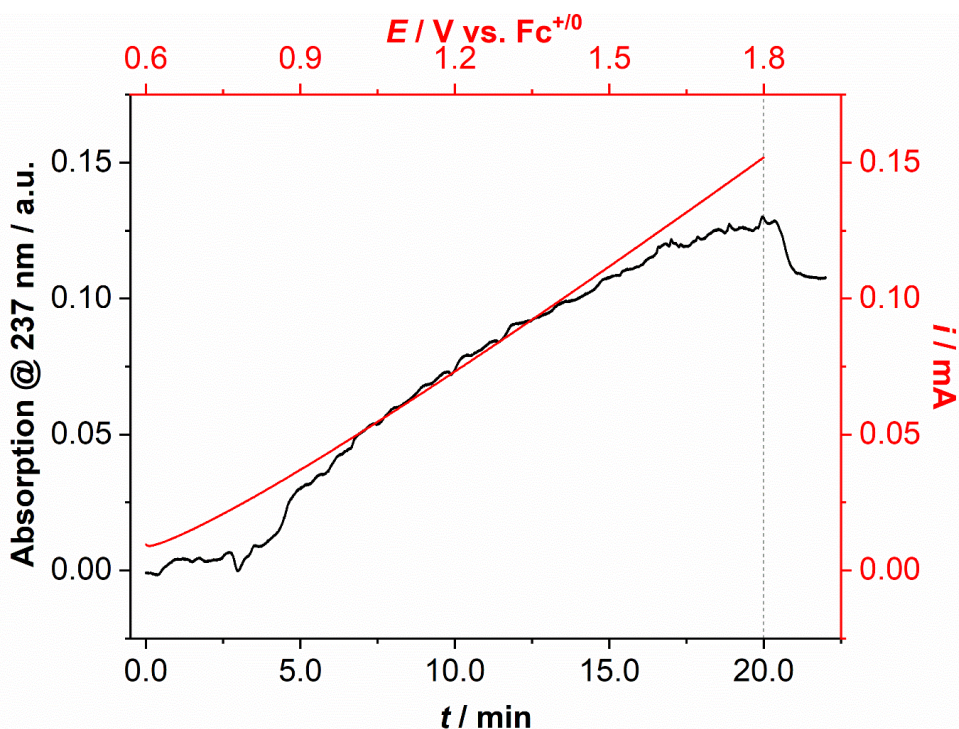
Figure 3.13. Spectroelectrochemical identification of EtOCl generation by linear sweep voltammetry in 100 mM Bu₄NCl electrolyte. LSV scan rate: 1 mV/s; UV-vis absorption wavelength: 237 nm. The LSV and UV-vis measurement starts at the same time and are designed in the ways that the top and bottom axis are aligned in time. The LSV experiment stops when the time axis reaches 20.0 minutes, thus a drop is observed in absorption due to spontaneous degradation of EtOCl.

In this analysis, the background is also the identical electrolyte solution with no charge passed. One can then clearly observe the rapid buildup of the black curve (proportional to [EtOCl]) starting near 5.0 min or 0.9 V. Despite the anodic current observed before such potential, minimal amount of EtOCl is made, confirming the presence of a lower-potential

step with only 1 electron transferred thus no EtOCl can be formed. This agrees with our proposed mechanism. Further, by referring back to RRDE analysis, this spectroelectrochemical observation is corroborated by the RRDE results shown in **Figure 3.14**.
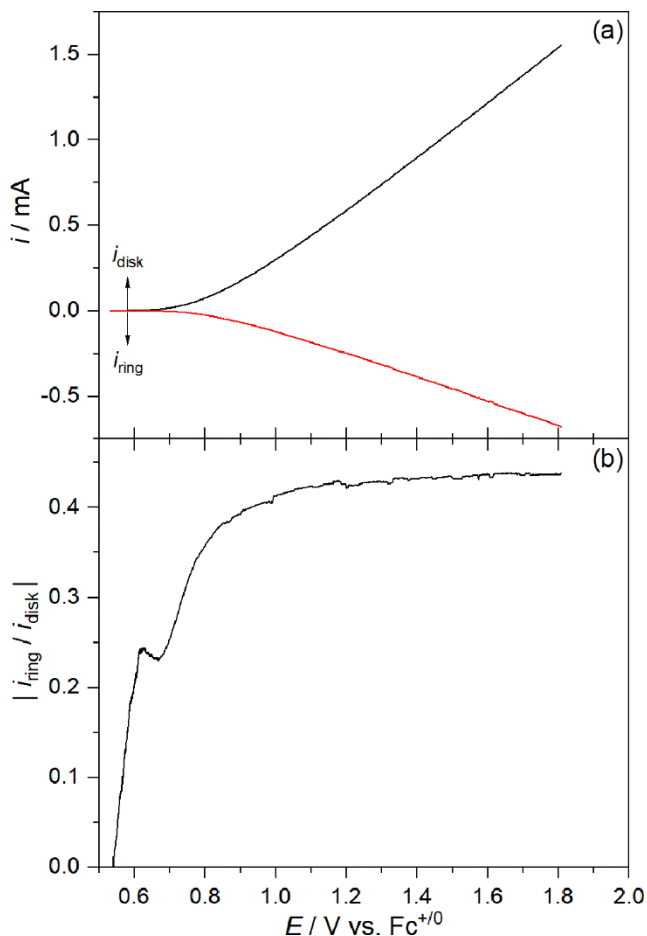
Figure 3.14. (a) RRDE LSV with Pt-ring and GC-disk in 100 mM Bu$_4$NCl with rotation rate = 3000 rpm. The scan rate is 1 mV/s and Ering is poised at –0.4 V vs. Fc$^{+/0}$; (b) The measured current ratio from the RRDE LSV.

With a chloride-rich electrolyte and very fast rotation rate on the RRDE, we anticipate efficient EtOCl generation that AOR is outcompeted. With the rather slow scan rate (1 mV/s), we hope to elucidate the potentials where EtOCl are produced by monitoring the ring/disk current ratio. The (b) part of Figure 3.14 shows that it is not until 0.9 V and above that the current ratio reached a similar level to the measured collection efficiency. The lower-than-expected ratio before 0.9 V can be attributed to a smaller-than-expected ring current, resulting from the lack of EtOCl to reduce. This result agrees with the observation

50

from **Figure 3.13** where a one-electron step is present before 0.9V where no EtOCl is made, supporting the hypothesized mechanism.

3.5. Conclusions

This chapter provides mechanistic insight to the chloride-mediated neat ethanol oxidation reaction to 1,1-DEE by utilizing a series of electroanalytical approaches and spectroelectrochemical studies. In inert solvent DCM, current responses and peak current analysis agree with the presence of a Volmer step, where Cl^0 is produced from a 1-electron oxidation and adsorbed onto the glassy carbon surface. In ethanol, a second step involving solvent molecule then proceeds, oxidizing the Cl^0 to form EtOCl, where the chloride possesses a +1-oxidation state. Koutecky-Levich analysis with RDE quantified the kinetic rate constant of the chloride mediated reaction as well as the direct alcohol oxidation reaction, with the former being 2-3 magnitudes larger than the direct pathway. Spectroelectrochemical measurements confirm that the chloride oxidation reaction yields one sole product throughout the potential of interest, as well as discovering the first electron transfer step in ethanol where no EtOCl is observed with the *in situ* experiment. Future work includes applying this hydrodynamic analysis towards other neat alcohol systems, carrying out *in situ* IR measurements at the surface to track the formation and presence of adsorbed species on carbon-based electrode materials, and finally develop more materials capable of performing this mechanism with faster kinetics than carbon.

3.6. References

[1] You, B.; Sun, Y. Innovative strategies for electrocatalytic water splitting. *Acc. Chem. Res.* **2018**, *51*(7), 1571-1580. DOI: https://doi.org/10.1021/acs.accounts.8b00002

[2] Chen, J.; Dong, C.; Idriss, H.; Mohammed, O. F.; Bakr, O. M. Metal halide perovskites for solar-to-chemical fuel conversion. *Adv. Energy Mater.* **2020**, *10*(13), 1902433. DOI: https://doi.org/10.1002/aenm.201902433

[3] Jing, Q.; Moeller, K. D. From molecules to molecular surfaces. Exploiting the interplay between organic synthesis and electrochemistry. *Acc. Chem. Res.* **2019**, *53*(1), 135-143. DOI: https://doi.org/10.1021/acs.accounts.9b00578

[4] Siu, J. C.; Fu, N.; Lin, S. Catalyzing electrosynthesis: a homogeneous electrocatalytic approach to reaction discovery. *Acc. Chem. Res.* **2020**, *53*(3), 547-560. DOI: https://doi.org/10.1021/acs.accounts.9b00529

[5] Capello, C.; Fischer, U.; Hungerbühler, K. What is a green solvent? A comprehensive framework for the environmental assessment of solvents. *Green Chem.* **2007**, *9*(9), 927-934. DOI: https://doi.org/10.1039/B617536H

[6] Prasad, R. K.; Chatterjee, S.; Mazumder, P. B.; Gupta, S. K.; Sharma, S.; Vairale, M. G.; Datta, S.; Dwivedi, S. K.; Gupta, D. K. Bioethanol production from waste lignocelluloses: A review on microbial degradation potential. *Chemosphere* **2019**, *231*, 588-606. DOI: https://doi.org/10.1016/j.chemosphere.2019.05.142

[7] Tekin, K.; Hao, N.; Karagoz, S.; Ragauskas, A. J. Ethanol: A promising green solvent for the deconstruction of lignocellulose. *ChemSusChem* **2018**, *11*(20), 3559-3575. DOI: https://doi.org/10.1002/cssc.201801291

[8] Zijlstra, D. S.; Lahive, C. W.; Analbers, C. A.; Figueirêdo, M. B.; Wang, Z.; Lancefield, C. S.; Deuss, P. J. Mild organosolv lignin extraction with alcohols: the importance of benzylic alkoxylation. *ACS Sustainable Chem. Eng.* **2020**, *8*(13), 5119-5131. DOI: https://doi.org/10.1021/acssuschemeng.9b07222

[9] Zweifel, T.; Naubron, J. V.; Büttner, T.; Ott, T.; Grützmacher, H. Ethanol as hydrogen donor: highly efficient transfer hydrogenations with rhodium (I) amides. *Angew. Chem., Int. Ed.* **2008**, *47*(17), 3245-3249. DOI: https://doi.org/10.1002/anie.200704685

[10] Weng, B.; Quan, Q.; Xu, Y. J. Decorating geometry-and size-controlled sub-20 nm Pd nanocubes onto 2D TiO_2 nanosheets for simultaneous H_2 evolution and 1, 1-diethoxyethane production. *J. Mater. Chem. A*, **2016**, *4*(47), 18366-18377. DOI: https://doi.org/10.1039/C6TA07853B

[11] Holade, Y.; Guesmi, H.; Filhol, J. S.; Wang, Q.; Pham, T.; Rabah, J.; Maisonhaute, E.; Bonniol, V.; Servat, K.; Tingry, S.; Cornu, D.; Kokoh, K. B.; Napporn, T. W.; Minteer, S. D. Deciphering the Electrocatalytic Reactivity of Glucose Anomers at Bare Gold Electrocatalysts for Biomass-Fueled Electrosynthesis. *ACS Catal.* **2022**, *12*(20), 12563-12571. DOI: https://doi.org/10.1021/acscatal.2c03399

[12] Rosales-Calderon, O.; Arantes, V. A review on commercial-scale high-value products that can be produced alongside cellulosic ethanol. *Biotechnol. Biofuels*, **2019**, *12*(1), 1-58. DOI: https://doi.org/10.1186/s13068-019-1529-1

[13] Yaqoob, L.; Noor, T.; Iqbal, N. A comprehensive and critical review of the recent progress in electrocatalysts for the ethanol oxidation reaction. *Rsc Adv.* **2021**, *11*(27), 16768-16804. DOI: https://doi.org/10.1039/D1RA01841H

[14] Ivandini, T. A.; Rao, T. N.; Fujishima, A.; Einaga, Y. Electrochemical oxidation of oxalic acid at highly boron-doped diamond electrodes. *Anal. Chem.* **2006**, *78*(10), 3467-3471. DOI: https://doi.org/10.1021/ac052029x

[15] Heard, D. M.; Lennox, A. J. Electrode materials in modern organic electrochemistry. *Angew. Chem., Int. Ed.* **2020**, *59*(43), 18866-18884. DOI: https://doi.org/10.1002/anie.202005745

[16] Badalyan, A.; Stahl, S. S. Cooperative electrocatalytic alcohol oxidation with electron-proton-transfer mediators. *Nature* **2016**, *535*(7612), 406-410. DOI: https://doi.org/10.1038/nature18008

[17] Ciriminna, R.; Palmisano, G.; Pagliaro, M. Electrodes Functionalized with the 2,2,6,6-Tetramethylpiperidinyloxy Radical for the Waste-Free Oxidation of Alcohols. *ChemCatChem* **2015**, *7*(4), 552-558. DOI: https://doi.org/10.1002/cctc.201402896

[18] Breuhaus-Alvarez, A. G.; Li, S.; Hardin, N. Z.; Bartlett, B. M. Oxidizing Ethanol and 2-Propanol by Hypochlorous Acid Generated from Chloride Ions on H_xWO_3 Photoelectrodes. *J. Phys. Chem. C*, **2021**, *125*(48), 26307-26312. DOI: https://doi.org/10.1021/acs.jpcc.1c06286

[19] DiMeglio, J. L.; Breuhaus-Alvarez, A. G.; Li, S.; Bartlett, B. M. Nitrate-mediated alcohol oxidation on cadmium sulfide photocatalysts. *ACS Catal.* **2019**, *9*(6), 5732-5741. DOI: https://doi.org/10.1021/acscatal.9b01051

[20] DiMeglio, J. L.; Terry, B. D.; Breuhaus-Alvarez, A. G.; Whalen, M. J.; Bartlett, B. M. Base-Assisted Nitrate Mediation as the Mechanism of Electrochemical Benzyl Alcohol Oxidation. *J. Phys. Chem. C* **2021** *125*(15), 8148-8154. DOI: https://doi.org/10.1021/acs.jpcc.0c10476

[21] Li, S.; Bartlett, B. M. Selective Chloride-Mediated Neat Ethanol Oxidation to 1,1-Diethoxyethane via an Electrochemically Generated Ethyl Hypochlorite Intermediate. *J. Am. Chem. Soc.* **2021**, *143*(39), 15907-15911. DOI: https://doi.org/10.1021/jacs.1c05976

[22] Choi, S.; Choi, W. I.; Lee, J. S.; Lee, C. H.; Balamurugan, M.; Schwarz, A. D.; Choi, Z. S.; Randriamahazaka, H.; Nam, K. T. A Reflection on Sustainable Anode Materials for Electrochemical Chloride Oxidation. *Adv. Mater.* **2023**, *35*(43), 2300429. DOI: https://doi.org/10.1002/adma.202300429

[23] Wang, Y.; Liu, Y.; Wiley, D.; Zhao, S.; Tang, Z. Recent advances in electrocatalytic chloride oxidation for chlorine gas production. *J. Mater. Chem. A*, **2021**, *9*(35), 18974-18993. DOI: https://doi.org/10.1039/D1TA02745J

[24] Lucky, C.; Wang, T.; Schreier, M. Electrochemical Ethylene Oxide Synthesis from Ethanol. *ACS Energy Lett.* **2022**, *7*(4), 1316-1321. DOI: https://doi.org/10.1021/acsenergylett.2c00265

[25] Nagarale, R. K.; Bhattacharya, B.; Jadhav, N. A.; Singh, P. K. Synthesis and electrochemical study of a functional ionic polymer. *Macromol. Chem. Phys.* **2011**, *212*(16), 1751-1757. DOI: https://doi.org/10.1002/macp.201100145

[26] El-Shafei, A. A. Electrocatalytic oxidation of methanol at a nickel hydroxide/glassy carbon modified electrode in alkaline medium. *J. Electroanal. Chem.* **1999**, *471*(2), 89-95. DOI: https://doi.org/10.1016/S0022-0728(99)00235-1

[27] Tomcsanyi, L.; De Battisti, A. Identification of the adsorbed intermediate of the electrooxidation of chloride by the cv technique. *Electrochim. Acta* **1996**, *41*(18), 2917-2919. DOI: https://doi.org/10.1016/0013-4686(96)00109-0

[28] Tomcsányi, L.; De Battisti, A.; Hirschberg, G.; Varga, K.; Liszi, J. The study of the electrooxidation of chloride at RuO_2/TiO_2 electrode using CV and radiotracer techniques and evaluating by electrochemical kinetic simulation methods. *Electrochim. Acta* **1999,** *44*(14), 2463-2472. DOI: https://doi.org/10.1016/S0013-4686(98)00381-8

[29] Bard, A. J.; Faulkner, L. R.; White, H. S. Electrochemical methods: fundamentals and applications. John Wiley & Sons. 2022

[30] Lusis, M. A.; Ratcliff, G. A. Diffusion of inert and Hydrogen-bonding solutes in aliphatic alcohols. AIChE Journal, *AIChE J.* **1971**, *17*(6), 1492-1496. DOI: https://doi.org/10.1002/aic.690170634

[31] Petrov, A. N.; Alper, G. A. VISCOSITY OF NONELECTROLYTE SOLUTIONS BASED ON FORMAMIDE. *Zh. Obshch. Khim.* **1992**, *62*(6), 1231-1235.

[32] Vago, E. R.; Calvo, E. J. Oxygen electro-reduction on iron oxide electrodes: III. Heterogeneous catalytic H_2O_2 decomposition. *J. Electroanal. Chem.* **1995**, *388*(1-2), 161-165. DOI: https://doi.org/10.1016/0022-0728(95)03860-J

[33] Vago, E. R.; Calvo, E. J.; Stratmann, M. Electrocatalysis of oxygen reduction at well-defined iron oxide electrodes. *Electrochim. Acta* **1994**, *39*(11-12), 1655-1659. DOI: https://doi.org/10.1016/0013-4686(94)85150-6

[34] Breuhaus-Alvarez, A. G.; Cheek, Q.; Cooper, J. J.; Maldonado, S.; Bartlett, B. M. Chloride Oxidation as an Alternative to the Oxygen-Evolution Reaction on H_xWO_3 Photoelectrodes. *J. Phys. Chem C.* **2021**, *125*(16), 8543-8550. DOI: https://doi.org/10.1021/acs.jpcc.0c11282

[35] Jung, K.; Lee, D.; Seo, C.; Lee, J.; Lee, S. Y.; Chang, H. N.; Kim, Y. C. Permeation characteristics of volatile fatty acids solution by forward osmosis. *Process Biochem.* **2015**, *50*(4), 669-677. DOI: https://doi.org/10.1016/j.procbio.2015.01.016

Chapter 4

Electrochemically Deposited Manganese Oxide Allows Facile Selective Electrochemical Ethanol Oxidation under Solvent-free Conditions

4.1. Introduction

Selective bio-derivable alcohol oxidation is considered one of the approaches to alleviate the overdependence on fossil fuel-based processing of chemicals. In a well-industrialized process, ethanol is produced at a scale of 10^{15} gallons per year simply in the U.S. Despite being used majorly as fuel or fuel additives, ethanol has the potential to serve as a promising building block chemical, with plenty of potentially profitable chemicals it can be processed to.[1] Oxidation, or dehydrogenation of ethanol is thus heavily sought after, since hydrogen gas may be generated stoichiometrically alongside the oxidation reaction, depending on the approach taken. Upon selective oxidation, alcohols can be converted into aldehydes, carboxylic acids, esters, and polymer precursors.[2] Although, many catalytic ethanol conversions are carried out with gas-phase thermocatalysis. With the developments of photovoltaic devices and photoelectrochemical materials, electrochemistry is a promising alternative approach for carrying out catalytic conversions with renewable energy sources.[3] With (photo)electrocatalysis, stoichiometric redox reagent can be avoided, achieving high atomic economy, as well as controlling both the anodic and cathodic reactions. Compared to traditional thermocatalysis, electrocatalysis can be carried out in ambient conditions where elevated pressure and/or temperature is not required. Finally, fuel-forming reaction, hydrogen evolution reaction can proceed on the counter electrode where reduction reaction occurs, further elevating the potential and financial benefits for electrocatalysis.

Apart from the potential control one can directly apply on the working electrodes, another frequently used approach for mechanistic control is redox mediators. Mediated electrocatalysis is generally sought after due to the faster kinetics that the mediator redox couple provide, and the benefits of avoiding direct organic oxidation on the electrode

surface that may result in poor selectivity or electrode passivation.[4] While the state-of-the-art mediators are still *N*-oxyl radical and their derivatives, recent studies have shown that inexpensive, simple inorganic anions from accessible salt sources can also work effectively in the mediated oxidation of alcohols. Apart from previous chapters' discussion on solvent-free chloride mediated mechanism, other recent works have been carried out regarding mediated electrocatalysis. With nitrate anion, a hydrogen atom extraction mechanism is observed for the reaction between benzyl alcohol and electrochemically generated nitrate radicals on platinum electrode in acetonitrile.[5] Additionally, it is found that chloride anions can be oxidized to hypochlorous acid photoelectrochemically, thus oxidizing ethanol or 2-propanol towards acetaldehyde, acetic acid, or acetone respectively.[6]

Despite the obvious benefits of using a redox mediator, limitations exist especially when larger-scale processing is of interest. The *N*-oxyl radicals, despite providing fast kinetics and excellent selectivity, are reactive organic compounds that have severe environmental impacts as well as high storage and transportation costs. Chloride anion mentioned above shows promise, yet EtOCl is a reactive chemical and could explode in large concentration, resulting in safety concerns especially in large-scale processing with higher working currents. Nevertheless, inspired by the solvent-free scheme mentioned in earlier chapters, we realize it is important to develop this scheme by seeking noble metal free electrocatalysts that can hasten the kinetics of direct EOR without the need for redox mediators, so that larger-scale reactions can be carried out with more financial benefits. Finally, the lack of a solution-phase redox active species allows the use of membrane-free 1-compartment electrolysis, further lowering the cost and complexity of the device especially for non-aqueous solutions. Previous studies have shown that platinum group metals, especially Pt, Pd, have feasible capabilities in performing alcohol oxidation reactions due to their strong adsorption features for reaction intermediates.[7,8] However, their abundancy is scarce compared to early transition metals.[9]

Manganese oxide is known to have applications in performing thermochemical oxidation of ethanol.[10,11] The formation and alignment of MnO_6 octahedra enables multiple lattice structures that brings benefits to the adsorption of ethanol.[12] Additionally, MnO_2 is known to provide synergy effect when loaded with noble metal. In the pathway of EtOH total oxidation to CO_2, MnO_2 serves as a dehydrogenation agent to form C=O intermediate

on adjacent Pt.[13] These results show MnO$_x$ may serve as a potential noble metal free electrocatalyst.

4.2. Experiments

4.2.1. Chemicals and Materials

Tetrabutylammonium trifluoromethanesulfonate (>98.0%, Fisher), tetrabutylammonium nitrate (98%, Fisher), tetrabutylammonium chloride (≥97.0%, Sigma, recrystallized), manganese bis(trifluoromethanesulfonate) (98%, Ambeed), Trifluoromethanesulfonic acid (98+%, Thermo Scientific Chemicals), ethanol (200 proof, Fisher), acetone (certified ACS, Fisher), hydrochloric acid (certified ACS Plus, Fisher), nitric acid (65% w/w/certified, Fisher), hydrogen peroxide solution (30% w/w, Sigma), toluene (HPLC, >99.8%, Fisher), 1,1-diethoxyethane (99%, Fisher), manganese sulfate monohydrate (99%, Fisher) were purchased and used as described. Ferrocene (98%, Sigma) is purified by sublimation at 120 degrees Celsius on a hot plate. FTO glass (1.8mm TECTM 15 Low Iron, Pilkington) is cut into 4 × 2.54 cm^2 slides before electrode preparation.

4.2.2. Electrode Preparation and Characterization

Up to 10 FTO glass slides of the abovementioned size are placed in a custom Teflon rack, where the majority of the FTO surface is exposed. Such rack alongside the FTO glasses is then placed in a 250 mL beaker where enough solvent is added to submerge all glasses. This beaker is then allowed to sonicate for 15 minutes under room temperature. A sequence of solvents is used in the following order: acetone, soap water, ethanol. Note that after the soap water sonication, a complete ultrapure water (18.2 MΩ / cm^2) rinse is necessary. After the final ethanol wash, the glasses are allowed to sit in ethanol until electrodeposition. Prior to deposition, the film is completely dried with compressed air. A custom copper wire – glass tube electrode is attached to the FTO film with conductive copper tape (3M) and such electrochemical contact is sealed by scotch tape to avoid wetting the copper component. The tape also limits the surface area of FTO exposed to solution to be exactly 2.54 × 2.54 cm^2.

Electrodeposition is carried out in an ultrapure water solution with 20 mM MnSO$_4$ and 50 mM HCl dissolved. In a typical deposition procedure, 200 mL of this precursor is made

in a volumetric flask and is poured into a 50 mL beaker submerging the FTO-electrode. The FTO-electrode is anchored vertically by a clamp. On a CHI 1000C potentiostat, electrochemical deposition proceeds with a 3-electrode system with a custom saturated Ag/AgCl reference electrode (Ag wire is from CH Instruments; the glass part is exchanged with a same-sized glass tube with a porous glass frit (955-00003, Gamry) attached to its end and is sealed by a heat-shrinking plastic sleeve) and a graphite counter electrode (935-00014, Gamry). Note that Pt counter electrode is to be avoided due to Mn platting during experiments. A constant potential coulometry (CPC) experiment is carried out at 1.1 V vs. reference, where 0.904 C of charge is allowed to pass. The solution is kept under quiescent condition. After opening the circuit, the film is removed from the beaker and thoroughly rinsed with DI water, then dried with compressed air. Such film should have a brown color. The electrodeposition solution is replaced after every 2 depositions. On a planar slate, up to 6 films are annealed together in a Muffle furnace at 400 degrees Celsius for 2 hours, with a ramp rate of 10 degrees per minute. The film should look darker with a near-black color after annealing and is stored in petri dishes when not used to avoid dust.

X-ray diffraction (XRD) is carried out in a Panalytical Empyrean diffractometer with a power of 1.8 kW (40 mA, 45 kV) using a Cu Kα radiation source (λ = 0.15418 nm). A position-sensitive 1D diffractometer (X'Celerator Scientific) equipped with a Bragg-Brentano[HD] X-ray optic was used to ensure delivery of only Kα radiation. All scan procedures are carried out with a step size of 0.0334 degree.

Scanning electron microscopy (SEM) and energy-dispersive X-ray spectroscopy (EDX) is carried out on a JEOL JSM-7800FLV Scanning Electron Microscope and an Oxford XMaxN 80mm² silicon-drift energy-dispersive X-ray spectrometer, respectively. Both instruments are in the Robert B. Mitchell Electron Microbeam Analysis Lab (EMAL), located in Ann Arbor, MI. For both the top-down and cross-section images, a 10 keV acceleration potential is used.

X-ray photoelectron spectroscopy (XPS) is carried out with a Kratos Axis Ultra X-ray photoelectron spectrometer in Michigan Center for Materials Characterization (MC[2]), located in Ann Arbor, MI. For all the measurements, a monochromatic Al Kα X-ray is used. 30 core scans are done for Mn 3s, while 10 core scans are done for C 1s. The charging

effects on the substrate are mitigated by an electron gun neutralizer. Binding energy of the adventitious carbon is adjusted to 284.8 eV as a calibration to peak positions.

4.2.3. Solution Phase Analysis

Inductively coupled plasma mass spectrometry (ICP-MS) is carried out on a Perkin-Elmer Nexion 2000 ICP-MS with Sc as internal standard for the quantification of solution-phase Mn. Several procedures have been carried out for the ICP-MS measurements in this work. For the full digestion of MnO_x film, the film is soaked in 20 mL of concentrated nitric acid. Then, 1000 μL of H_2O_2 is added dropwise with a pipet. Complete digestion proceeds after roughly 1 hour. For the control reaction, a cleaned FTO is treated the same way. Such solutions are diluted 1:1000 with 5 % HNO_3 to make the ICP-MS sample. For the post-electrolysis dissolution assessment, aliquot is taken directly from the post-electrolysis cell before diluted 1:1000 with 5 % HNO_3 to obtain the sample. Control experiment of this measurement is prepared with diluting the electrolyte solution with no charge passed. Finally, soaking experiments are done by soaking MnO_x films in 20 mL 200 mM HOTf ethanol solution in a 50 mL falcon tube, with vigorous stirring for 24 hours. The aliquot is subsequently diluted 1:1000 with 5 % HNO_3 and a same control is used. All ICP-MS data is collected in triplicates.

Gas chromatography (GC) measurement is carried out on a Thermo Fisher Trace 13-10 gas chromatograph. A capillary column and flame ionization detector (FID) heated at 325 degrees Celsius is used. For sample preparation, a stock solution is made with toluene (internal standard) dissolved in ethanol. The concentration of toluene is calculated to ensure a 2 mM concentration of toluene exists in the sample. The sample is prepared by performing a 10-fold dilution of post-electrolysis aliquot with the abovementioned stock solution to make a 1 mL sample. The GC oven is set to 35 degrees Celsius, held for 1 minute, before ramping up to 200 degrees at a 10 degrees/min ramp rate. Finally for quantification, a calibration curve is made for 0 – 100 mM 1,1-diethoxyethane solutions in ethanol, where they are treated the same way as post-electrolysis aliquots when being prepared as samples. The calibration curve is obtained from ratios of integrated peak area of toluene and 1,1-diethoxyethane. All GC measurements, including the calibration curve, are measured in triplicates.

4.2.4. Electrochemical Measurements

All electrochemical experiments, apart from the Tafel analyses, are carried out on a CHI1000C potentiostat (CH Instruments). The Tafel analyses are done on a CHI760E potentiostat (CH Instruments). All electrochemical data is plotted and treated under the IUPAC convention. All electrochemical experiments are carried out with a 3-electrode system. The aqueous 3-electrode system is described in 4.2.2., and in an organic-solvent, different reference and counter electrodes are used. The Ag reference electrode (Ag wire is from CH Instruments; the glass part is exchanged with a same-sized glass tube with a porous glass frit (955-00003, Gamry) attached to its end and is sealed by a heat-shrinking plastic sleeve) is filled with the electrolyte solution, and a custom Pt wire (Surepure Chemetals, 0.05 cm diameter, with 2 cm submerged, resulting with ~0.314 cm^2 surface area) is mounted to a piece of copper wire sealed in a glass tube and is used as the counter electrode. Note that the Ag wire serves as the pseudoreference electrode; the potential is calibrated to the ferrocenium/ferrocene redox couple ($Fc^{+/0}$). To calibrate the pseudo reference electrode to ferrocene redox couple, the exact solution of interest is replicated but with an additional 10 mM ferrocene dissolved. Then with the same set of reference/counter electrodes yet with a glassy carbon working electrode (CH Instrument), a CV with a scan rate of 50 mV / s is carried out between 0 – 1 V to obtain the calibration value by calculating the average of both the oxidation and reduction peak potential. Apart from Tafel analyses and film deposition, all electrochemical measurements are carried out in a custom 2-compartment compression cell with 10 mL electrolyte in each compartment. The compartments are separated by a glass frit.

Tafel analyses is carried out within a 50 mL beaker with the film clamped so that it suspends in solution, yet completely submerged, with a fixed position. Vigorous stirring is applied with a stir bar (1.5 cm length, Fisher) so that convection is provided but the solution body isn't swiveling. Other LSVs and CPCs are carried out in a custom-made compression cell where a fine glass frit is installed between the compartments. The o-ring and clamp ensures a 3.14 cm^2 surface area is exposed to the solution. Vigorous stirring is applied with a stir bar (3.0 mm length, Fisher) to avoid collision with the film surface.

4.3. Results

4.3.1. Characterization of Deposited MnO$_x$ Electrocatalyst

With an electrochemical deposition method, manganese (II) sulfate is oxidized to form MnO$_x$ on FTO substrates, with a mixed oxidation state between +3 and +4. For this deposition, a tentative chemical reaction can be described below:

$$Mn^{2+} - (2x-2)\ e^- + x\ H_2O \rightarrow MnO_x + 2x\ H^+ \qquad (4.1)$$
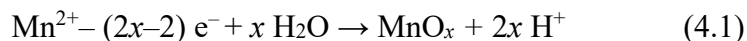
where a controlled amount of charge is passed, 140 mC/cm^2 of FTO substrate exposed to the solution. The detailed procedure can be found in section 4.2 of this thesis, and an example of such CPC deposition *j-t* curve is shown in **Figure C.1**. With the as-deposited film, X-ray diffraction is carried out prior to and after annealing. **Figure 4.1** shows the diffraction spectra for both annealed and unannealed film, where barely any diffraction peaks can be observed apart from the inherited ones from the fluorine-doped tin oxide (FTO) underlying film (marked as vertical straight lines). Even for trials with 3 times more charge passed during the deposition and annealing, the same diffraction pattern is observed.
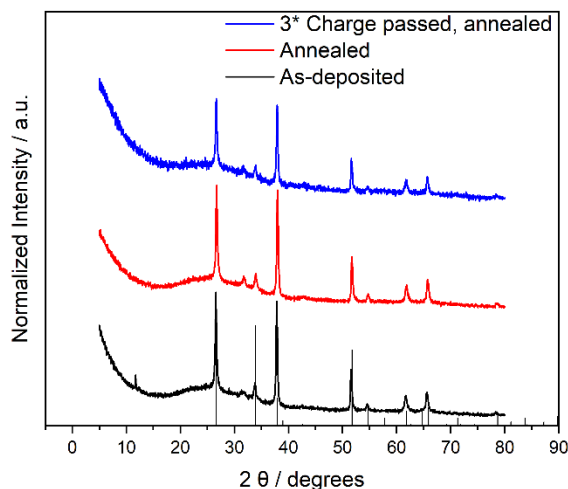

Figure 4.1. X-ray diffraction patterns of deposited MnO$_x$ films on FTO substrate. Vertical black lines represent diffraction peaks from the conductive FTO layer.

Thus, we conclude that our deposited films are largely amorphous. It is noteworthy that for the unannealed material, a reflection at ~12º 2θ can be observed, agreeing with what is reported for the *d*-spacing between layered Birnessite structures of MnO$_x$ prepared with a similar method. Upon annealing, such features vanish due to the removal of interlayer water.[14] Subsequently, SEM imaging alongside EDX is carried out to assess the morphology and thickness of prepared films. **Figure 4.2** shows the top-down and cross-

sectional SEM images, as well as cross-sectional EDX elemental mapping. The top-down image for an as-deposited, not annealed MnO_x film can be found in **Figure C.2**.

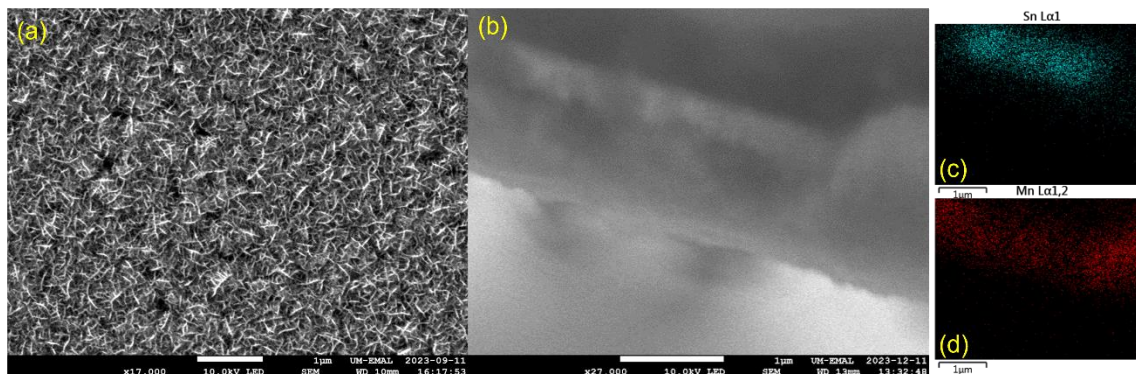

Figure 4.2. SEM images for annealed MnO_x films. (a) top-down; (b) cross-section; (c) & (d) elemental mapping of (b) for Sn and Mn, respectively.

From the top-down image, a decent coverage of MnO_x is observed with decent surface roughness. From the cross-sectional image, corroborated with the mapping of Sn and Mn metals, we can conclude that the MnO_x films have an even thickness of ~1.2 microns.

4.3.2. Electrochemical Tests for Ethanol Oxidation Reaction (EOR) on MnO_x

With the prepared material, we carry out the electrochemical EOR reaction on a custom-made compression cell. To avoid any sort of mediated reaction, like reported in other chapters, Bu_4NOTf is selected to be the electrolyte due to its anion's stability towards redox reactions. **Figure 4.3** shows the LSV curves of FTO, annealed MnO_x and as-deposited MnO_x in a 200 mM Bu_4NOTf ethanol solution.
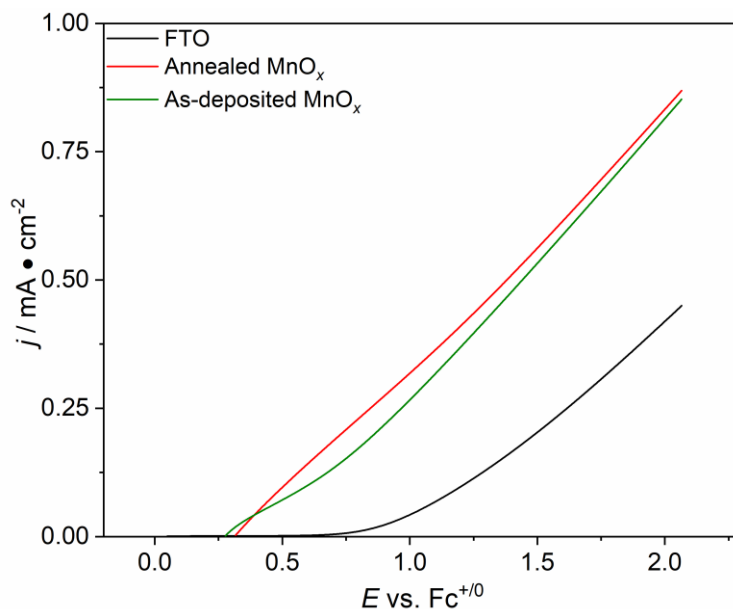
Figure 4.3. LSV curves for different films in 200 mM Bu$_4$NOTf ethanol solution, in a compression cell. The scan rate is 100 mV/s.

Clearly, a lower onset potential and higher anodic current can be observed with the electrocatalyst layer, and the annealed film exhibited both traits compared to the unannealed film as well. Thus, we chose the annealed material as our focus in this chapter. Intrigued by the elevated rate of EOR on this material, we moved on to test if it is also active to the easier-to-oxidize anions by performing the same LSV measurements with Bu$_4$NCl and Bu$_4$NNO$_3$, both with the same concentration as in **Figure 4.4**. Previous chapters have mentioned that chloride and nitrate anions both have potential to be utilized as redox mediators, thus they are easily oxidizable. Should these anions get oxidized, an earlier onset potential would be expected compared to when Bu$_4$NOTf is the electrolyte.
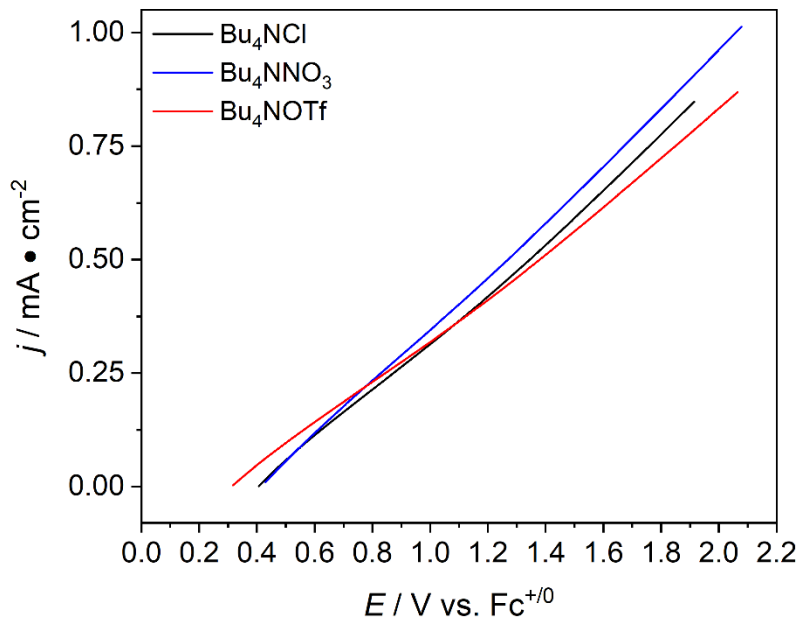
Figure 4.4. LSV curves of different electrolytes in ethanol on MnO$_x$. The electrolyte concentration is 200 mM and the scan rate is 100 mV / s. Such measurements are carried out in a compression cell with a quiescent solution.

Rather surprisingly, not much difference is observed among the 3 electrolytes tested. Despite the ethanol-specific chloride oxidation mechanism discussed in the previous chapters, neither lower onset potential nor higher current is observed in this case for chloride oxidation. Similarly, despite recent reports on nitrate anions functioning as redox mediators in alcohol oxidation reactions, insignificant difference is observed in the LSV measurements. This result further supports the hypothesis that MnO$_x$ can significantly improve the EOR kinetics, so that EOR is no longer outcompeted by the oxidation of easy-to-oxidize anions. With the above observations, we carried out constant potential coulometry (CPC) measurements to assess the long-term current output and stability of annealed MnO$_x$ in EOR practices. Understanding that conductivity is an important factor especially in non-aqueous systems, and that the hydrogen evolution reaction (HER) is of great interest, HOTf is also tested out as a strong acid with an inert anion. **Figure 4.5** shows triplicates of 16-hour CPC experiments conducted in the compression cell with vigorous stirring. **Figure C.3** shows LSVs of as-deposited MnO$_x$ and annealed film in this 200 mM HOTf solution, where a similar pattern is observed to **Figure 4.3**.
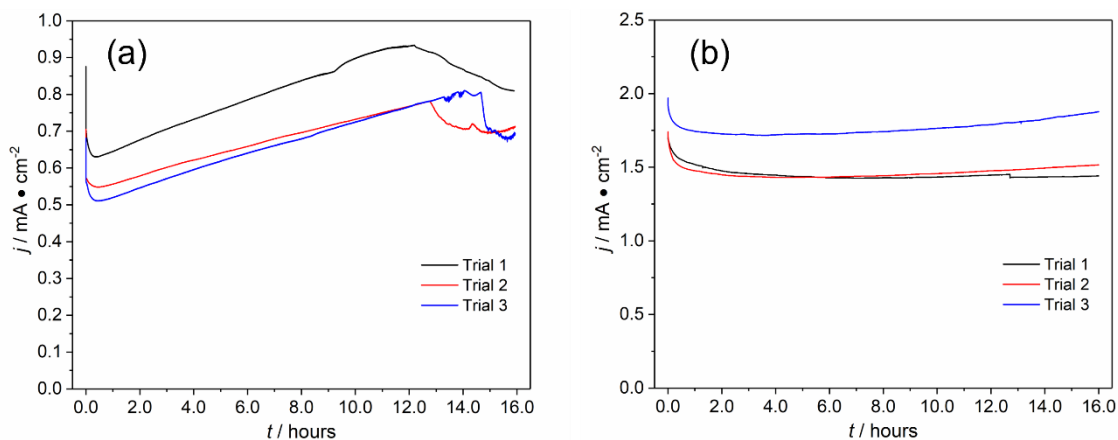
Figure 4.5. CPC curves of 200 mM (a) Bu$_4$NOTf, (b) HOTf dissolved in ethanol on MnO$_x$. Note that the scale on the y-axis is different. Applied potential is 1.76 V vs. Fc$^{+/0}$.

For Bu$_4$NOTf, an unusual CPC curve is observed with an initial drop followed by a gradual increase in current over time. For HOTf, a rather stable current is observed following the initial drop. As is expected, roughly 3-fold higher current is observed for the HOTf case, which has a conductivity of 7.80 mS/cm^2 compared to 2.74 mS/cm^2 for the Bu$_4$NOTf. Control CPC experiment with FTO in HOTf is shown in **Figure C.4**, where a degrading, low-current density j-t curve is observed. We hypothesize that the direct EOR on MnO$_x$ results in the following reaction regardless of electrolyte:

$$CH_3CH_2OH - 2e^- \rightarrow CH_3CHO + 2H^+ \qquad (4.2)$$

Where, same as described in Chapter 2, the acetaldehyde formed is expected to form 1,1-diethoxyethane (DEE) upon acetalization reaction with the ethanol solvent. From this viewpoint, we attribute the gradual increase in current with the Bu$_4$NOTf case to the build-up of proton concentration. To understand the selectivity of the CPC experiments, we carried out GC analyses for the post-CPC solutions to quantify the amount of DEE made. The Faradaic efficiency (FE) is calculated with the same solution used in Chapter 2. The FE is measured, with triplicates, to be 98.0±0.1% for the Bu$_4$NOTf and 91.3±3.9% for the HOTf cases respectively. This demonstrates the selectivity of MnO$_x$ on direct EOR in both solutions. GC chromatogram of post-CPC aliquot and the control is shown in **Figure C.5**. While the HOTf electrolyte provides higher current and conductivity, the strong acidity raises concerns on corrosion. Despite the stable current, to ensure that MnO$_x$ is not corroded and dissolved, ICP-MS experiments have been carried out to assess the solution Mn cation concentration after >24-hour CPCs. With a digestion experiment aiming to dissolve off all

the MnO$_x$, 4.94×10^{-6} moles total loading of Mn is found to be on the FTO substrate following a normal deposition. Less than 1 % Mn is observed for the 24-hour CPC, confirming the excellent stability of the MnO$_x$ material even under strong acidic conditions.

Moreover, Tafel analysis is carried out to assess the kinetic details of MnO$_x$ based EOR. **Figure 4.6** shows such results for MnO$_x$ in Bu$_4$NOTf, HOTf and FTO in Bu$_4$NOTf as a control reaction.
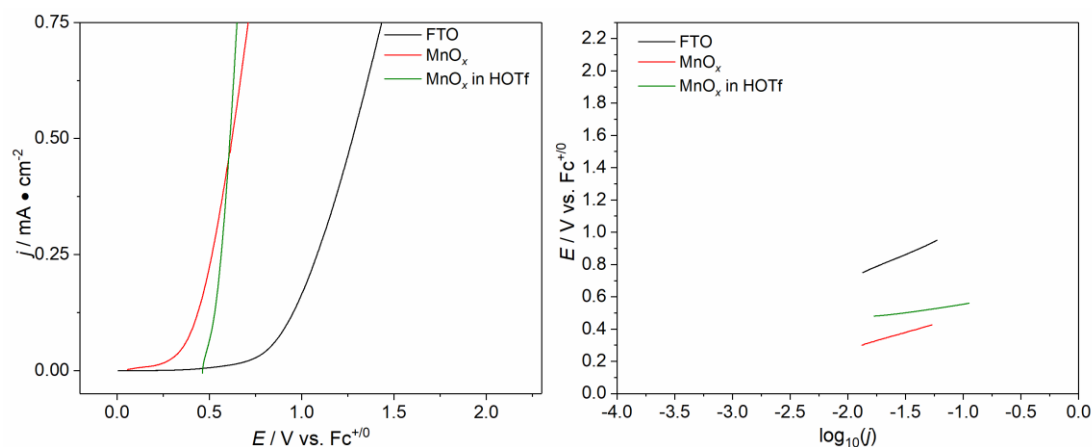

Figure 4.6. Tafel analysis with the MnO$_x$ electrocatalyst and FTO as a control. Left: LSV curves at 1 mV/s with vigorous stirring and 200 mM Bu$_4$NOTf, or HOTf if specified. Right: Tafel slopes obtained from the LSV curves.

The following Tafel slopes are collected: FTO & Bu$_4$NOTf, 304 mV/dec; MnO$_x$ & Bu$_4$NOTf, 204 mV/dec; MnO$_x$ & HOTf, 100 mV/dec. This result agrees with the previous observations that MnO$_x$ improves the kinetics of EOR compared to FTO, as well as hinting that the presence of acid also accelerates the reaction.

4.4. Discussion

4.4.1. Operational Stability of MnO$_x$ Electrocatalyst

Despite the observed stability during CPC from both a stable *j-t* curve and low Mn dissolution by ICP-MS, it is noticed that the color of the dark-brown film would fade following soaking in the post-CPC solution overnight. This indicates a chemical dissolution/corrosion reaction. A soaking experiment is thus carried out to assess such dissolution process. In triplicates, MnO$_x$ is soaked in 200 mM HOTf, with vigorous stirring for overnight. Similarly, the color of the film is gone post the soaking experiment. ICP-MS is carried out on the supernatant, and based on the total Mn loading measured earlier, only 59.6 ± 0.59 % of Mn dissolved, indicating a good amount of Mn left on the surface. We

carried out XPS to determine the oxidation state of the remaining Mn after soaking that are washed and dried thoroughly, as well as films for those deposited or annealed for reference. The average oxidation state (AOS) of Mn on the surface is calculated with the following reaction:[15]

$$AOS = 9.67 - 1.27 \times \Delta E_{(Mn\ 3s)} / eV \qquad (4.3)$$

where ΔE corresponds to the absolute value of the difference in binding energies of the 2 Mn 3s fitted peaks. **Figure 4.7** shows the fitted XPS results for as-deposited film, annealed film, and post-soaking film.
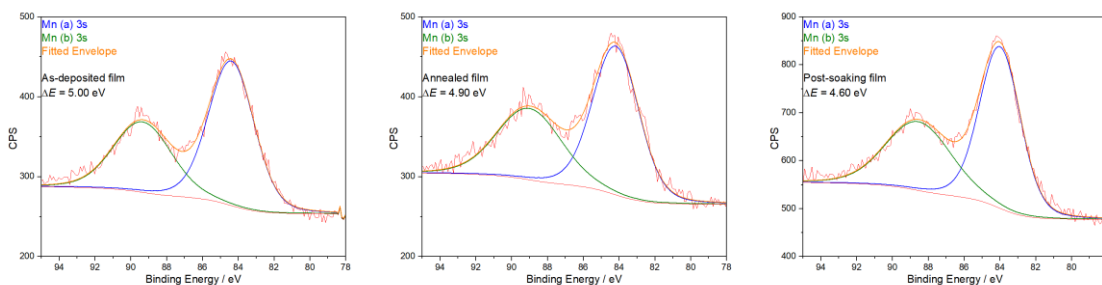

Figure 4.7. Mn 3s XPS spectra of as-deposited film, annealed film, and post-soaking film.

With equation (4.3), the AOS of Mn can be obtained for the abovementioned film: 3.320 for as-deposited film, 3.447 for annealed film, and 3.828 for post-soaking film. It is intuitive that annealing increases the oxidation state of the electrochemically deposited film. However, the significant increase in AOS after the corrosive soaking process is unexpected. One possible explanation is that disproportionation reaction of Mn (III) proceeds to yield Mn (IV) and Mn (II), with the latter usually being soluble. Relating this hypothesis to earlier observed operational stability, a straightforward theory would be that during CPC, re-deposition of solvated Mn (II) proceeds under applied potential, keeping the film intact. To test this, we took one of the soaked films and used it as the working electrode, carried out CPC experiment with 195 mM Bu$_4$NOTf and 2.5 mM Mn(OTf)$_2$ to mimic the case where solvated Mn (II) exist. **Figure 4.8** shows the LSV under such circumstance alongside a normal LSV carried out with annealed MnO$_x$ in a Mn-free electrolyte. Significantly lower current is observed with the solvated-Mn case, likely indicating that the re-deposition is not happening even with applied potential; and that the Mn (IV)-dominant material is not as active as the annealed MnO$_x$ towards direct EOR. Thus, we hypothesize that other mechanisms are contributing to the improved kinetics of MnO$_x$ based EOR.
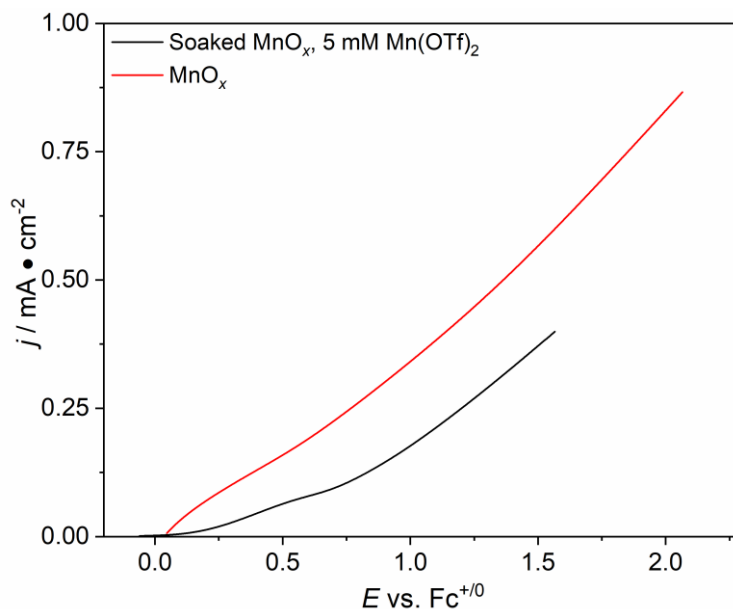
Figure 4.8. LSV curves of (red) soaked MnO_x in 5 mM $Mn(OTf)_2$, 195 mM Bu₄NOTf and (black) annealed MnO_x in 200 mM Bu₄NOTf. The scan rate is 100 mV/s.

Nevertheless, we propose a similar disproportionation reaction reported on MnO_x material during acidic oxygen evolution reaction.[16] **Figure 4.9** shows a tentative scheme for such reaction that results in the formation of Mn (IV) and Mn (II):

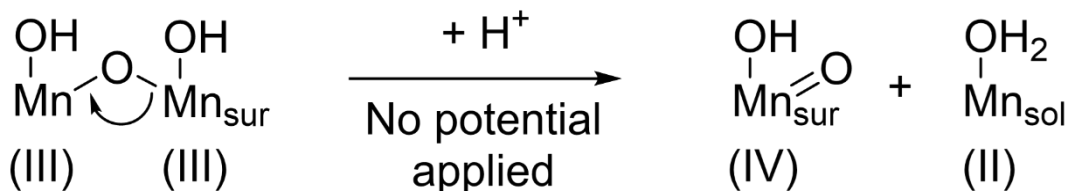Figure 4.9. Proposed mechanism for the disproportionation reaction of Mn (III) species when soaked in ethanol solution.

4.4.2. Purposed Ethanol Oxidation Reaction on MnO_x

Referring back to the Tafel analysis in **Figure 4.6**, one can notice that despite the obvious lower Tafel slope in the HOTf case, a much higher onset potential is found compared to Bu₄NOTf cases. This indicates that it requires a less negative potential to reduce the film, that the film is easier to be reduced when acid is present. Moreover, in the previously mentioned soaking experiment, control reaction carried out with aqueous system showed a much slower rate of film dissolution, even with 200 mM H_2SO_4 added (greater than 3 days of soaking). When 200 mM ethanol is sparged in the H_2SO_4 aqueous solution, a similar rate is observed to that of 200 mM HOTf in ethanol. This hints the

likelihood of a chemical oxidation mechanism of ethanol, especially when there is acid around. Realizing the drastic thermodynamic instability of solvated Mn (III) species,[17] and the low observed activity for Mn (IV) species, we hypothesize the following chemical EOR mechanism shown in **Figure 4.10**:
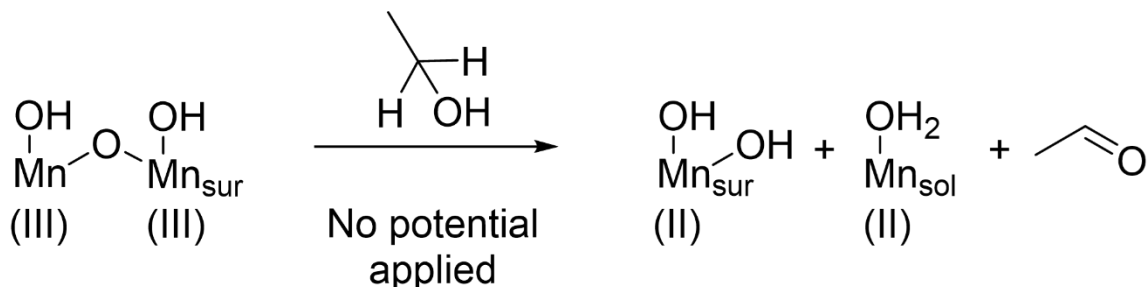

Figure 4.10: Proposed reaction for the chemical oxidation reaction carried out by Mn (III) species when soaked in ethanol solution. Note that the stoichiometry between the Mn species on the right side of the equation is unclear.

Such mechanism is relatable to the previously reported MnO_x-driven oxygen evolution reaction mechanism.[16] And thus, based on this mechanism, we hypothesize that the operational stability observed during the CPC experiments arise from the potential-driven deprotonation of Mn-OH or Mn-OH2 species. As proton gets removed, the Mn center would also be oxidized, maintaining a >3 oxidation state so that the solvation of Mn is avoided. We then carried out Tafel analyses with varied concentrations of HOTf to explore the relationship between reaction kinetics and concentration of HOTf, shown in **Figure 4.11**. Realizing the conductivity can be a factor in current data collected, we added extra amounts of Bu4NOTf to compensate for the conductivity differences among solutions tested.

From the result in **Figure 4.11**, it can be concluded that the presence of acid significantly decreases the Tafel slope, and that increased concentration of acid also mildly decreases the Tafel slope. This observation indicates that the deprotonation step is likely not rate-limiting, otherwise a negative relationship between acid concentration and electrochemical reaction rate would be expected. Thus, we hypothesis that the rate-limiting step is the chemical oxidation of ethanol with Mn (III), and that the applied bias assists in significantly improving the turnover frequency by ensuring the surface is populated with active Mn (III) species. Moreover, the Tafel analysis of FTO in HOTf is also included in the Appendix in **Figure C.6**. In this case, despite being put into a strong acidic condition, the Tafel slope of

FTO didn't decrease (333.9 mV/dec), indicating that the relationship shown in **Figure 4.11** is material-specific and only applies to MnO$_x$.
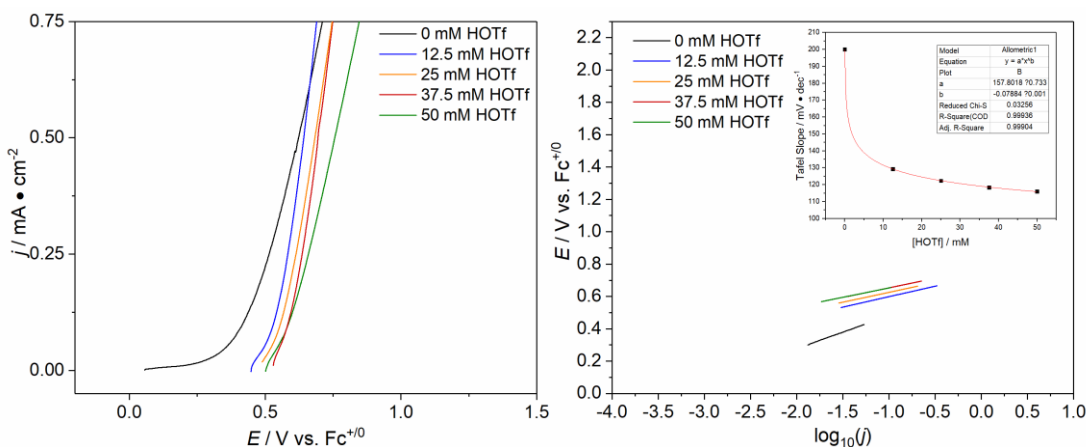

Figure 4.11. Tafel analysis for 0-50 mM HOTf on annealed MnO$_x$ in neat ethanol. (Left) 1 mV/s LSV scans with vigorous stirring in a beaker. (Right) Tafel slope plots with the slope-[HOTf] relationship in the inset. The 0 mM HOTf electrolyte has 200 mM Bu$_4$NOTf added.

4.5. Conclusions and Future Work

Amorphous planar MnO$_x$ is prepared from an electrochemical deposition method on FTO substrate, followed by annealing under atmosphere. This material, when used as an electrocatalyst, can significantly hasten the kinetics of direct electrochemical neat ethanol oxidation reaction. This is confirmed by the near-same LSV curves collected from both inert electrolyte and redox-active anion (Cl$^-$ or NO$_3^-$) based electrolyte. CPC electrolysis is carried out with MnO$_x$ in Bu$_4$NOTf and HOTf electrolyte, where long-term stability and >90% faradaic efficiency for 1,1-diethoxyethane formation is observed in both cases. Higher current as well as lower Tafel slope is observed for the HOTf case. ICP-MS quantified less than 1% Mn dissolution after 24 hours of CPC in HOTf electrolyte, confirming the stability of the MnO$_x$ electrocatalyst. However, when anodic potential is not poised, MnO$_x$ is observed to corrode with Mn collected in solution, while XPS detected elevated amount of Mn (IV) on the surface. Thus, we propose 2 chemical processes that could proceed on the MnO$_x$ material in neat ethanol. First, a spontaneous disproportionation reaction converts surface Mn (III) to Mn (II) and Mn (IV), with the latter species being inert. Additionally, Mn (III) can chemically oxidize ethanol, protonating the Mn-O or Mn-OH bonds and reducing to Mn (II). We hypothesis that the electrochemical ethanol oxidation reaction proceeds through the chemical oxidation process, while the

applied anodic potential deprotonates the Mn-OH or Mn-OH$_2$ bond to maintain the oxidation state and avoid passivation. This work demonstrates the potential of utilizing noble metal free MnO$_x$ as a selective electrocatalyst for neat ethanol oxidation to 1,1-diethoxyethane.

Future works include carrying out *in situ* Raman or IR experiments to track the reaction intermediate to provide direct evidence of this mechanism. We hypothesize that through *in situ* Raman, the potential-introduced transition of Mn species can be tracked, and visible difference is expected in neat-ethanol and ethanol-free conditions. With IR measurement, the ethanol oxidation intermediate can also be observed, thus confirming the step where the carbonyl of MeCHO is formed. Moreover, instead of planar electrode, modifying the electrodeposition method to deposit the material onto high-surface area carbon electrode will assist in elevating the current output of the MnO$_x$ electrocatalyst, while benefiting from this material-based mechanism.

4.6. References

[1] Dagle, R. A.; Winkelman, A. D.; Ramasamy, K. K.; Lebarbier Dagle, V.; Weber, R. S. Ethanol as a renewable building block for fuels and chemicals. *Ind. Eng. Chem. Res.* **2020**, *59*(11), 4843-4853. DOI: https://doi.org/10.1021/acs.iecr.9b05729

[2] Rosales-Calderon, O.; Arantes, V. A review on commercial-scale high-value products that can be produced alongside cellulosic ethanol. *Biotechnol. Biofuels*, **2019**, *12*(1), 1-58. DOI: https://doi.org/10.1186/s13068-019-1529-1

[3] Chatterjee, P.; Ambati, M. S. K.; Chakraborty, A. K.; Chakrabortty, S.; Biring, S.; Ramakrishna, S.; Wong, T. K. S.; Kumar, A.; Lawaniya, R.; Dalapati, G. K. Photovoltaic/photo-electrocatalysis integration for green hydrogen: A review. *Energy Convers. Manage.* **2022**, *261*, 115648. DOI: https://doi.org/10.1016/j.enconman.2022.115648

[4] Zhang, F.; Wang, Q. Redox-mediated electrocatalytic and photocatalytic hydrogen production. *Curr. Opin. Electrochem.* **2022**, *35*, 101097. DOI: https://doi.org/10.1016/j.coelec.2022.101097

[5] DiMeglio, J. L.; Terry, B. D.; Breuhaus-Alvarez, A. G.; Whalen, M. J.; Bartlett, B. M. Base-Assisted Nitrate Mediation as the Mechanism of Electrochemical Benzyl Alcohol Oxidation. *J. Phys. Chem. C* **2021** *125*(15), 8148-8154. DOI: https://doi.org/10.1021/acs.jpcc.0c10476

[6] Breuhaus-Alvarez, A. G.; Li, S.; Hardin, N. Z.; Bartlett, B. M. Oxidizing Ethanol and 2-Propanol by Hypochlorous Acid Generated from Chloride Ions on H_xWO_3 Photoelectrodes. *J. Phys. Chem. C* **2021**, *125*(48), 26307-26312. DOI: https://doi.org/10.1021/acs.jpcc.1c06286

[7] Lamy, C. Electrocatalytic oxidation of organic compounds on noble metals in aqueous solution. *Electrochim. Acta* **1984**, *29*(11), 1581-1588. DOI: https://doi.org/10.1016/0013-4686(84)85012-4

[8] Guo, F.; Li, Y.; Fan, B.; Liu, Y.; Lu, L.; Lei, Y. Carbon-and binder-free core-shell nanowire arrays for efficient ethanol electro-oxidation in alkaline medium. *ACS Appl. Mater. Interfaces* **2019**, *10*(5), 4705-4714. DOI: https://doi.org/10.1021/acsami.7b16615

[9] Rana, S.; Biswas, J. P.; Paul, S.; Paik, A.; Maiti, D. Organic synthesis with the most abundant transition metal-iron: from rust to multitasking catalysts. *Chem. Soc. Rev.* **2021**, *50*(1), 243-472. DOI: https://doi.org/10.1039/D0CS00688B

[10] Santos, V. P.; Pereira, M. F. R.; Órfão, J. J. M.; Figueiredo, J. L. The role of lattice oxygen on the activity of manganese oxides towards the oxidation of volatile organic compounds. *Appl. Catal., B* **2010**, *99*(1-2), 353-363. DOI: https://doi.org/10.1016/j.apcatb.2010.07.007

[11] Bai, B.; Li, J.; Hao, J. 1D-MnO_2, 2D-MnO_2 and 3D-MnO_2 for low-temperature oxidation of ethanol. *Appl. Catal., B* **2015**, *164*, 241-250. DOI: https://doi.org/10.1016/j.apcatb.2014.08.044

[12] Li, J.; Wang, R.; Hao, J. Role of lattice oxygen and lewis acid on ethanol oxidation over OMS-2 catalyst. *J. Phys. Chem. C* **2010**, *114*(23), 10544-10550. DOI: https://doi.org/10.1021/jp102779u

[13] Cai, J.; Huang, Y.; Huang, B.; Zheng, S.; Guo, Y. Enhanced activity of Pt nanoparticle catalysts supported on manganese oxide-carbon nanotubes for ethanol oxidation. *Int. J. Hydrogen Energy* **2014**, *39*(2), 798-807. DOI: https://doi.org/10.1021/jp102779u

[14] Abe, H.; Murakami, A.; Tsunekawa, S.; Okada, T.; Wakabayashi, T.; Yoshida, M.; Nakayama, M. Selective catalyst for oxygen evolution in neutral brine electrolysis: An oxygen-deficient manganese oxide film. *ACS Catal.* **2021**, *11*(11), 6390-6397. DOI: https://doi.org/10.1021/acscatal.0c05496

[15] Beyreuther, E.; Grafström, S.; Eng, L. M.; Thiele, C.; Dörr, K. XPS investigation of Mn valence in lanthanum manganite thin films under variation of oxygen content. *Phys. Rev. B* **2006**, *73*(15), 155425. DOI: https://doi.org/10.1103/PhysRevB.73.155425

[16] Huynh, M.; Bediako, D. K.; Nocera, D. G. A functionally stable manganese oxide oxygen evolution catalyst in acid. *J. Am. Chem. Soc.* **2014**, *136*(16), 6002-6010. DOI: https://doi.org/10.1021/ja413147e

[17] Kim, B.; Lingappa, U. F.; Magyar, J.; Monteverde, D.; Valentine, J. S.; Cho, J.; Fischer, W. Challenges of measuring soluble Mn (III) species in natural samples. *Molecules* **2022**, *27*(5), 1661. DOI: https://doi.org/10.3390/molecules27051661

Chapter 5
Summary and Outlook

5.1. Summary of Presented Work

Through the chapters of this thesis, multiple approaches have been explored to facilitate selective electrochemical neat ethanol oxidation. Solvent-free electrocatalysis has been an overlooked area of study, and more applications could be implemented in not only catalytic redox conversions but also functionalization reactions for organic compounds. We were able to demonstrate the use of chloride as an accessible mediator in neat ethanol oxidation, provide hydrodynamic and mechanistic study for the chloride oxidation reaction in ethanol, and develop a noble metal free MnO_x electrocatalyst that exhibit stability and selectivity in strong acidic conditions.

In chapter 2, we found that chloride can be utilized as a redox mediator for direct EOR. On a commercial glassy carbon electrode, much lower onset potential is observed for chloride electrolyte compared to inert electrolyte. Constant potential electrolysis yielded 1,1-diethoxyethane (DEE) with high stability and faradaic efficiency, and collection experiment confirms chloride was not consumed during electrolysis. With UV-vis spectroscopy, the intermediate generated from chloride oxidation is confirmed to be EtOCl, an unstable species that is known to decompose into acetaldehyde and HCl. Kinetic study for the EtOCl confirms the first-order degradation mechanism. During electrolysis, an equilibrium of EtOCl concentration is reached and DEE is formed from the acetalization reaction of released acetaldehyde.

In chapter 3, mechanistic study is conducted to the COR in neat ethanol. With CV study in dichloromethane, we observed a Volmer step for COR where one-electron oxidation of chloride produced an adsorbed Cl(0) species. Similar analyses are performed in ethanol, where a one-electron anodic electrochemical step is observed. Koutecky-Levich analysis quantified the kinetic rate constant of COR and direct EOR, with the COR's rate constant being 2-3 magnitudes larger than EOR. Realizing that no chlorinated product is observed

in chapter 2, we move on to confirm that EtOCl is the only COR product with an *in situ* spectroelectrochemical analysis, across the potentials of interest. Furthermore, slow scan rate LSVs with RRDE as well as spectroelectrochemical characterization confirms the presence of an electron transfer event where EtOCl is not observed. This chapter provides an example methodology to assess mechanistic details and kinetics in neat ethanol.

In chapter 4, MnO_x is prepared with an electrochemical deposition method on FTO substrate. This amorphous material can electrocatalytically oxidize neat ethanol to 1,1-diethoxyethane with high selectivity and stability. Moreover, such stability is also observed in strong acidic conditions with elevated anodic current. However, when anodic potential is not applied, the electrocatalyst is observed to corrode into solution. The dissolution is then investigated by XPS and ICP-MS and a disproportionation mechanism is proposed. Corroborating with previously reported OER mechanisms, we hypothesize that the catalytic oxidation of ethanol proceeds through a chemical step, where Mn (III) is the oxidant and gets protonated. Applied anodic potential then deprotonates the Mn-OH or Mn-OH_2 species, re-oxidizing Mn and maintaining the integrity of the catalyst. Tafel analyses determined the relationship between [HOTf] and reaction rate, suggesting that the electrochemical deprotonation step is *not* rate limiting. We then hypothesize the chemical oxidation of ethanol is the limiting step in the mechanism. Future work includes *in situ* measurements to provide direct observation of reaction intermediates.

5.2. Introducing Other Components to Neat Alcohol Oxidation Scheme

Despite the obvious benefits of solvent-free electrolysis, underlying challenges do exist. Apart from smaller molecule alcohols, viscosity can be an issue that is hard to circumvent as it significantly limits the solution conductivity. Moreover, the solubility of electrolyte can also be limited. We then anticipate that the introduction of solvent is needed to provide the necessary ionic conductivity, especially for larger alcohols. However, to maximize the benefits from 1) chloride-mediated formation of alkyl hypochlorite and 2) selectivity control from acetalization, a large enough alcohol concentration is expected to be present in the solution. Moreover, the choice of solvent is to be considered. Water for example, is to be avoided due to the likelihood of forming active chlorine species when oxidizing chloride. We hypothesize that aprotic polar solvent has the most potential, including

dichloromethane, acetonitrile, and propylene carbonate. Further studies should be conducted in these solvents, with concentration of the alcohol substrate exceeding that of the supporting electrolyte.

Additionally, realizing the formation of DEE in neat ethanol oxidation heavily relies on the nucleophilic attack of ethanol molecule, we hypothesize that the addition of a strong nucleophile could alternate the primary product for this mechanism, especially since the acetaldehyde is slowly generated homogeneously with the chloride mediated mechanism. A stronger nucleophile, for instance, methoxide anion, has the potential to change the DEE product to dimethoxyethane. We anticipate more reaction pathways to be discovered for electrocatalysis in neat ethanol system with different functionalized products. Finally, the formation of EtOCl in neat ethanol upon the oxidation of chloride could be exploited. It is noteworthy that in Chapters 2 & 3, EtOCl is not used as an oxidant, nor as a functionalization agent despite its ability to do so. It is thus believed that the high selectivity from EtOCl fromed *in situ* has the potential to functionalize or oxidize *other* organic substances dissolved in ethanol.

5.3. Photochemical Neat Alcohol Oxidation with Hydrogen Evolution

The inevitable bottleneck of electrocatalysis in the case of neat alcohol oxidation is determined to be conductivity, which is a term that can be thoroughly circumvented by non-electrochemical methods. We realize that photocatalysis is also driven by renewable energy, can also be carried out with abundant metal chalcogenides, and possesses the redox capabilities to generate hydrogen gas as a byproduct alongside alcohol oxidation. By applying semiconductor photocatalysts in neat alcohol, not only larger alcohols can be handled without the worry of conductivity, but also mediators can still be applied to alternate the mechanism. In a recent literature review, we demonstrated the strategies on photocatalytic alcohol oxidation reactions carried out on noble metal free materials. It is found that photocatalytic performance can be optimized by bridging the heterogeneous and homogeneous processes with redox mediators, designing nanomaterial syntheses that focus on the growth of active facets, reducing the particle size to expose more active areas, and morphological engineering of the nanoparticles. Such results are summarized from multiple common light-absorbing materials, including TiO_2, ZnO, WO_3, CdS and g-C_3N_4.

5.4. Preliminary Results for Photochemical Neat Ethanol Oxidation

To test the possibility of the above-mentioned photochemical scheme, we carried out preliminary trials with hydrothermal-synthesized CdS nanowires in neat ethanol. CdS nanowires are prepared by a hydrothermal method, where 10 mmol $Cd(NO_3)_2$ and 40 mmol thiourea is dissolved in 30 mL ethylenediamine with sonication. This mixture is then placed in a furnace held at 160 C for 48 hours, and the product is filtered, washed with ethanol (3 times) and water (3 times) before drying in a vacuum oven. The diffuse reflectance data and Tauc plot obtained for this yellow powder is shown in **Figure 5.1**, confirming its ability to absorb blue light with an optical bandgap of 2.43 eV.
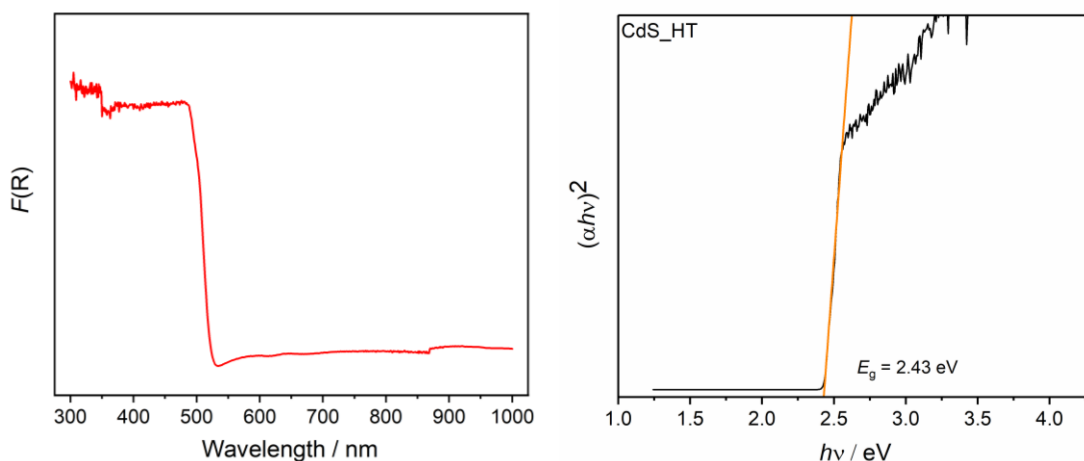
Figure 5.1. Diffuse reflectance measured for prepared CdS and corresponding Tauc plot.

The CdS photocatalyst is then mixed with ethanol solution with 10 mM dissolved electrolyte at 1 mg/mL ratio. In each run, triplicates of 10 mL solutions are placed under 200 mW/cm^2 447.5 nm LED irradiation for 24 hours, with a catalyst-free control experiment under the same light. A fan is applied to control the temperature increase during the photolysis, and the concentrations of DEE product are quantified by GC in the same methodology demonstrated in Chapter 4. Preliminary results show that when the atmosphere is air, ~32 mM DEE can be produced for Bu$_4$NCl electrolyte, and no conversion is observed for chloride-free electrolyte, highlighting the effectiveness of chloride as a potential mediator. Yet, the CdS completely dissolved only in the Bu$_4$NCl case. Under N$_2$ atmosphere however, no product is observed in either Cl$^-$ and Cl$^-$ free conditions, while CdS remains undissolved. We thus hypothesize that in the air & Cl$^-$ case, the oxygen

reduction reaction (ORR) proceeds alongside the oxidation reaction, and forms oxidative products that convert the sulfide to sulfate, which makes soluble Cd^{2+}.

To facilitate the HER capability so that the reaction can be carried out in air-free conditions to avoid ORR, 1 mol-% of NiS is decorated on CdS *via* a hydrothermal method. 1 mol-% of $NiCl_2$ and 1.6 mol-% of L-cysteine are added alongside synthesized CdS to 30 mL water. This mixture is sonicated to ensure thorough mixing, and then placed in a furnace held at 200 C for 24 hours, and is washed and dried in the same way mentioned above. The collected powders now have a greener color. **Figure 5.2** showed the XRD patterns for CdS and CdS-NiS, where both materials showed the same wurtzite structure.
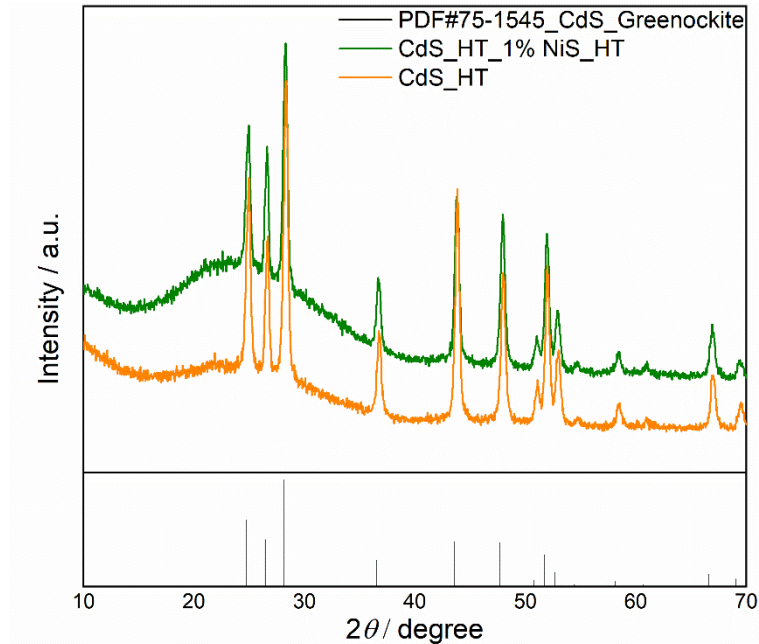
Figure 5.2. XRD patterns for CdS and CdS-NiS. No visible difference is present before and after the loading of NiS.

Figure 5.3 shows the SEM image before and after NiS loading, as well as the EDS mapping data that confirms ~ 1% loading of Ni. Thus, we note our heterojunction material to be CdS-1%NiS.
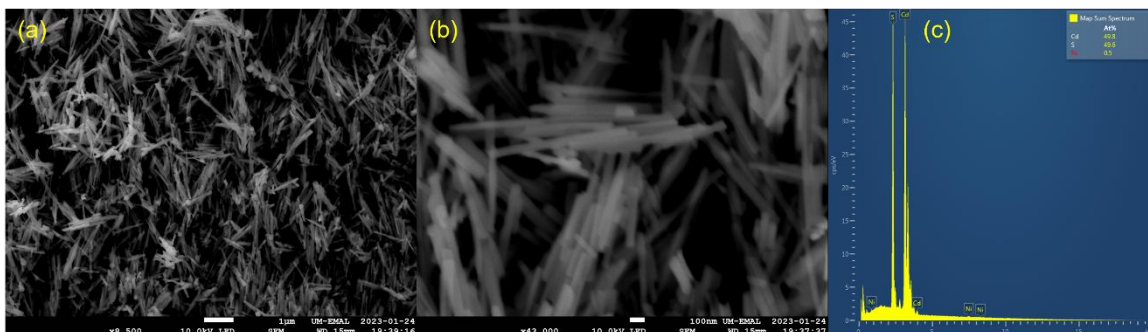
Figure 5.3. (a) and (b): SEM images at different magnifications for obtained CdS-NiS nanowires. (c): EDS mapping data showing the ratio between Cd and Ni elements.

Under the same irradiation but in a N_2 glove box, we found CdS-1%NiS can also oxidize ethanol to DEE, yet only when acid is present. **Figure 5.4** shows the concentrations of DEE generated after 24-hour irradiation with different electrolyte dissolved.
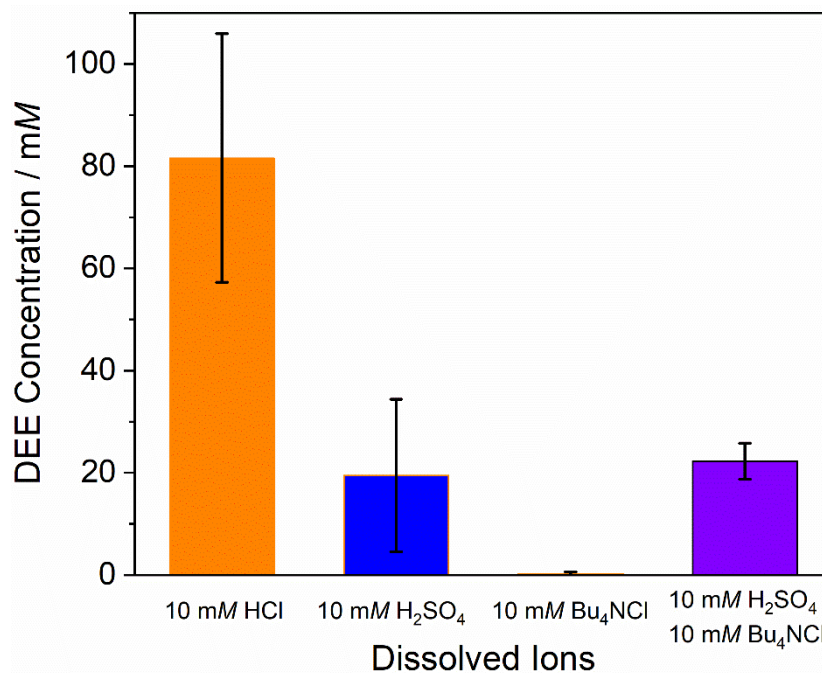
Figure 5.4. DEE concentration produced after 24-hour photolysis with CdS-1%NiS under N_2 atmosphere.

We observe a much faster DEE formation rate for the HCl vs H_2SO_4 case, demonstrating again the acceleration of ethanol oxidation when there is chloride around. The comparation between HCl and Bu_4NCl indirectly confirm the occurrence of the HER alongside ethanol oxidation. It is noteworthy that the DEE yield of 10 mM HCl in N_2 is also much larger than the yield observed for the 10 mM Bu_4NCl in air case (32 mM). We hypothesize that the generated hydrogen gas quantification can be done through an on-line gas chromatography in our lab with a custom photochemical cell. Although, an underlying issue of CdS-1%NiS

is its acidic instability, and catalyst corrosion is indeed observed during the photolysis for the best-performing 10 mM HCl case shown in **Figure 5.4** (7.23 % Cd and 19.3 % Ni dissolved, confirmed by ICP-MS). This preliminary work indicates the proposed photocatalytic approach has potential to be implemented in the broader alcohol oxidation scheme. We anticipate successful neat alcohol photochemical oxidation with other photocatalysts or encapsuled CdS; and that not only small molecule alcohols can be selectively oxidized this way.

Appendices

Appendix A

Supporting Information for Chapter 2
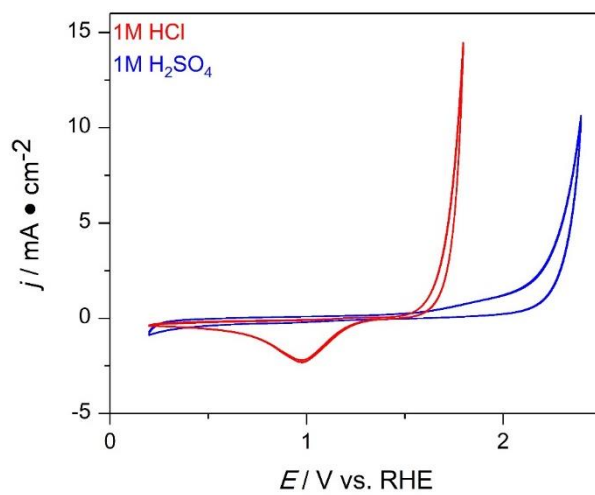
Figure A.1. CV measurements on glassy carbon electrode in water with acid electrolytes. Working electrode: glassy carbon; reference electrode: saturated Ag/AgCl. Scan rate: 100 mV/s.
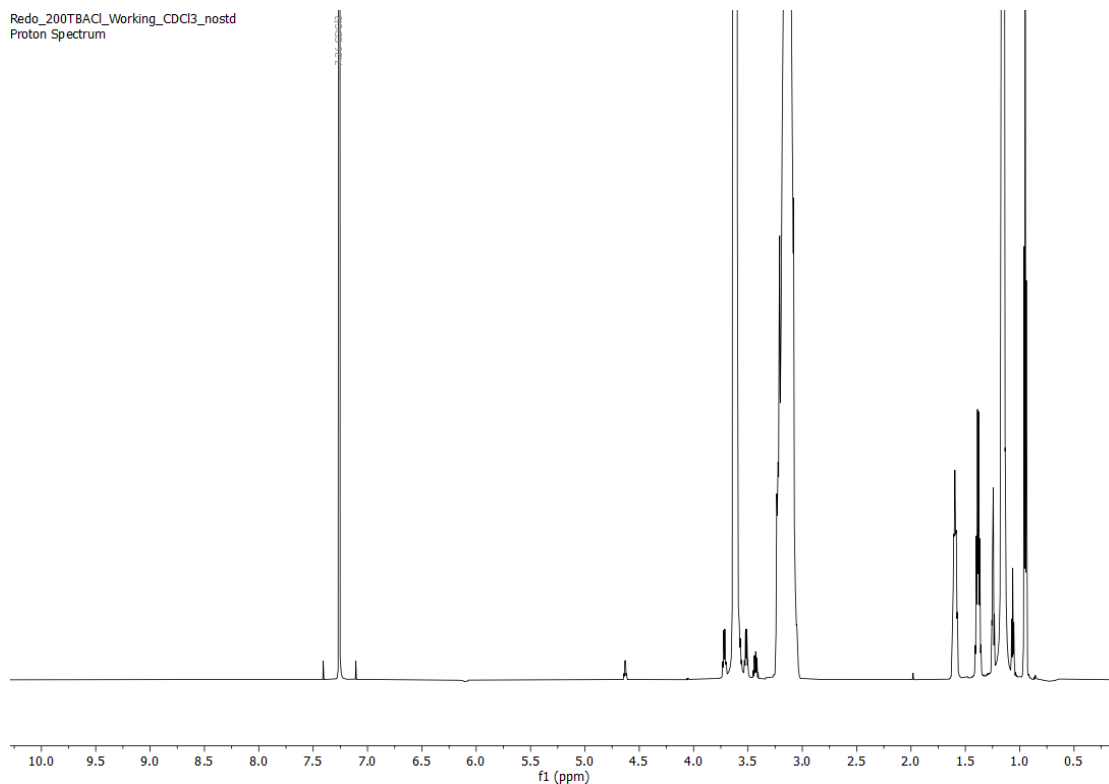
Figure A.2. ^{1}H-NMR spectrum for a post-CPC experiment reaction mixture. The sample is prepared by diluting 100 μL aliquot in 500 μL CDCl$_3$. Chemical shifts: chloroform (7.26, 1H). tetrabutylammonium chloride (3.21, 8H, m; 1.58, 8H, m; 1.37, 8H, m; 0.94, 12H, t). EtOH (3.60, 2H, q; 3.15, 1H; 1.14, 3H, t). DEE (4.61, 1H, q; 3.43, 4H, m; other peaks overlay with the solvent peak).
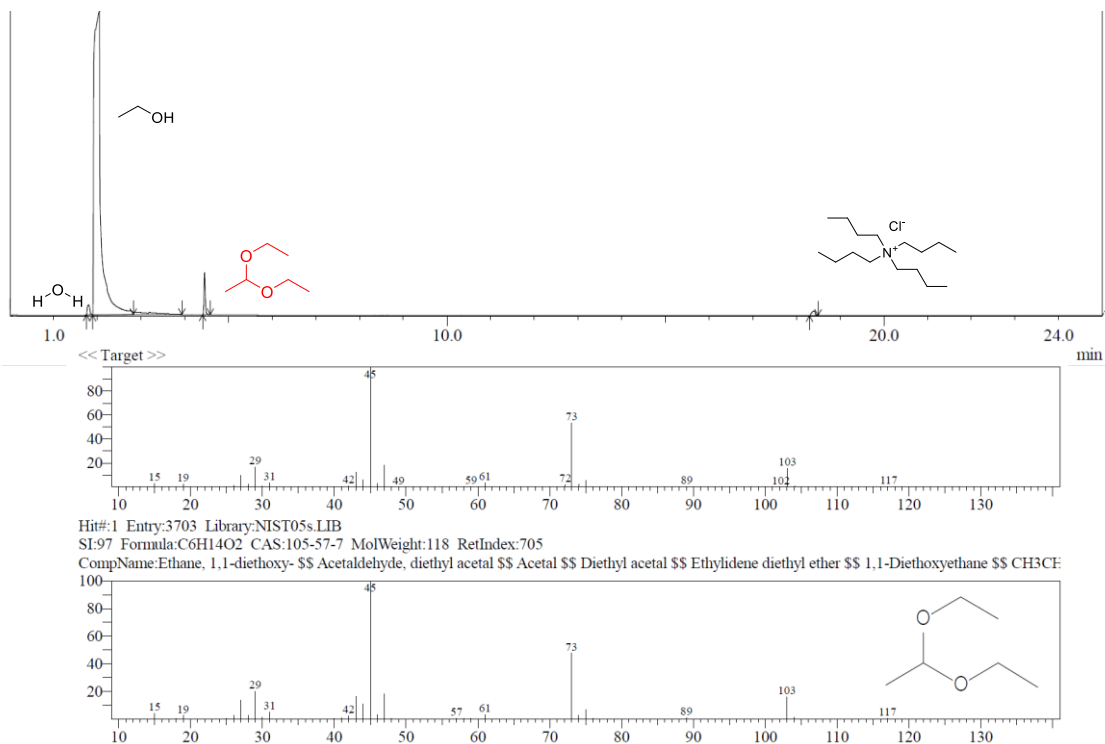
Figure A.3. GC-MS chromatogram for the post-CPC reaction mixture and m/z ratio graph for the 1,1-diethoxyethane peak (retention time = 4.45 min) with the standard graph from NIST.
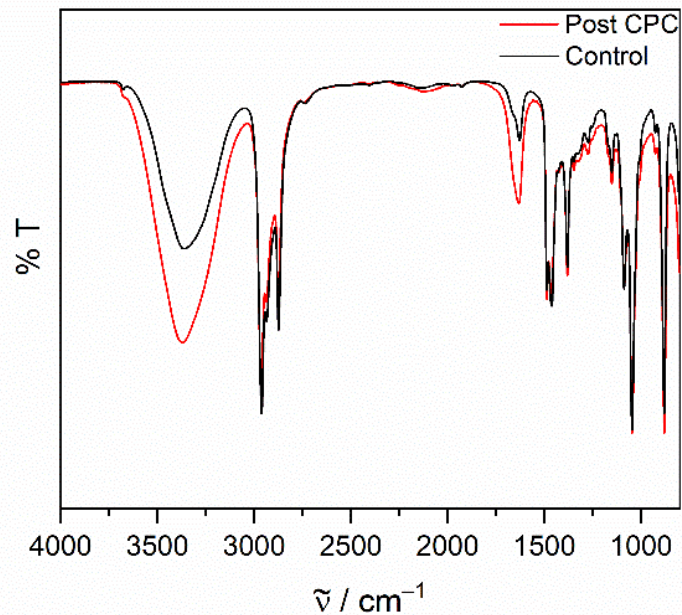
Figure A.4. FT-IR spectrum of an aliquot of the reaction mixture recorded before (black) and after (red) the CPC experiment. The % transmittance value was normalized, and the only differences are attributed to water (the reaction byproduct): ν_{O-H} (3360 cm^{-1}) and δ_{H-O-H} (1630 cm^{-1}).[1]
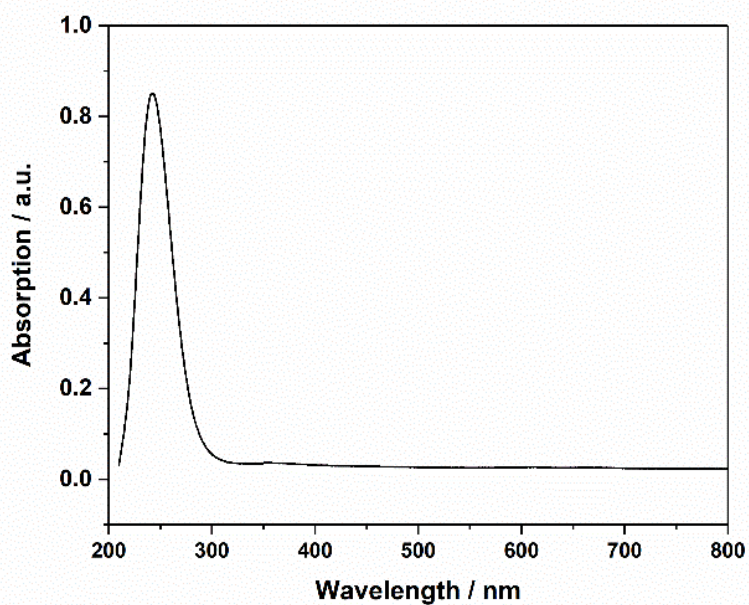
Figure A.5. Extended-range UV-vis absorption spectrum of diluted aliquot after the 1h CPC experiment. The EtOCl signature peak remains as the only notable absorption feature throughout the UV-vis range.
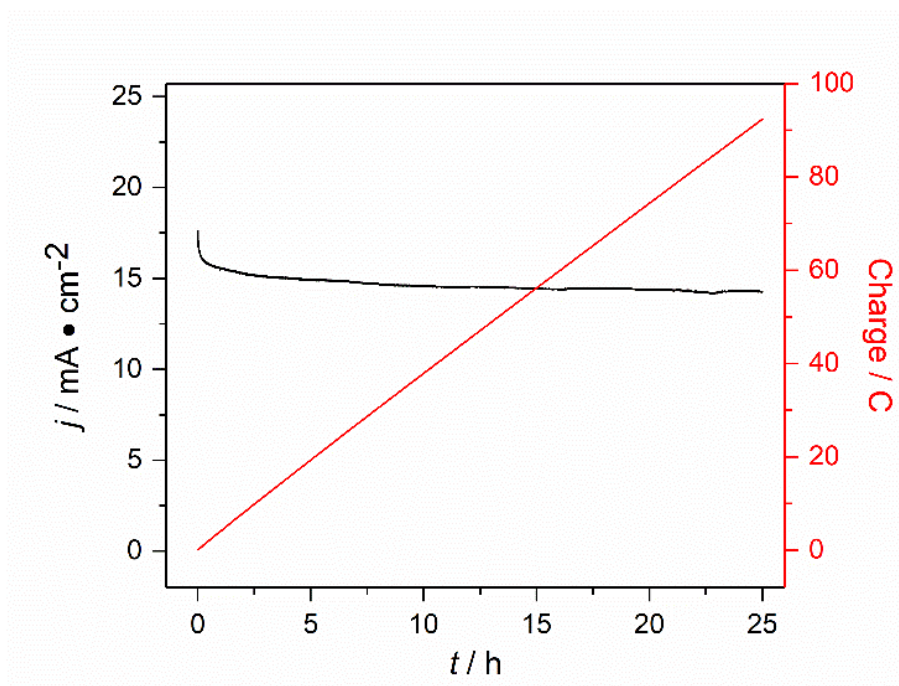
Figure A.6. Long-time CPC experiment for measuring chloride recovery. CPC potential: +1.61 V vs. Fc$^{+/0}$. Black: CPC $i - t$ curve. Red: Charge passed $q - t$ from integrating the $i - t$ curve. In total, 96.77 C of charge passed, which would correspond to 50.1% of chloride being consumed (100.3 mM chloride consumption out of 200 mM) *if* chloride reacted stoichiometrically.

Trial a): slope = $-6.436 \cdot 10^{-4}$ s^{-1}
Trial b): slope = $-6.636 \cdot 10^{-4}$ s^{-1}
Trial c): slope = $-7.616 \cdot 10^{-4}$ s^{-1}

$k = 6.896 \pm 0.516 \cdot 10^{-4}$ s^{-1}
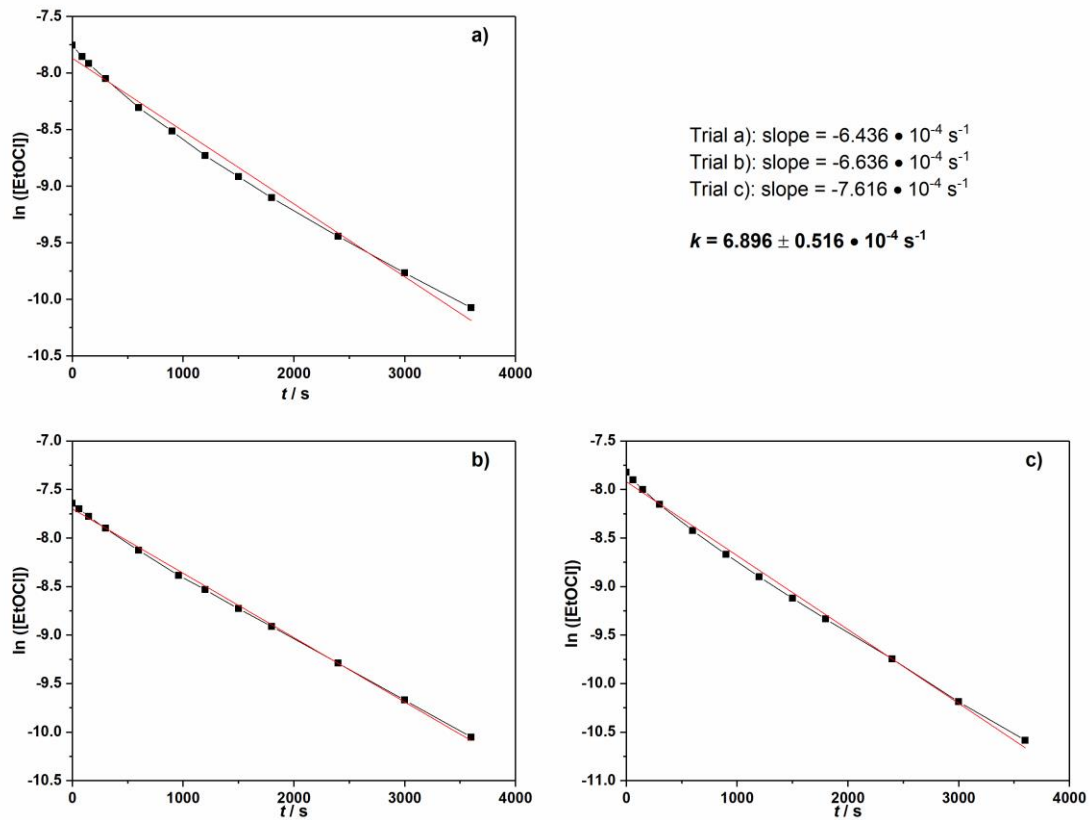
Figure A.7. Replicates of UV-vis measured EtOCl degradation kinetics presented in **Figure 2.4**. The CPC was carried out for 1 hour and the initial concentration is confirmed by titration.
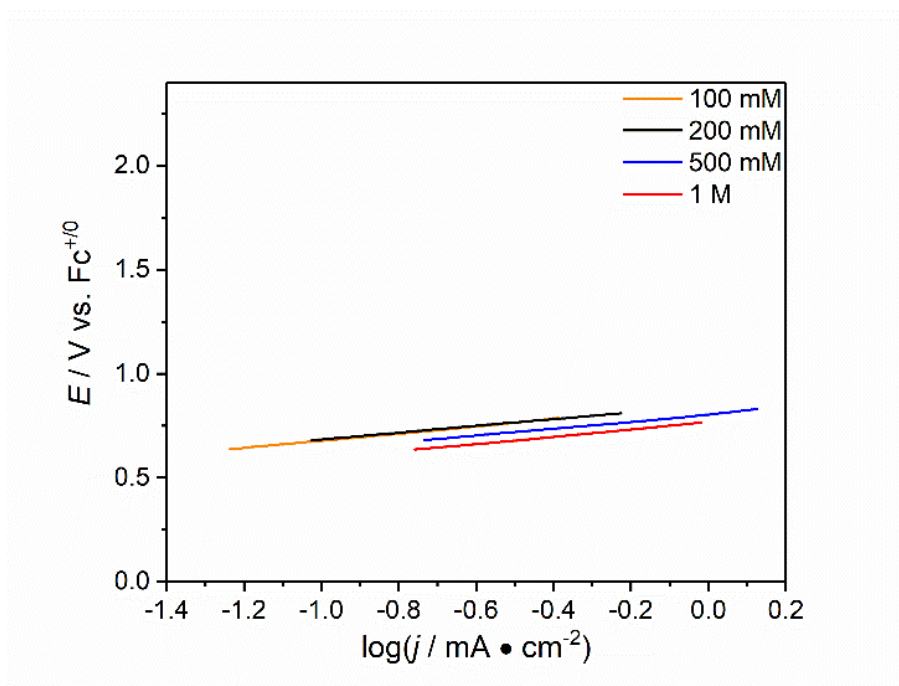
Figure A.8. Tafel slopes for varying concentration of chloride electrolyte in ethanol solution. The numeric slopes: 100 mM, 173.7 mV/dec; 200 mM, 162.7 mV/dec; 500 mM, 169.4 mV/dec; 1 M, 176.0 mV/dec.

---

[1] Mojet, B. L.; Ebbesen, S. D.; Lefferts, L. Light at the interface: the potential of attenuated total reflection infrared spectroscopy for understanding heterogeneous catalysis in water. *Chem. Soc. Rev.* **2010**, *39*(12), 4643-4655.

Appendix B

Supporting Information for Chapter 3
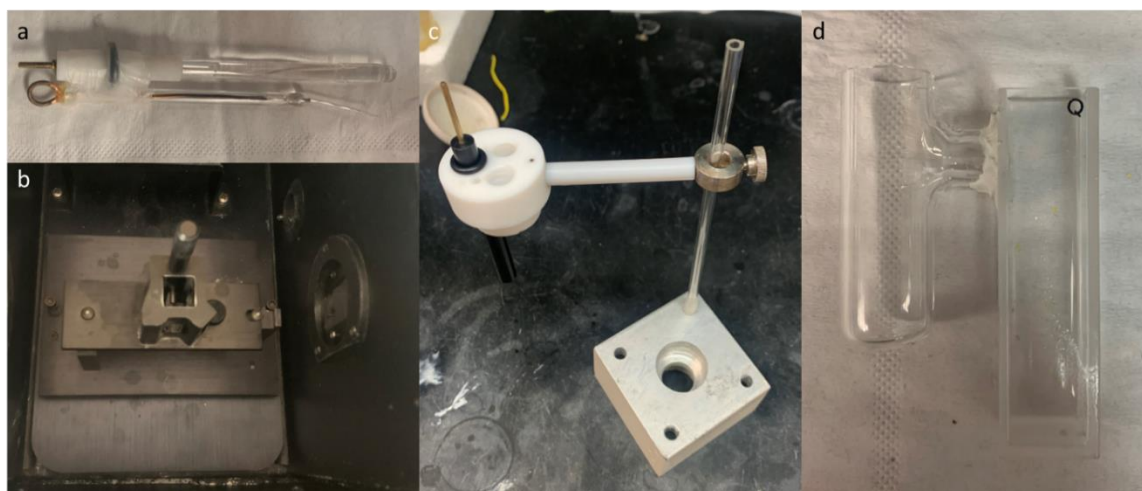
Figure B.1. Custom spectroelectrochemical setup.

(a) Assembly of the DIY reference and counter electrodes used in the quartz cell (d).

(b) Inside of Agilent Cary 5000 UV-Vis-NIR spectrophotometer's measurement chamber.

(c) The working electrode holder from CH Instrument with a simple stand that is placed in (b).

(d) Custom-made spectroelectrochemical cell. The quartz cuvette was sawed off a 4 mm diameter hole where a glass tube is attached to allow the placement of the other 2 electrodes, while the glassy carbon working electrode is placed in the quartz compartment. The junction was sealed by Epoxy.
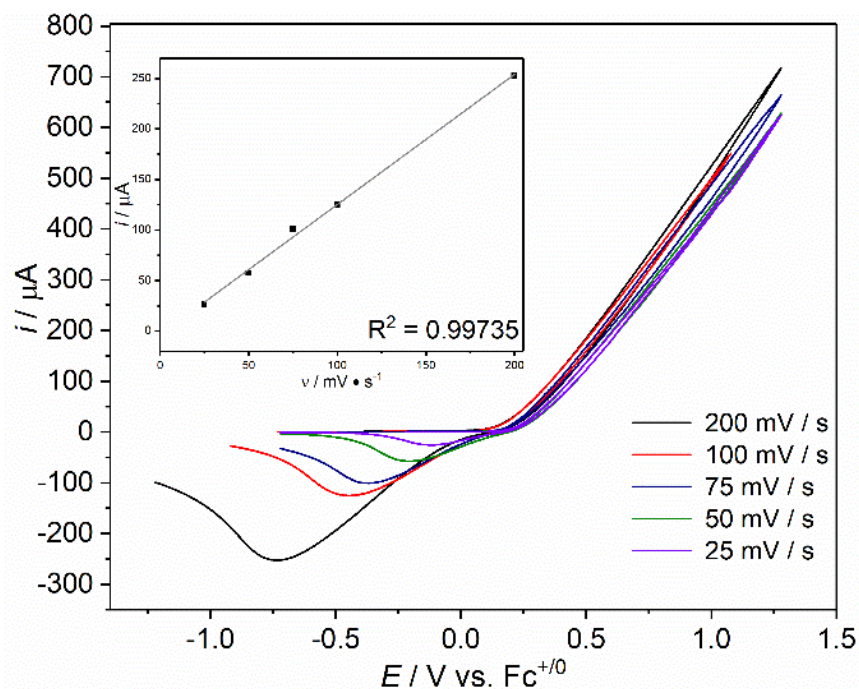
Figure B.2. CV measurements at different scan rates, with 100 mM Bu4NCl dissolved in DCM. The working electrode is glassy carbon disk. The inset shows the linearity of $|i_{pc}|$ against first order of scan rate. At this high chloride concentration, higher current is guaranteed so the peaks can be well resolved.
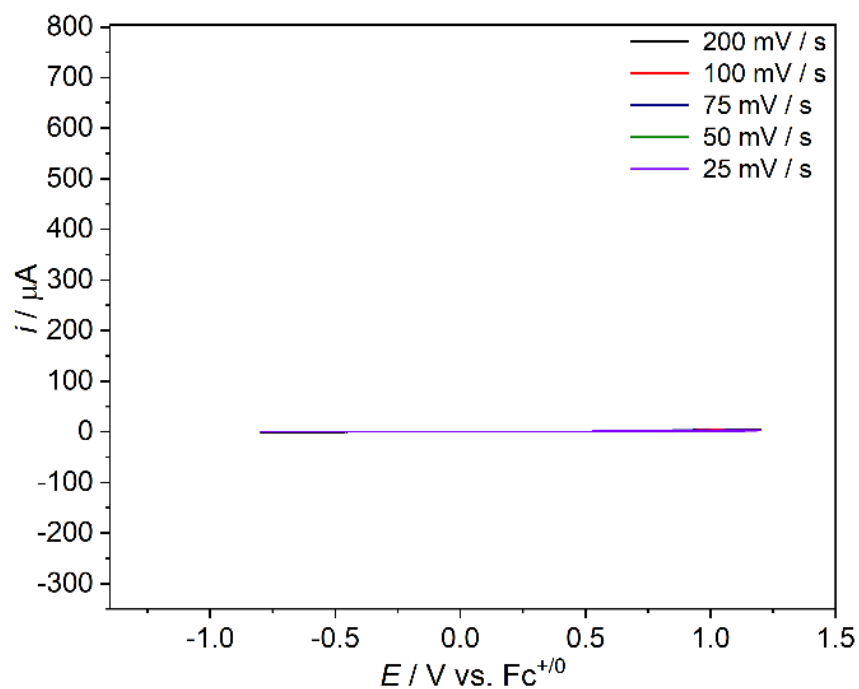
Figure B.3. CV measurements carried out at different scan rates, with 100 mM Bu_4NPF_6 dissolved in DCM. The same electrochemical setup is used as in Figure B.2. The same y-axis scale in Figure B.2 is also used for comparison.
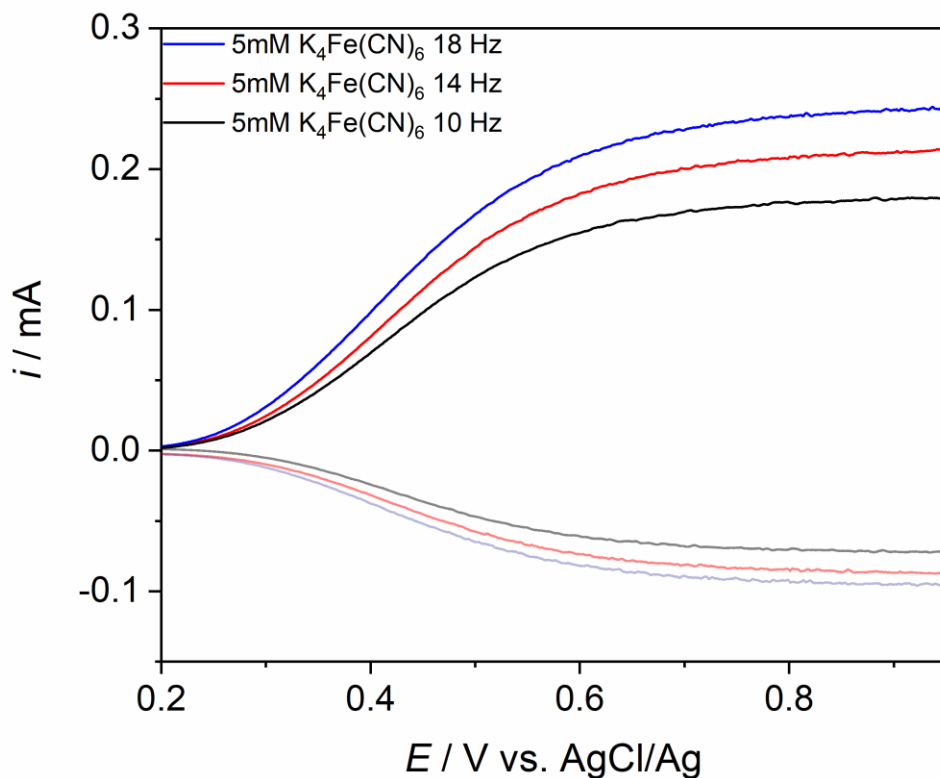
Figure B.4. RRDE LSV with Pt-ring (cathodic) and GC-disk (anodic) in 100 mM Na$_2$SO$_4$, aqueous solution with 5 mM K$_4$Fe(CN)$_6$ dissolved. The Scan rate = 20 mV/s, E_{ring} = 0.1 V vs AgCl/Ag reference. The counter electrode is Pt wire. The experiment is conducted in a 3-compartment cell with no purging gas. Starting potential is OCP, scan direction is positive.

At 0.9 V vs. Ag/AgCl, the corresponding collection efficiency: 10 Hz, 40.06%; 14 Hz, 40.60%; 18 Hz, 38.95%. The collection efficiency is determined from averaging these values, and it agrees with the manufacturer-provided theoretical value based on the dimensions and structure of the RRDE.
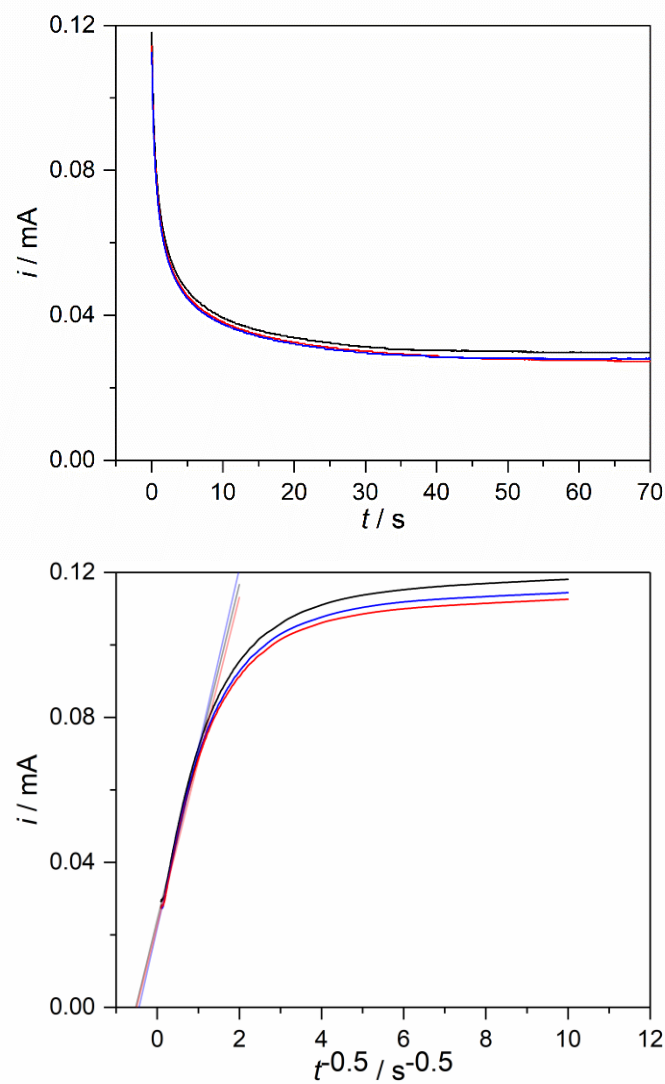
Figure B.5. Cottrell experiments to measure the diffusion coefficient of Cl⁻ in ethanol. Electrolyte: 100 mM Bu₄NOTf, 5 mM Bu₄NCl. Electrodes: Glassy carbon disk (working), Ag wire (reference), Pt wire (counter). Data are recorded in triplicate and the numeric results are averaged.

Top: replicates of CPC at 2 V vs. Ag wire. Bottom: i vs $t^{-0.5}$ plot, guided by $i = \frac{nFAC^0_{Cl^-}\sqrt{D_{Cl^-}}}{\sqrt{\pi t}}$. [1] average slope: 4.701×10^{-5} mA·s$^{0.5}$; average D_{Cl^-}: 1.522×10^{-6} cm²/s
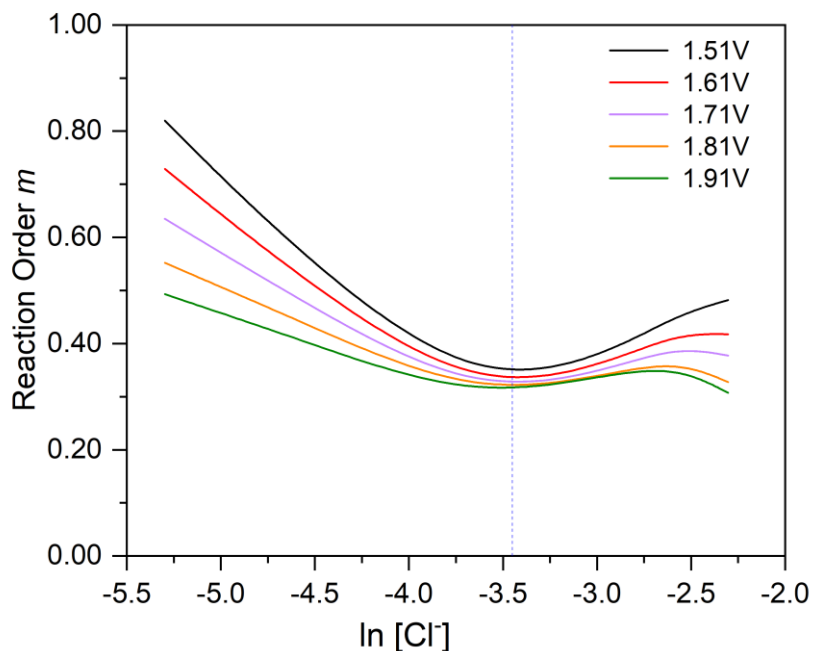
Figure B.6. Estimate of apparent reaction order regarding the concentration of chloride. RRDE experiments at 2400 rpm rotation rate are performed for varied [Cl⁻].

m is obtained with the following equation[2]:

$$ m = \left(\frac{\partial \ln(i)}{\partial \ln \left(c(Cl^-) \right)} \right) $$

Where i corresponds to the measured disk current. The vertical line in the figure represents the estimated reaction order with minimal interference from mass transport. Such reaction order values are used with the i_k calculated from K-L analysis, where ideal mass transport is assumed. Numerical values can be found towards the end of this Appendix.
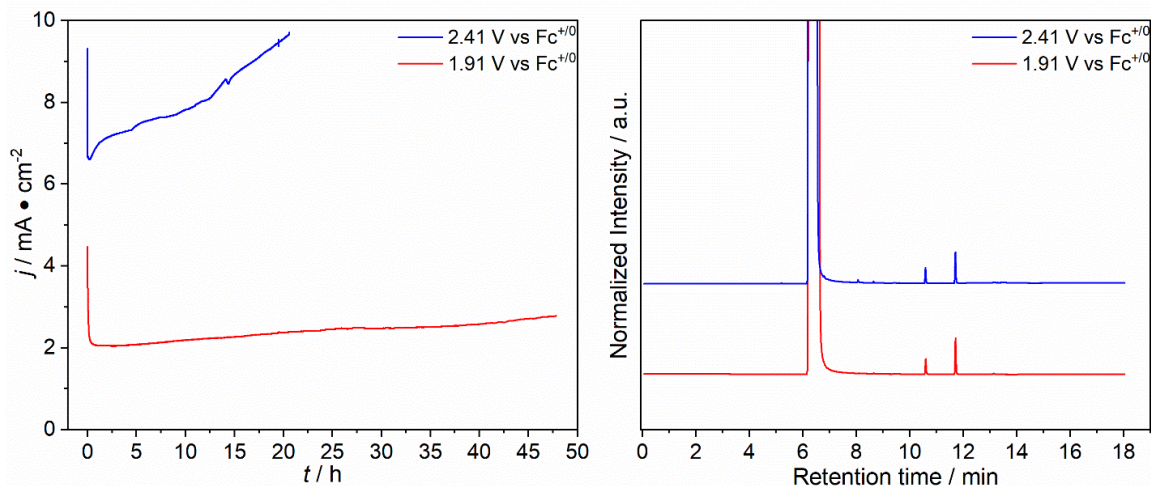
Figure B.7. CPC j-t curve of direct ethanol oxidation at varied potential and GC chromatogram on the post-CPC solution. Electrolyte: 100 mM Bu$_4$NOTf dissolved in ethanol. In both cases, CPC are run in cell shown in Figure S1, and total charge passed is controlled between 30 and 40 C.

Speciation in the chromatogram: CH_3CH_2OH, Rt ~ 6.2 min; CH_3COOH, Rt = 8.072 min; $CH_3COOC_2H_5$, Rt = 8.633 min; 1,1-diethoxyethane (DEE), Rt = 10.607 min; toluene (internal standard), Rt = 11.716 min. In such case, DEE represents 2-electron AOR product; CH_3COOH and $CH_3COOC_2H_5$ represents 4-electron AOR product. In the high-potential blue chromatogram, 4-electron AOR product are seen.
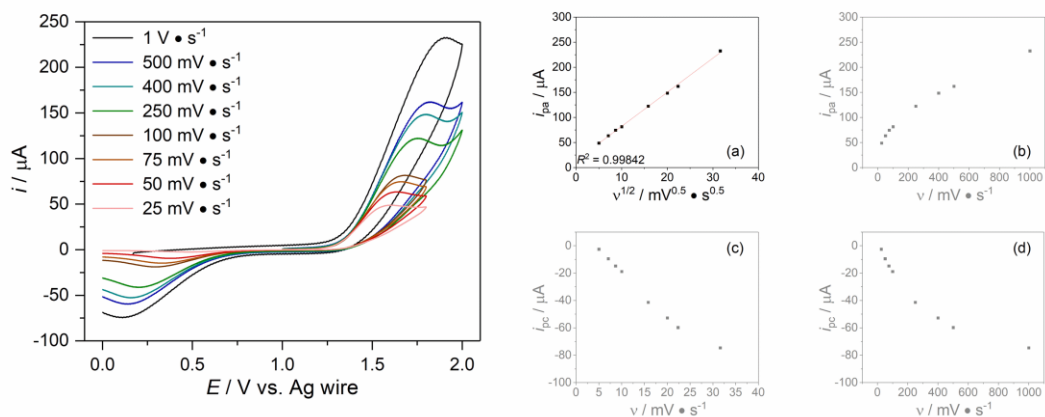
Figure B.8. Peak current – scan rate study for 10 mM Bu₄NCl and 90 mM Bu₄NOTf in ethanol. The working electrode is a glassy carbon disk. Left: CV curves. Right: Relationship of peak currents from the CV traces and either the square root of scan rate or scan rate. Note that due to the spontaneous degradation of EtOCl, the species responsible for the cathodic current, measured cathodic currents are lower than what should be expected for either case. This mismatch is more significant for slower scan rates.
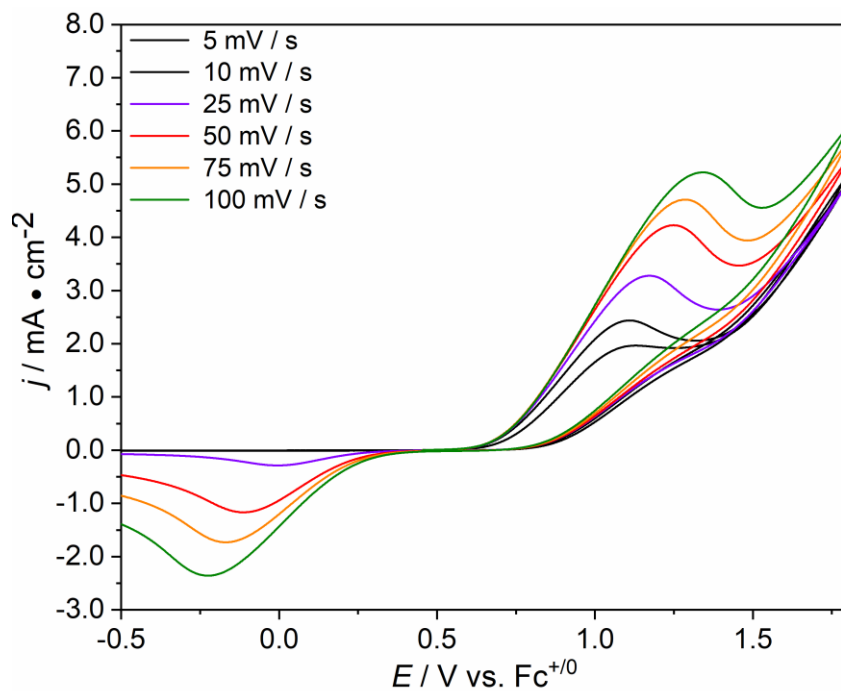
Figure B.9. CV curves for electrolyte containing 50 mM Bu$_4$NCl and 50 mM Bu$_4$NOTf in ethanol, with varied scan rates. The working electrode is a glassy carbon disk.

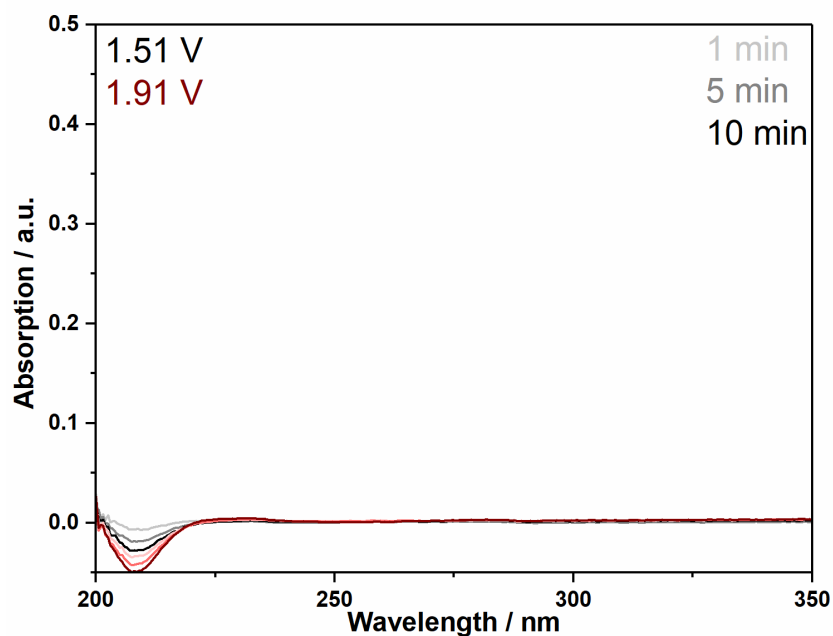Figure B.10. Spectroelectrochemical measurement of 100 mM Bu4NOTf solution poised at two different potentials in the custom cell. The UV-vis absorption measurement of the electrolyte is carried out every minute while the constant potential coulometry runs for 20 mins. Only selected timepoints of measurement are shown for clarity. The negative absorption values may be due to the destruction of species that were in the background.

K-L Analysis Calculations and Other Numeric Results.

Parameters:

F: Faradaic constant, 96,485 C/mol;

A: geometric surface area of the disk electrode, 0.12567 cm^2;

D, diffusion coefficient of the reduced species in the redox reaction of interest. Chloride in ethanol: 1.522×10^{-6} cm^2/s; ethanol self: 1.01×10^{-5} cm^2/s; [3]

v: kinematic viscosity of solvent. EtOH: 1.391×10^{-2} cm^2/s;[4]

C: concentration of substrate in mol/cm^3. Chloride: adjustable; ethanol self: 1.712×10^{-2} mol/cm^3;

ω: disk angular rotation rate in rads/s.

Table of k_f with different potential and electrolyte is attached below. Units are cm/s. Note that reaction order for the chloride-free case is considered 0 due to ethanol being the solvent.

E / V vs Fc$^{+/0}$	5 mM Bu$_4$NCl	10 mM Bu$_4$NCl	20 mM Bu$_4$NCl	Reaction order m by Cl$^-$	100 mM Bu$_4$NOTf
1.51	9.11×10^{-7}	1.47×10^{-6}	1.19×10^{-6}	0.355	1.88×10^{-9}
1.61	9.27×10^{-7}	1.47×10^{-6}	1.26×10^{-6}	0.337	2.79×10^{-9}
1.71	1.06×10^{-6}	1.49×10^{-6}	1.46×10^{-6}	0.329	4.84×10^{-9}
1.81	1.19×10^{-6}	1.50×10^{-6}	1.63×10^{-6}	0.322	7.99×10^{-9}
1.91	1.28×10^{-6}	1.56×10^{-6}	1.79×10^{-6}	0.317	1.18×10^{-8}

[1] Ruff, I.; Friedrich, V. J.; Demeter, K.; Csillag, K. Transfer diffusion. II. Kinetics of electron exchange reaction between ferrocene and ferricinium ion in alcohols. *J. Phys. Chem.* **1971** *75,* 3303–3309.

[2] Reinsberg, P.; Weiβ, A.; Bawol, P.P.; Baltruschat, H. *J. Phys. Chem. C* **2017**, 121, 14, 7677–7688

[3] Lusis, M. A.; Ratcliff, G. A. Diffusion of inert and Hydrogen-bonding solutes in aliphatic alcohols. *AIChE J.* **1971** *17*(6), 1492-1496.

[4] Petrov A.N.; Alper G.A.. Viscosity of Non-Electrolyte Solutions on Base of Formamide. *Zh. Obshch. Khim*. **1992** *62*,1231-1235
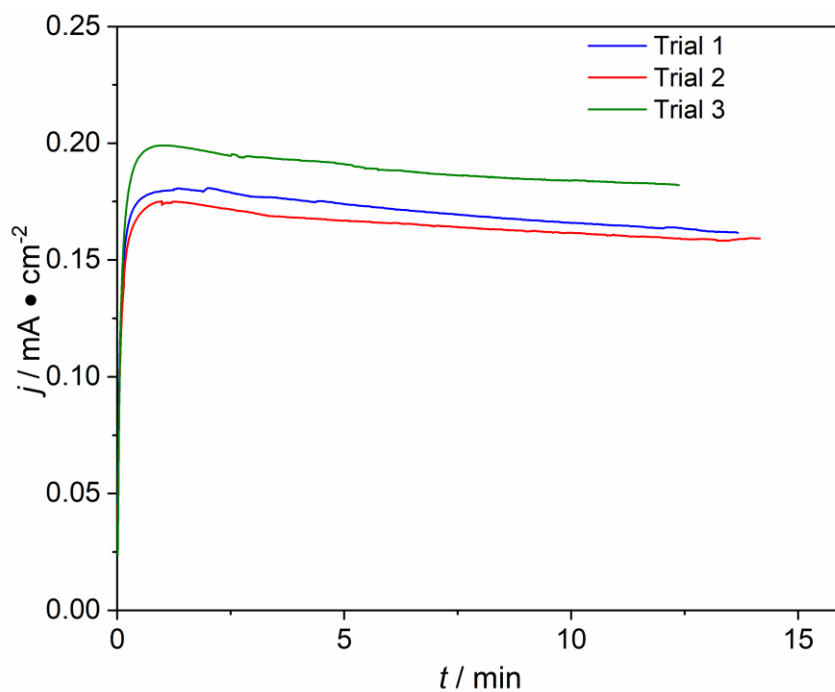
Supporting Information for Chapter 4

Figure C.1. *j-t* curves of replicates of MnO$_x$ CPC electrodeposition on FTO substrate. The exposed area is 2.54 cm*2.54 cm square; applied potential is 1.1 V vs. Ag/AgCl.
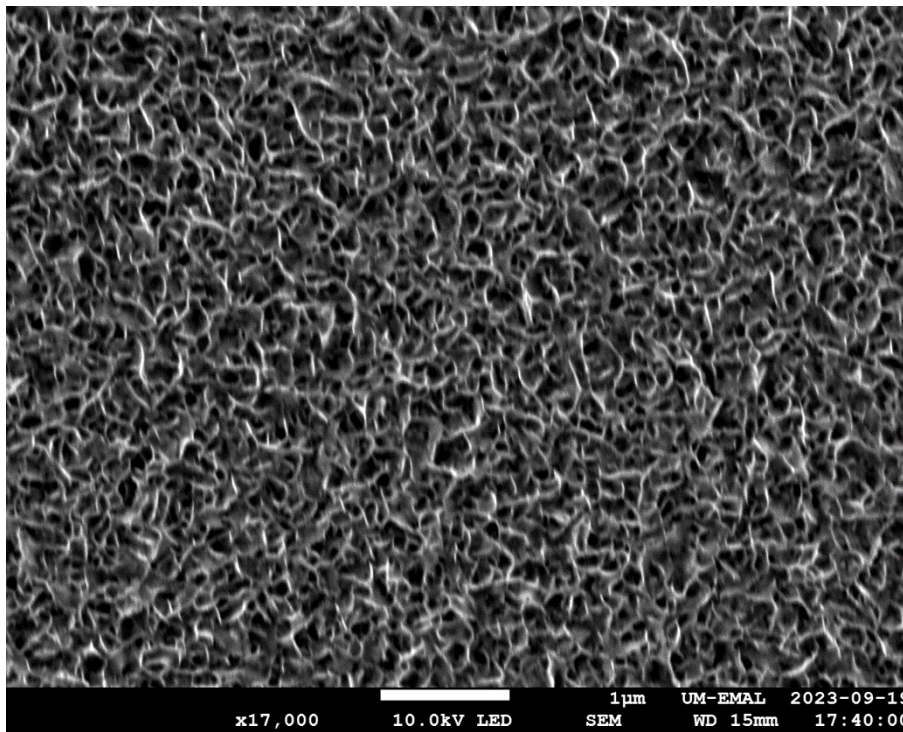
Figure C.2. Top-down SEM image of the as-deposited MnO$_x$ film. The morphology is very similar to the annealed film in **Figure 4.2(a)**.
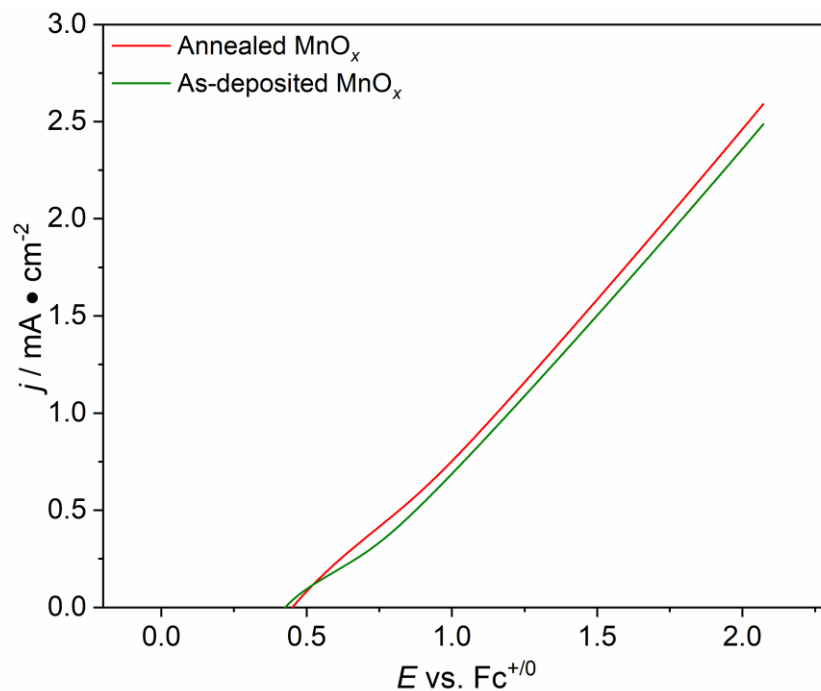
Figure C.3. LSV curves for different films in 200 mM HOTf ethanol solution, in a compression cell. The scan rate is 100 mV/s.
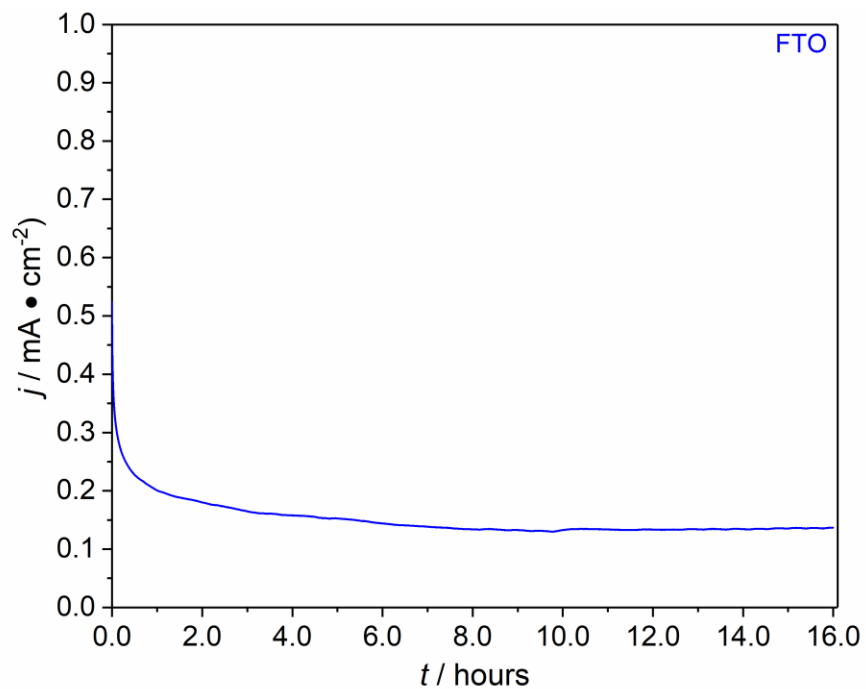
Figure C.4. CPC curves of 200 mM HOTf dissolved in ethanol on FTO over 16 hours. Applied potential is 1.76 V vs. Fc$^{+/0}$.

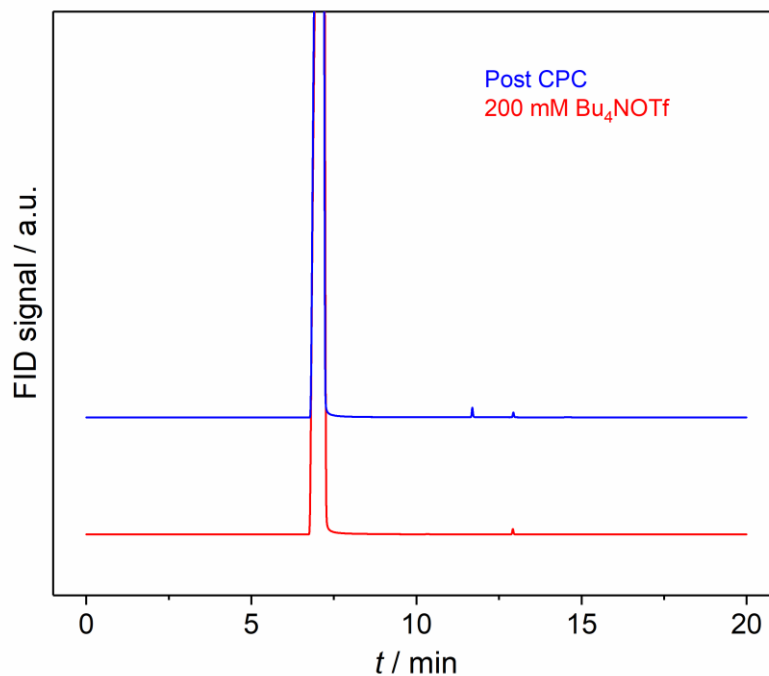Figure C.5. GC-FID chromatograms for (red) 200 mM Bu$_4$NOTf electrolyte in ethanol and (blue) sample after 16-hour CPC at 1.76 V vs. Fc$^{+/0}$. The peak at ~13 minute represents internal standard, toluene. The only noticeable additional peak observed in the blue chromatogram corresponds to the desired product, 1,1-diethoxyethane. The lack of other peaks indicates that the CPC did not generate any 4-electron product in acetic acid or ethyl acetate.
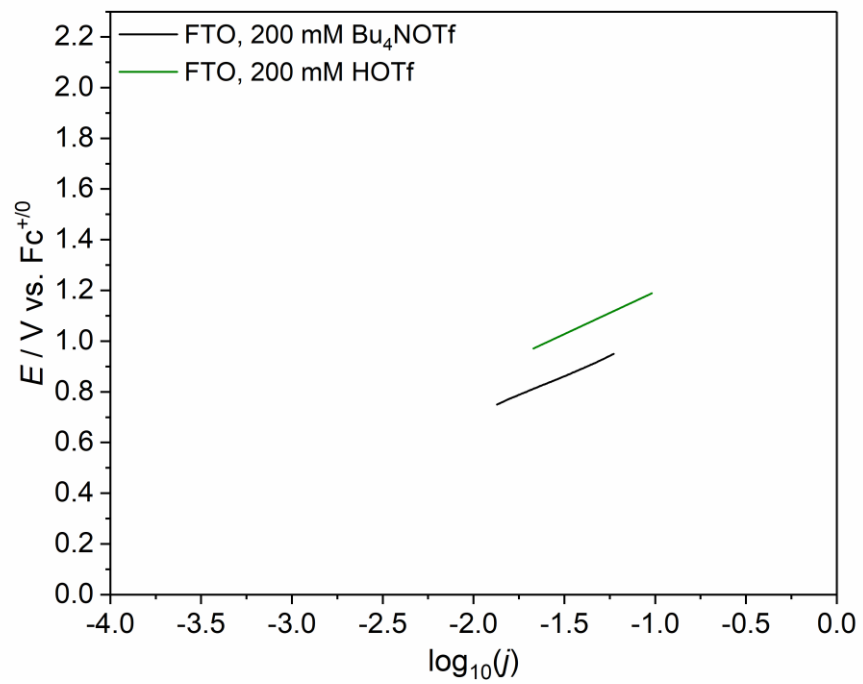
Figure C.6. Tafel analysis with FTO in either 200 mM Bu₄NOTf or 200 mM HOTf. LSVs are carried out at 1 mV/s with vigorous stirring.